Linear and Nonlinear Optical Excitations in Spatially-Inhomogeneous Semiconductor Systems

Dissertation
zur Erlangung des Doktorgrades
der Naturwissenschaften
(Dr. rer. nat)

dem Fachbereich Physik
der Philipps-Universität Marburg
vorgelegt

von
Matthias Reichelt

Marburg/Lahn 2005

Vom Fachbereich Physik der Philipps-Universität Marburg als Dissertation angenommen am 22.06.2005

Erstgutachter: Prof. Dr. S.W. Koch
Zweitgutachter: Prof. Dr. R.M. Noack

Tag der mündlichen Prüfung am 06.07.2005

To Katharina

Morpho menelaus [1]

Contents

Chapter 1

Introduction

> *"There are only two ways to live your life. One is as though nothing is a miracle. The other is as though everything is a miracle."*
> - Albert Einstein

It is a pleasure to present the thesis "Linear and Nonlinear Optical Excitations in Spatially-Inhomogeneous Semiconductor Systems" just in the *Einstein-jahr* 2005. Not only among physicists it is well known that 100 years ago Einstein published several famous articles becoming milestones in modern physics: One is about the photo-electrical effect which may be regarded as the "hour of birth" of quantum mechanics and one about special relativity. Einstein's relationship with quantum physics is quite remarkable. Despite his important contributions to the theory at the beginning of the last century he never accepted its implications culminating in the famous sentence *"Gott würfelt nicht"* (God does not play dice). Of course, over the last century quantum mechanics has proven to work extremely well and, of course, it provides an adequate description of material systems like semiconductors. Thus, on the one hand, *in the sense of Einstein* the reader could feel a little uncomfortable about the "matter-part" of the present thesis which is based on a full quantum-mechanical treatment. On the other hand, (s)he may be relieved to hear that the light "light-part" of this work is based on Maxwell's equations which are in entire accordance with the theory of relativity.

To state it more seriously: by tailoring both, the semiconductor material as well as the electromagnetic field, one arrives at an up-to-date field of research aiming at novel possibilities to design optoelectronic devices with remarkable properties. The following chapters present different fundamental aspects of the light-matter coupling which arise when dealing with spatially inhomogeneous systems. These may be caused by an inhomogeneous distribution of the electric

field (Chap. 2 and Chap. 3) or by an intrinsic inhomogeneous structuring of the material (Chap. 2 and Chap. 4).

The first part of this thesis, **chapter 2**, deals with "semiconductors embedded in photonic crystals". Basically, photonic crystals are periodic dielectric structures that affect the propagation of electromagnetic waves. They can be classified into the categories one-, two-, or three-dimensional according to the dimensionality of the stack, see Fig. 1.1. Whereas first studies on electromagnetic waves propagating in one-dimensional periodic media were already performed in 1887 by Lord Rayleigh, the concept of two- and three-dimensional photonic crystals was introduced not until 1987 by Eli Yablonovitch and Sajeev John [2, 3].
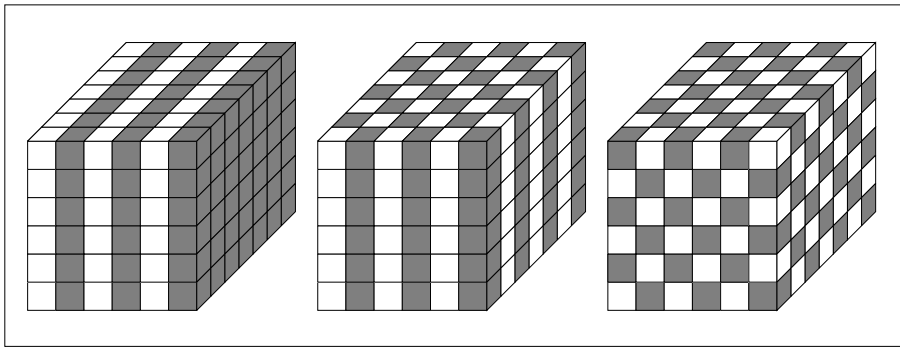
Figure 1.1: Schematic illustration of photonic crystals periodic in one, two, and three directions, respectively, where the periodicity is in the dielectric material structure of the crystal. After Ref. [4].

Analog to an ordinary crystal in which the arrangement of atoms builds up a periodic potential for the electrons the alternating dielectric media in a photonic crystal are a "potential" for the electromagnetic field. Hence, similar effects that can be observed in ordinary crystals also occur in photonic crystals. In particular, if the lattice constant is chosen to have the proper length, gaps in the photonic band structure may form, i.e., light is prevented from propagating in certain directions with specified energies [4–6]. This feature can be extremely useful since, e.g., it is possible to suppress the spontaneous emission and increase the radiative lifetime of optical excitations by several orders of magnitude if excited matter is embedded in such systems [7–9]. Moreover, if the regular array of dielectrics is disordered, one may obtain defect modes which are modes whose eigenfunctions are strongly localized around the region of disorder [10, 11]. In general, it is possible to design and modify the density of states of the radiation field with the help of a photonic crystal. This situation is schematically sketched in Fig 1.2. Actually, many basic

ideas can be transfered from ordinary crystals to photonic crystals, however, one major difference between them is the scale of the lattice constant. Whereas the potential of crystals varies on the order of Ångstroms, the lattice constant for a photonic crystal is on the order of the wavelength of the relevant electromagnetic waves, e.g., about some micrometer for visible light.
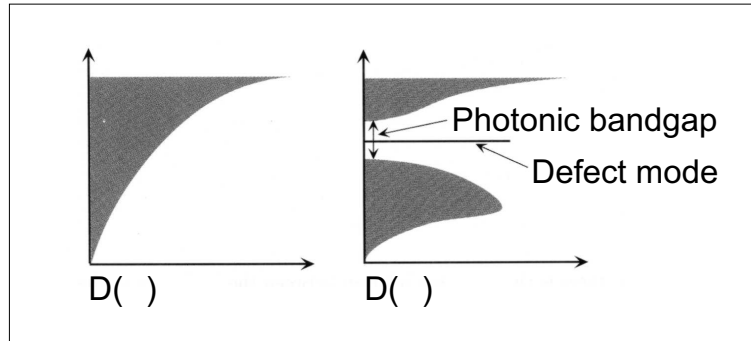
Figure 1.2: Schematic depiction of the density of states for light in free space (left) and in a photonic crystal (right). In vacuum $D(\omega) \propto \omega^2$ holds whereas in the photonic crystal band gaps or localized modes may exist. Taken from Ref. [5].

Semiconductor nanostructures coupled to photonic crystals are very promising material systems [12–14]. In particular, photonic crystals with semiconductors as *active material* have received considerable attention [15–19]. Sheer the introduction of a band structure for the transverse optical field gives rise to interesting new features of the semiconductor. For example, by reducing the spontaneous emission in a certain frequency range strong modifications of the exciton statistics and Coulomb many-body correlations inside the semiconductor material are to be expected [20]. Furthermore, it has been shown that the dielectric environment of the photonic crystal can also alter the longitudinal part of the electromagnetic field, i.e., the Coulomb interaction among charged particles in the semiconductor [21–24]. In this way, the intrinsic properties of the material are modified, too, leading to a different optoelectronic behavior of the system.

In chapter 2 a microscopic theory which is capable of describing the properties of semiconductor nanostructures near photonic crystals is presented. The equations for the electromagnetic field and for the material excitations are treated self-consistently to account for both the transversal as well as the longitudinal modifications of the fields due to the dielectric environment. It is analyzed to what extend the optoelectronic properties of such a hybrid system differ as compared to pure semiconductor structures.

The subject of **chapter 3** is the analysis of the interaction between electro-magnetic waves and planar chiral nanostructures[1]. These structures consist of pure dielectrics and may be investigated with the methods developed in Chap. 2. The considered materials possess certain symmetry properties which manifest itself in the reflected light under particular excitation conditions. If, in addition, the incident electromagnetic field is polarized in a well-defined way, also the light wave may satisfy different symmetry operations. It is analyzed in-depth, both numerically and analytically, to what extent the symmetry properties of the single components (light and matter) influence the behavior of the whole (light-matter) system.

The last part of this thesis, **chapter 4**, treats nonlinear optical excitations at semiconductor surfaces. Actually, these systems are inhomogeneous in the z-direction, i.e., perpendicular to the surface, since the crystal symmetry is broken at the interface between the material and the surrounding[2]. The outermost atoms possess a different number of neighbors compared to the bulk case because some bonding partners disappear leading to so-called *dangling bonds* as is schemati-cally displayed in Fig. 1.3. Due to that cost of energy the surface atoms will react somehow to this modified environment [26]. If they merely move in z-direction and stay in their original positions parallel to the surface the effect is referred to as *surface relaxation*. Often, they will also rearrange in the x-y-plane building up a new unit-cell with a different geometry which is called *surface reconstruction*. In any case, the changes at the topmost atomic layers will lead to novel states which are only present directly at the interface and decay rapidly in the direction to the vacuum and to the material. These states are also responsible for certain optical properties that solely appear at the surface and differ from those in the bulk.

Optical techniques are major tools to investigate the electron dynamics at sur-faces. Although recently some progress has been made in the experimental study of semiconductor surfaces applying ultrafast optical spectroscopy methods such as two-photon photoemission [28–31] and second-harmonic generation [32–34] the theoretical background is by far not as well understood as for bulk semicon-ductors. In chapter 4 two different approaches to describe optical excitations at surfaces are pursued. First, a microscopic theory for computing nonlinear optical properties of a semiconductor surface is presented. It is shown how the relevant parameters which are taken from *ab-initio* band-structure calculations can be com-bined with the semiconductor Bloch equations in order to obtain a consistent theo-

---

[1]An accurate definition of planar chirality is given in Chap. 3.

[2]Many surface techniques require the sample to be in ultra high vacuum with pressures below 10^{-8} Pa [25].
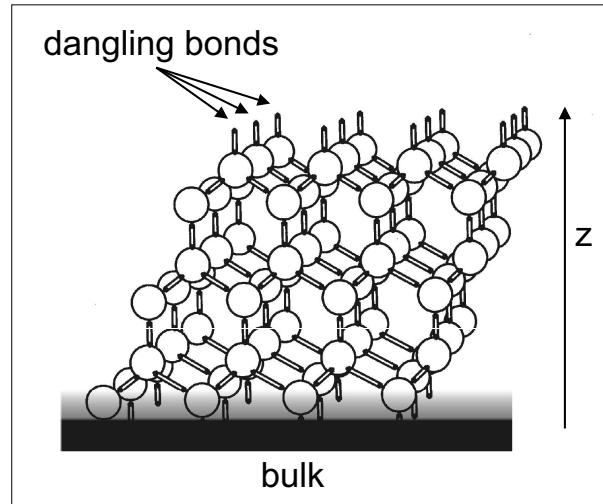
Figure 1.3: Dangling bonds of a (111) surface based on diamond structure. After Ref. [27].

retical description. This theory has predictive capability and is used in section 4.1 to examine the linear and nonlinear optical properties of the Si(111)-(2×1) surface. It is shown that this novel approach is capable of reproducing known results for the surface exciton in the linear regime and is applicable to predict nonlinear optical effects.

In section 4.2 a more phenomenological treatment is introduced. By comparing model calculations with experiments, it is possible to get an understanding of the underlying physical mechanisms which are important for the dynamics of excited states at surfaces. Due to parameters which have to be taken from experiment, the phenomenological approach can only be applied in retrospect and rarely has predictive capability, however, one may obtain valuable insight into the system by excluding or favoring certain assumptions. This can be done by comparing experimental results with the findings of the phenomenological model for different parameter sets. In this manner the temporal evolution of the optical polarization and the photoexcited populations are examined and a new surface specific mechanism occurring at the Si(001)c(4×2) surface is proposed by analyzing femtosecond time-resolved five-wave-mixing experiments with the help of the optical Bloch equations for a three-band model.

Chapter 2

Semiconductors Embedded in Photonic-Crystal Structures

"If only it were possible to make dielectric materials in which electro-magnetic waves cannot propagate at certain frequencies, all kinds of almost-magical things would be possible." - John Maddox

As outlined in the introduction this chapter deals with the description of semiconductor nanostructures combined with photonic crystals. One of the specific structures which is the subject of investigation is schematically sketched in Fig. 2.1. It consists of a periodic array of thin GaAs quantum wires which are placed below a two-dimensional photonic crystal. The main question addressed in the following is in which way the structured dielectric environment influences the optical properties of the semiconductor compared to the common case where it is surrounded with a homogeneous material. Although the derivation of the theory below is quite general and therefore can be applied to various of such hybrid systems one is limited to certain geometries because of numerical restrictions. As afore mentioned the length scales for describing the semiconductor material and the photonic dielectric structuring are greatly different which makes an accurate numerical modeling rather demanding. In particular this is the reason for using an array of quantum wires in the simulations while utilizing a quantum well would be more suitable for experimental studies because these structures can be grown easier. However, general physical aspects of the combined systems can already be shown with reduced numerical effort for the special geometry considered here.

To describe the situation properly one is primarily faced with two problems. On the one hand the periodic dielectric structuring alters the density of states for the electromagnetic field, i.e., due to the photonic crystal the propagation of the
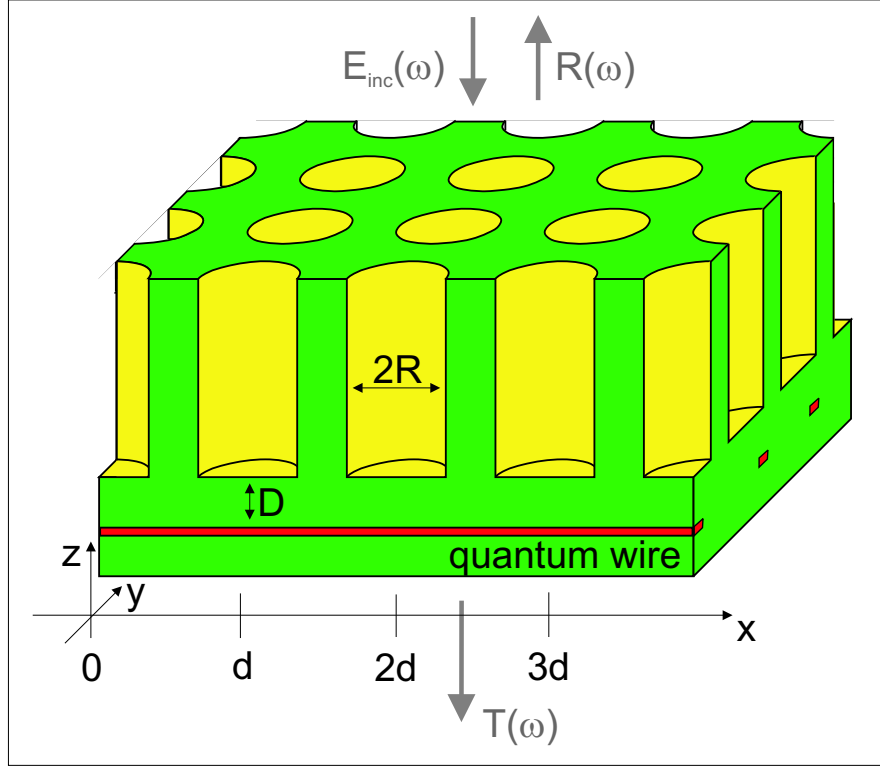
Figure 2.1: Drawing of the combined semiconductor photonic crystal structure: An array of quantum wires is placed at distance D beneath a two-dimensional photonic crystal based on a square lattice with the lattice constant d. The air cylinders have a radius R and their bottom part decrease circularly with radius r, q.v. Fig. 2.9(b) on page 24. The period of the wires and the crystal coincide. After Ref. [35].

light has to be taken seriously. On the other hand the dielectric environment also influences the longitudinal part of the electromagnetic field, i.e., the Coulomb interaction among charged carriers, meaning that the intrinsic properties of the semiconductor are modified, too.

In general, the vector Maxwell semiconductor Bloch equations have to be solved. The problem of treating the full set Maxwell's equations

$$\nabla \times \boldsymbol{E} \;=\; -\frac{\partial}{\partial t}\boldsymbol{B}\,, \tag{2.1}$$

$$\nabla \times \boldsymbol{H} \;=\; \boldsymbol{j} + \frac{\partial}{\partial t}\boldsymbol{D}\,, \tag{2.2}$$

$$\nabla \cdot \boldsymbol{D} \;=\; \rho\,, \qquad \text{and} \tag{2.3}$$

$$\nabla \cdot \boldsymbol{B} \;=\; 0\,, \tag{2.4}$$

reduces to the coupled equations

$$\frac{\partial}{\partial t}\boldsymbol{E}(\boldsymbol{r},t) \;=\; \frac{1}{\epsilon(\boldsymbol{r})}\nabla\times\boldsymbol{H}(\boldsymbol{r},t) - \frac{1}{\epsilon(\boldsymbol{r})}\frac{\partial}{\partial t}\boldsymbol{P}(\boldsymbol{r},t) \qquad\text{and} \qquad (2.5)$$

$$\frac{\partial}{\partial t}\boldsymbol{H}(\boldsymbol{r},t) \;=\; -\frac{1}{\mu}\nabla\times\boldsymbol{E}(\boldsymbol{r},t)\,. \qquad\qquad (2.6)$$

in the case of non-magnetic materials and the absence of free electric charges and currents. Here, $\boldsymbol{E}$ is the electric field, $\boldsymbol{H}$ is the magnetic field, $\epsilon(\boldsymbol{r})$ is the space-dependent relative permittivity $\epsilon_r(\boldsymbol{r})$ times the free-space permittivity ϵ_0, and $\mu \equiv \mu_0$ is the free-space permeability. Furthermore, the constitutive relations $\boldsymbol{B} = \mu\boldsymbol{H}$ and $\boldsymbol{D} = \epsilon(\boldsymbol{r})\boldsymbol{E} + \boldsymbol{P}$ are used. The polarization density $\boldsymbol{P}$ whose time derivative appears as additional source term in Eq. (2.5) is due to optical resonances of the semiconductor material.

In section 2.1 the treatment of the electromagnetic field in a photonic crystal with the help of the finite-difference time-domain (FDTD) method is presented. It is outlined how a self-consistent calculation of the field and material equations can be achieved in principle. The proper microscopic description of the semiconductor material is then addressed in section 2.2. The full theory is applied in section 2.3 to different hybrid semiconductor-photonic-crystal systems.[1]

---

[1]Throughout the text the following terminology is used: "Semiconductor" refers to the *active* material having optical resonances in the considered spectral range whereas "photonic crystal" refers to the *passive* structured dielectric (which may also be composed of semiconductor material).

2.1 The Electromagnetic Field in a Photonic Crystal

In Chap. 2 and Chap. 3 of this work the electromagnetic field is calculated numerically with the help of the FDTD-method, which is introduced in this section. After a derivation of the standard technique it is shown how to adapt the algorithm to the current problem.[2] Particularly it is explained in which way self-consistency with the material equations can be obtained.

2.1.1 The Finite-Difference Time-Domain Method

In this subsection an approach for numerically solving Maxwell's equation is presented. The algorithm was already proposed in 1966 by Yee [38] but due to its overwhelming consumption of computer resources it became only utilizable in recent years. Nevertheless, the treatment of the full 3D-Maxwell equations remains a problem and can be achieved only with the help of supercomputers[3] or special geometries as used below.

As starting point we rewrite Maxwell's equations for a dielectric non-magnetic material and drop the macroscopic polarization $\boldsymbol{P}$ in Eq. (2.5). The resulting two equations

$$\frac{\partial}{\partial t}\boldsymbol{E}(\boldsymbol{r},t) \;=\; \frac{1}{\epsilon(\boldsymbol{r})}\nabla \times \boldsymbol{H}(\boldsymbol{r},t) \qquad \text{and} \tag{2.7}$$

$$\frac{\partial}{\partial t}\boldsymbol{H}(\boldsymbol{r},t) \;=\; -\frac{1}{\mu_0}\nabla \times \boldsymbol{E}(\boldsymbol{r},t) \tag{2.8}$$

are sufficient to describe the propagation of light in a photonic crystal represented by a space-dependent dielectric constant $\epsilon(\boldsymbol{r})$. Here, the active semiconductor material is not included yet. The algorithm is quite general and therefore one does not need to make special assumptions about the geometry at his point. In fact it is even possible to apply it to fairly different situations. The introductory chapter of Ref. [36] highlights quite distinct investigations of electromagnetic phenomena for which the FDTD method has been utilized. For instance the fields of military applications (radar related issues), computer engineering (high-speed digital circuits), technical problems (microwave amplifiers), medical research (radiation impact on bodily parts), analysis of photonic crystal structures (e.g. waveguides), and so forth have been covered.

The key idea is to use a discretization grid know as "Yee space lattice" [36] which is shown in Fig. 2.2(a). The components of the $\boldsymbol{E}$- and the $\boldsymbol{H}$-field are

---

[2]The general concepts of subsections 2.1.1 and 2.1.2 primarily follow Refs. [36, 37].

[3]For example, the pure propagation problem in Chap. 3 takes 15-20h on an eight processor IBM eServer pSeries p655+ (1.5GHz) node.
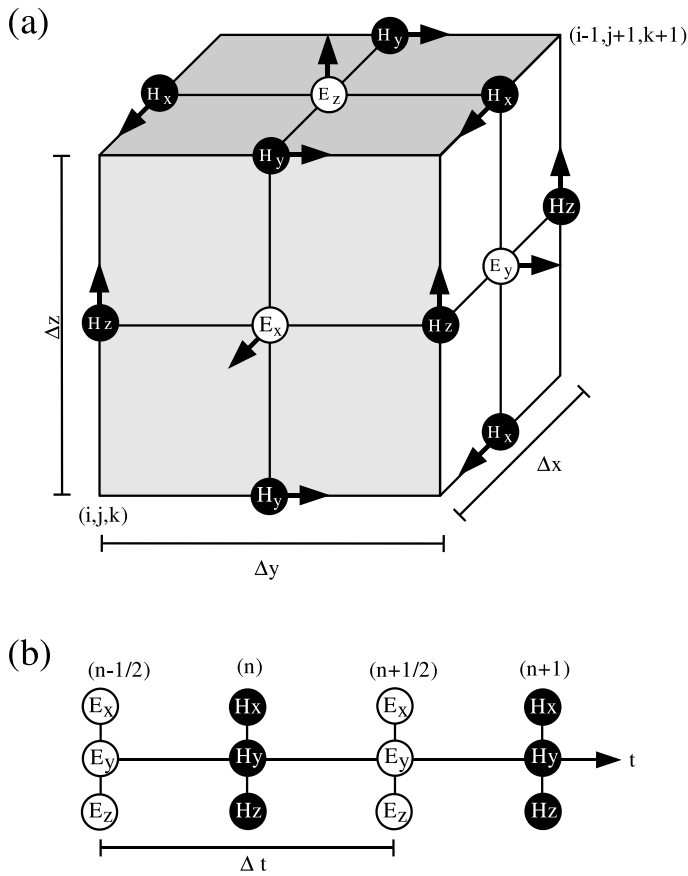
Figure 2.2: (a) The Yee space lattice: Every $\boldsymbol{E}$ component is surrounded by four $\boldsymbol{H}$ components and vice versa. (b) $\boldsymbol{E}$ and $\boldsymbol{H}$ fields are calculated in turn. After Ref. [36].

arranged in such a way that each $\boldsymbol{E}$-component is surrounded by $\boldsymbol{H}$-components and vice versa. On the one hand by using both $\boldsymbol{E}$ and $\boldsymbol{H}$ information the solution of Eqs. (2.7)-(2.8) is more robust than using either alone [36]. On the other hand the spacial stagger together with a Leapfrog time stepping sketched in Fig. 2.2(b) allows for a very compact algorithm which is effectively implementable. Note,

that both, the space grid as well as the time grid, are resolved by $\Delta x/2$, $\Delta y/2$, $\Delta z/2$, and $\Delta t/2$, respectively.

To derive the expressions for solving Eq. (2.7) we consider first an arbitrary function depending on space and time $f = f(\boldsymbol{r}, t)$ whose functional characteristics are known on each grid point

$$f(\boldsymbol{r}, t) \longrightarrow f|_{i,j,k}^{n} \equiv f(i\Delta x, j\Delta y, k\Delta z, n\Delta t). \tag{2.9}$$

One may write down a Taylor's series expansion of f about, e.g., the space point i to $i \pm 1/2$ keeping the other variables fixed. Expanding to linear order yields

$$f|_{i\pm 1/2,j,k}^{n} = f|_{i,j,k}^{n} \pm \frac{\Delta x}{2} \left. \frac{\partial f}{\partial x} \right|_{i,j,k}^{n} + \mathcal{O}\left(\Delta x^2\right). \tag{2.10}$$

Hence, the centered finite-difference expression for the derivative with respect to x has the form

$$\left. \frac{\partial f}{\partial x} \right|_{i,j,k}^{n} = \frac{f|_{i+1/2,j,k}^{n} - f|_{i-1/2,j,k}^{n}}{\Delta x} + \mathcal{O}\left(\Delta x^2\right). \tag{2.11}$$

Applying this scheme to the component E_x for all space- and time-derivatives in Eq. (2.7) gives

$$\frac{E_x|_{i,j+1/2,k+1/2}^{n+1/2} - E_x|_{i,j+1/2,k+1/2}^{n-1/2}}{\Delta t} = \frac{1}{\epsilon|_{i,j+1/2,k+1/2}}$$

$$\times \left(\frac{H_z|_{i,j+1,k+1/2}^{n} - H_z|_{i,j,k+1/2}^{n}}{\Delta y} - \frac{H_y|_{i,j+1/2,k+1}^{n} - H_y|_{i,j+1/2,k}^{n}}{\Delta z} \right). \tag{2.12}$$

Finally, if one assumes an equally discretized grid in all three space dimensions, i.e., $\Delta r \equiv \Delta x = \Delta y = \Delta z$, one obtains a compact expression for E_x

$$E_x|_{i,j+1/2,k+1/2}^{n+1/2} = E_x|_{i,j+1/2,k+1/2}^{n-1/2} + \frac{\Delta t}{\Delta r \, \epsilon|_{i,j+1/2,k+1/2}}$$

$$\times \left(H_z|_{i,j+1,k+1/2}^{n} - H_z|_{i,j,k+1/2}^{n} - H_y|_{i,j+1/2,k+1}^{n} + H_y|_{i,j+1/2,k}^{n} \right). \tag{2.13}$$

The equations for the components E_y and E_z as well as H_x, H_y, and H_z are derived in an analog way and are given for completeness in appendix A.1. Inspecting the time arguments in Eq. (2.13) one sees that the "new" value of E_x at time $t = n + 1/2$ depends on its "old" value at earlier time $t - \Delta t = n - 1/2$ and the values of the surrounding $\boldsymbol{H}$-fields at intermediate time $t - \Delta t/2 = n$. Also,

every novel $\boldsymbol{H}$-field component can be computed knowing its previous value and the current $\boldsymbol{E}$-fields located around.

Thinking in terms of a computer code one recognizes that it is sufficient to merely store in memory $\boldsymbol{E}$ and $\boldsymbol{H}$ matrices for the current value which can be updated in the next cycle not needing any auxiliary variables. Furthermore, the algorithm can be parallelized in a straightforward way since the computation at a certain grid point involves only its neighbors. That is why one can divide the whole simulation space into different regions that can be processed individually and solely the information at the boundaries has to be exchanged. In order to get a stable numerical solution of the Eq. (2.13) it is necessary to fulfill the Courant-condition [36] which means that time-stepping in three dimensions has at least to be resolved like

$$c\Delta t \leq \left(\frac{1}{(\Delta x)^2} + \frac{1}{(\Delta y)^2} + \frac{1}{(\Delta z)^2} \right)^{-1/2} \tag{2.14}$$

turning into

$$t \leq \frac{\Delta r}{c\sqrt{3}} \tag{2.15}$$

for an equal discretization of each space direction. Here, c is the speed of light in vacuum. Since the spacial resolution of the photonic crystal will be on the order of some nanometers the time steps must be in the attosecond range.

2.1.2 Tailoring the FDTD-Method

The standard FDTD algorithm presented in subsection 2.1.1 has to be adapted in order to make it usable for the investigated structures. One major problem is that if one wants to compute the field component at a given grid point one needs the information about the values of the components of the four surrounding grid points and so forth. Strictly speaking, one would have to use an infinite grid for the purpose of simulating the evolution of electromagnetic fields properly. Clearly, no computer can store an unlimited amount of data, and therefore, the field computation domain must be limited in size. But since no information about the "outside-world" is available at the boundaries of the simulation space one might get an undesirable behavior at these space points.

Suppose, an electromagnetic wave travels in an one-dimensional scenario to the right as depicted in the upper row of Fig. 2.3(a)-(d). If one just limits the simulation space at a certain grid point (marked gray) one of the neighbor grid points of the corresponding 1-d equation of Eq. (2.13) are forced to be equal to zero, meaning that the boundary acts as perfectly reflecting metal, see top right
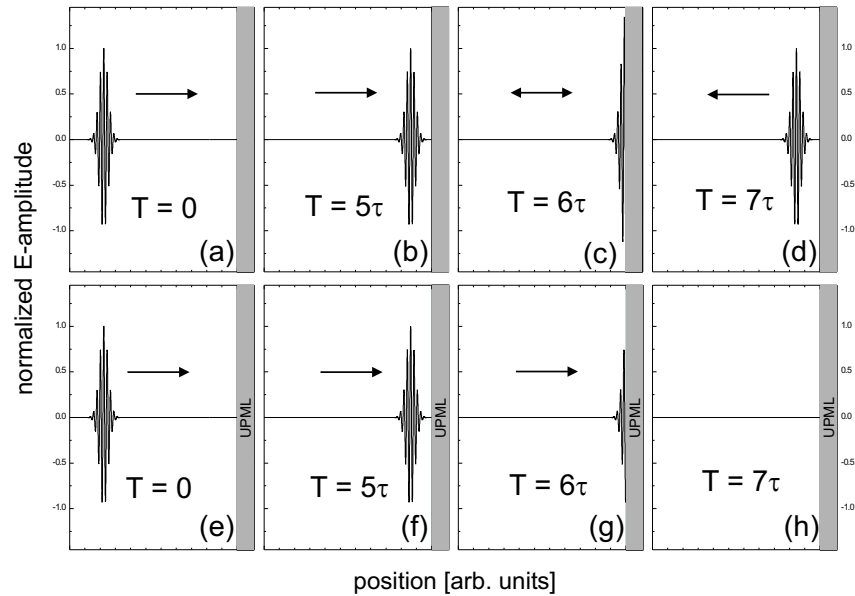
Figure 2.3: 1d-FDTD calculation. Upper row (a)-(d): The simulation space is truncated at the gray region resulting in a total reflection of the pulse. Lower row (e)-(h): The UPML-absorbing-boundary condition are used at the gray region which damp the impinging waves and for this reason simulate the extension of the lattice to infinity. The arrows indicate the propagation direction of the pulse.

picture in Fig. 2.3(d). That is the reason why for $T = 7\tau$ the initial wave has been reflected completely.

There exist in principle two methods to circumvent this effect. Either the simulation domain is simply enlarged in such a way that the reflecting waves do not affect the results in a defined region of interest. Of course, this solution may require a lot of computer memory, especially when the simulation time is long – e.g. to propagate spectrally narrow pulses – which means that one has to choose a very large computational domain. Whereas a more sophisticated treatment is to introduce some absorbing boundary conditions which damp the impinging wave to (almost) zero. In this case it looks like the wave is leaving the computational domain because no reflection at the outmost points occurs. There are different absorbing boundary conditions (ABC) which can be incorporated into the FDTD-code, for example the Mur-ABC or the uniaxial perfectly matched layer ABC (UPML) are commonly applied [37]. Whereas the Mur-condition falls into the category of analytical boundary conditions, i.e., an expression for the fields at the outer domain is derived from the known interior fields to annihilate the reflecting wave [36, 39],

the UPML-layers act as lossy material and damp the electromagnetic waves.

In the following the UPML-method is used [37, 40]. Although the implementation of such a kind of absorbing-material is quite memory consuming it has the advantage of being applicable to arbitrarily impinging light and, above all, the approach has been shown to provide significantly better accuracy than most other ABCs [37]. Furthermore, it turned out to be quite robust for three-dimensional problems. The concept is based on the assumption that the boundaries of the simulation space are surrounded by an anisotropic absorbing material which can be described by a general permittivity and permeability tensor. The requirement that no part of the wave is reflected when impinging on the artificial material leads to a particular form of these tensors. For instance, it can be analytically shown [36] that the reflection vanishes for a wave traveling in x-direction if the boundary material consists of a medium for which

$$
\underline{\underline{\epsilon}} = \epsilon \underline{\underline{s_x}} \quad , \underline{\underline{\mu}} = \mu \underline{\underline{s_x}} \quad , \text{ and } \quad \underline{\underline{s_x}} = \begin{pmatrix} s_x^{-1} & 0 & 0 \\ 0 & s_x & 0 \\ 0 & 0 & s_x \end{pmatrix} \tag{2.16}
$$

hold. Here, s_x is an arbitrary number. One can get a general three-dimensional tensor $\underline{\underline{s}}$ by recognizing that

$$
\begin{aligned}
\underline{\underline{s}} &= \underline{\underline{s_x}} \cdot \underline{\underline{s_y}} \cdot \underline{\underline{s_z}} \\
&= \begin{pmatrix} s_x^{-1} & 0 & 0 \\ 0 & s_x & 0 \\ 0 & 0 & s_x \end{pmatrix} \cdot \begin{pmatrix} s_y & 0 & 0 \\ 0 & s_y^{-1} & 0 \\ 0 & 0 & s_y \end{pmatrix} \cdot \begin{pmatrix} s_z & 0 & 0 \\ 0 & s_z & 0 \\ 0 & 0 & s_z^{-1} \end{pmatrix} \\
&= \begin{pmatrix} s_x^{-1} s_y s_z & 0 & 0 \\ 0 & s_x s_y^{-1} s_z & 0 \\ 0 & 0 & s_x s_y s_z^{-1} \end{pmatrix} .
\end{aligned} \tag{2.17}
$$

This generalized constitutive tensor is, of course, rather anisotropic but uniaxial. However, since in the nonoverlapping regions of the limiting borders only one of the numbers s_x, s_y, or s_z differs from unity, it is commonly still referred to as "uniaxial".

The ideal behavior of a complete non-reflecting crossover between the simulation space and the surrounding material can only be achieved in a continuous real space. If the tensors are discretized on a grid, again some spurious reflection will occur. However, it has been proven that the fraction of the returning wave is at least 5 orders of magnitude smaller than the original wave if the parameters s_x, s_y, and s_z are chosen adequately for the respective grid. The deviation of these parameters from unity determine the quality of the absorbing material, see comment about Eq. (A.7) on page 85. To obtain a finite-difference formulation of the method the special permittivity and permeability tensors can be matched

with Maxwell's equations resulting not only in equations for $\boldsymbol{E}$ and $\boldsymbol{H}$ but due to the artificial boundary medium also for $\boldsymbol{D}$ and $\boldsymbol{B}$. An explicit derivation of the FDTD-UPML equations can be found, e.g., in Refs. [36, 41]. In appendix A.2 the relations between the components $\boldsymbol{D}_x$ and $\boldsymbol{E}_x$ are briefly discussed. Altogether, the numerical demands are increased because twice as many equations have to be solved and the computational domain has to be enlarged to also include the absorbing material. From the introduction above it becomes transparent that for $s_x = s_y = s_z = 1$ the standard FDTD-equations Eqs. (A.1)-(A.6) are recovered.

   The result of implementing the UPML-layers can be clearly seen in the lower row of Fig. 2.3(e)-(h). In contrast to the upper row the electromagnetic wave is completely damped and not reflected from the boundary.

   Another important issue of FDTD modeling is the introduction of electromagnetic waves into the discrete lattice. In principle, there are two straightforward ways of how to create a wave source in the simulation domain but both turn out to have serious disadvantages. First, it seems feasible to calculate analytically the initial field distribution for every $\boldsymbol{E}$- and $\boldsymbol{H}$-component, insert it into the grid, and then just let the system develop in time according to Eqs. (A.1)-(A.6). The shortcoming of this method is that in fact a huge lattice is needed when dealing with spreading pulses. Since it is impossible to assign the source's values only to a few grid points but one rather has to resolve the whole spatial distribution of the incoming pulse, this solution is impractical for most initial conditions. Therefore, a second elementary approach which keeps the simulation space small would be using a so called *hard source*, i.e., to specify certain space positions at which the time-development of the source is enforced. For instance, in an one-dimensional scenario the source's value $s = s(t)$ is assigned to the location i_s

$$E\big|_{i_s}^n = s(n\Delta t) \,. \tag{2.18}$$

The drawbacks of this method can be seen in the upper row of Fig. 2.4(a)-(d) where the simulation domain has been divided into two regions: the white region illustrating vacuum and the gray one illustrating a dielectric with a dielectric constant $\epsilon > 1$. Again, the waves at the boundaries are damped due to UPML-layers described in the previous paragraph. If the source is inserted into the grid via a hard-source Eq. (2.18) the resulting wave propagates bilaterally in both directions from the source point, cp. Fig. 2.4(a). In Fig. 2.4(b) it is shown that part of the wave is reflected when reaching the dielectric and another part keeps on traveling in the material. The reflected wave reaches the source point i_s again after some time and cannot evolve according to the common FDTD-equations since the time-behavior is determined by Eq. (2.18). In a sense the constraint of the source divides the simulation space into two non-interacting subspaces. This leads to a spurious, nonphysical retroreflection at i_s, see Fig. 2.4(c) which avoids that the wave propagates to the "left". For that reason there still is some signal present

in Fig. 2.4(d) although every partial-wave should have left the computational do-
main at that point in time. Note also, that the spurious reflection generally makes
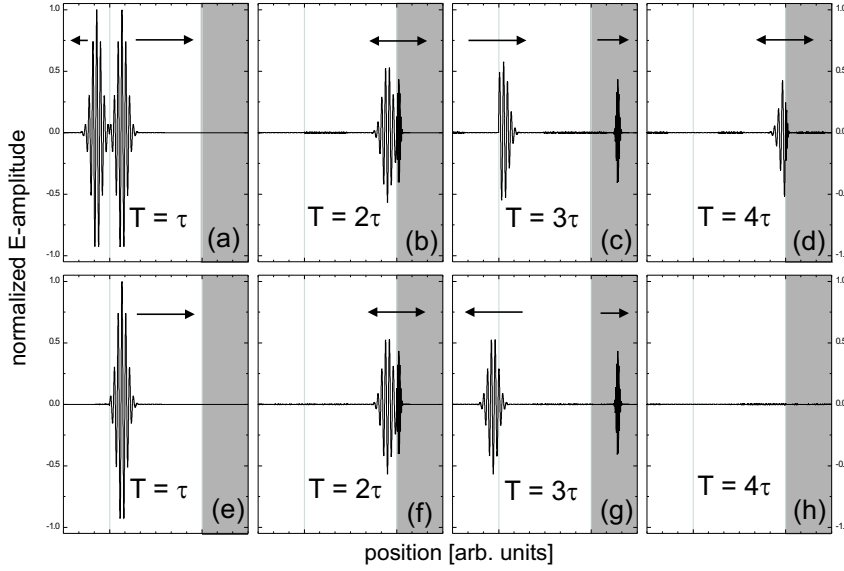it impossible to identify the reflected and transmitted part of the incident wave.

Figure 2.4: 1d-FDTD calculation. Upper row (a)-(d): The wave is introduced into the
lattice using a hard source Eq. (2.18). Lower row (e)-(h): Time evolution of the pulse
if the total-field scattered-field technique is applied. The arrows indicate the propagation
direction of the pulse.

All these problems are resolved using the *total field / scattered-field* (TF/SF)
technique. This method not only allows for a correct introduction of the elec-
tromagnetic fields into the lattice resulting in an unilaterally traveling wave, but
also suppresses any retroflection at i_s. The proper evolution of a pulse is shown
in Fig. 2.4(e)-(h): the wave starts propagating only to the "right", impinges on a
dielectric and then its reflected part leaves the computational domain to the "left".

The TF/SF approach makes use of the linearity of Maxwell's equations. It
assumes that the electromagnetic fields can be decomposed in the manner

$$\boldsymbol{E}_{\text{total}} = \boldsymbol{E}_{\text{incident}} + \boldsymbol{E}_{\text{scattered}} \quad \text{and} \tag{2.19}$$

$$\boldsymbol{H}_{\text{total}} = \boldsymbol{H}_{\text{incident}} + \boldsymbol{H}_{\text{scattered}} \quad . \tag{2.20}$$

Here, *incident* stands for the fields which originate from the radiation source itself
and *scattered* accounts for the fields which result from the interaction of the in-
cident wave with any material. Whereas the values of $\boldsymbol{E}_{\text{incident}}$ and $\boldsymbol{H}_{\text{incident}}$ are
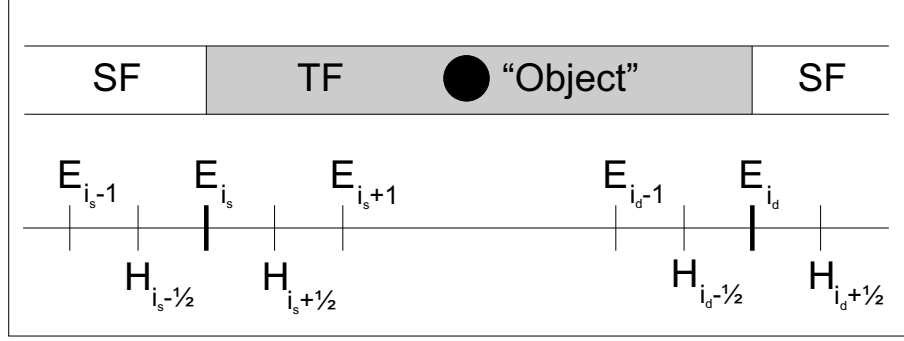
Figure 2.5: Schematic sketch of the total-field scattered-field space-partitioning: The TF region contains the incident as well as the (from the object) scattered field, the SF region only the scattered field itself. In the respective regions the standard FDTD-code can be applied, however, at the interfaces the fields have to be matched according to Eq. (2.22).

known for all grid points and at all times the scattered fields depend on the scattering object and are initially unknown. The principle of the technique is sketched in Fig. 2.5 for an one-dimensional situation: The simulation space consists of two regions namely "TF" for the total fields and "SF" for the scattered fields which are connected at the virtual interfaces i_s and i_d. If all components $i, i \pm 1/2$, which are involved to compute a new time-step value, are located inside one of the regions the conventional FDTD algorithm can be applied. Written as a functional, e.g., for the $\boldsymbol{E}$-field it holds that

$$
\begin{aligned}
\boldsymbol{E}|^{n+1}_{i,\text{scattered}} &= \boldsymbol{E}|^{n+1}_{i,\text{scattered}}\left[\boldsymbol{E}|^n_{i,\text{scattered}}, \boldsymbol{H}|^{n+1/2}_{i+1/2,\text{scattered}}, \boldsymbol{H}|^{n+1/2}_{i-1/2,\text{scattered}}\right], \\
\boldsymbol{E}|^{n+1}_{i,\text{total}} &= \boldsymbol{E}|^{n+1}_{i,\text{total}}\left[\boldsymbol{E}|^n_{i,\text{total}}, \boldsymbol{H}|^{n+1/2}_{i+1/2,\text{total}}, \boldsymbol{H}|^{n+1/2}_{i-1/2,\text{total}}\right].
\end{aligned}
$$

$$(2.21)$$

However, if components from different regions are needed for the computation a correction is required to make a consistent connection at the interface, e.g., at i_s

$$
\begin{aligned}
\boldsymbol{E}|^{n+1}_{i_s,\text{total}} &= \\
\boldsymbol{E}|^{n+1}_{i_s,\text{total}}&\left[\boldsymbol{E}|^n_{i_s,\text{total}}, \boldsymbol{H}|^{n+1/2}_{i_s+1/2,\text{total}}, \left(\boldsymbol{H}|^{n+1/2}_{i_s-1/2,\text{scattered}} + \boldsymbol{H}|^{n+1/2}_{i_s-1/2,\text{incident}}\right)\right].
\end{aligned}
$$

$$(2.22)$$

In this way not only a proper description for the TF as well as the SF region is achieved, but it is also possible to use the connecting interface to radiate an arbitrary incident plane wave into the TF-region. Finally, this leads to the desired behavior shown in Fig. 2.4(e)-(h). The method can be extended straightforwardly to the three-dimensional case.

2.1.3   Inclusion of the Polarization

In subsections 2.1.1 and 2.1.2 basic principles of numerically solving the electromagnetic-field equations (2.7)-(2.8) are discussed. To account for the full problem, namely a proper description of the combined photonic-crystal semiconductor system, also the material properties have to be included, i.e., Eq. (2.5) has to be used. Mostly, the FDTD-code is exclusively applied to simulate passive dielectric structures and sometimes relative simple materials, which, e.g., can be modeled by two-level systems [36, 41–43], are incorporated into the algorithm. In the present work the transverse optical polarization $P(r, t)$ is determined by a more sophisticated microscopic theory which is introduced in section 2.2 and appropriately describes the active semiconductor material. However, in the remainder of this subsection, general aspects of the light-matter coupling are illustrated with the help of two-level systems. In either case the polarization equation itself is driven by the electric field, cp. Eq. (2.24) and Eq. (2.44) on page 27. Integrating all equations simultaneously allows for a self-consistent treatment of the coupled dynamics of the electromagnetic field and the material excitations.

It is straightforward to approximate the time derivative of the polarization entering Eq. (2.5) with a finite difference, Eq. (2.11), too. Thus, resolving the time evolution of P on the same time scale as the electromagnetic fields, Eq. (2.13) is extended to

$$
\begin{aligned}
E_x\big|_{i,j+1/2,k+1/2}^{n+1/2} &= E_x\big|_{i,j+1/2,k+1/2}^{n-1/2} + \frac{\Delta t}{\Delta r\ \epsilon\big|_{i,j+1/2,k+1/2}} \\
&\times \left(H_z\big|_{i,j+1,k+1/2}^{n} - H_z\big|_{i,j,k+1/2}^{n} - H_y\big|_{i,j+1/2,k+1}^{n} + H_y\big|_{i,j+1/2,k}^{n} \right) \\
&- \frac{1}{\epsilon\big|_{i,j+1/2,k+1/2}} \left(P_x\big|_{i,j+1/2,k+1/2}^{n+1/2} - P_x\big|_{i,j+1/2,k+1/2}^{n-1/2} \right) .
\end{aligned}
\tag{2.23}
$$

Under certain conditions it is, however, possible to compute the material equations on a much coarser time-resolution.[4] Possibly, the values of P at times $n \pm 1/2$ shall be obtained by means of interpolation or extrapolation.

In the standard FDTD-code the E and H fields are calculated alternately in a leap frog type manner. Now, also the polarization P has to be included into this cycle. The approach is schematically sketched in Fig. 2.6: The E-field not only determines the next time step value of the H-field but also of P. Then, both these quantities affect in turn the computation of E. The time integration of the polarization equation may be carried out with different routines depending on the terms which actually appear at its right hand side. For the numerical calculation

---

[4]For example, applying the rotating wave approximation (RWA) [44] reduces the numerical complexity.
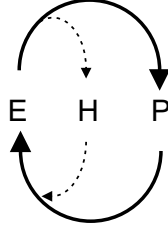
Figure 2.6: Self-consistent calculation scheme for the electromagnetic fields $\boldsymbol{E}$ and $\boldsymbol{H}$ and the material equations $\boldsymbol{P}$ as described in the text.

of the material Eq. (2.24) and Eq. (2.44) we use the fourth-order Runge-Kutta method or the Leapfrog algorithm [45].

To verify the correctness of the approach we consider a simple quantum-well model consisting of two level systems (TLS). Therefore, on each grid point in the x-y-plane the polarization equation[5] for a TLS [46]

$$\frac{\partial}{\partial t}\left.P\right|_{i,j,k=0} = i\omega_g \left.P\right|_{i,j,k=0} - \frac{i}{\hbar}\boldsymbol{\mu} \cdot \left.\boldsymbol{E}\right|_{i,j,k=0} \tag{2.24}$$

is solved. Here, $\hbar\omega_g$ is the transition energy which is chosen to be resonant with the incident field and $\boldsymbol{\mu}$ is the dipole matrix element. If the TLS are excited with a short pulse centered around $t = 0$ and the polarization is *not* fed back into the FDTD-lattice, then, of course, the absolute value of the polarization increases and stays at a constant value after the pulse is over, see Fig. 2.7(a). However, if one allows for the self-consistent coupling of the electromagnetic fields and the polarization, P_{ij} decays radiatively as can be seen in Fig. 2.7(b). It is known from analytical considerations [41] that $P(t)$ described via Eq. (2.24) should decay like

$$P(t) \quad \propto \quad \exp(-\Gamma_{\text{rad}} \cdot t) \quad \text{with} \tag{2.25}$$

$$\Gamma_{\text{rad}} \quad = \quad \frac{\omega_g \mu^2}{2\epsilon_0 c\hbar a_0^2} \tag{2.26}$$

for an ideal infinitesimal thin quantum well which consists of TLS. Hence, using Eq. (2.23) in combination with an integration routine for P yields the expected result $\Gamma_{\text{rad}} = 2.66$ ps for the parameters given in appendix D.1.

2.1.4   Observables in the Simulation Space

Although the intrinsic properties of the semiconductor material definitely determine the behavior of the polarization equation the numerical simulations in sec-

---

[5]In general, $\boldsymbol{P}$ is a vector. In the following, the exciting light field is linearly polarized in x-direction, thus the calculation of one component, $P \equiv P_x$, is sufficient.
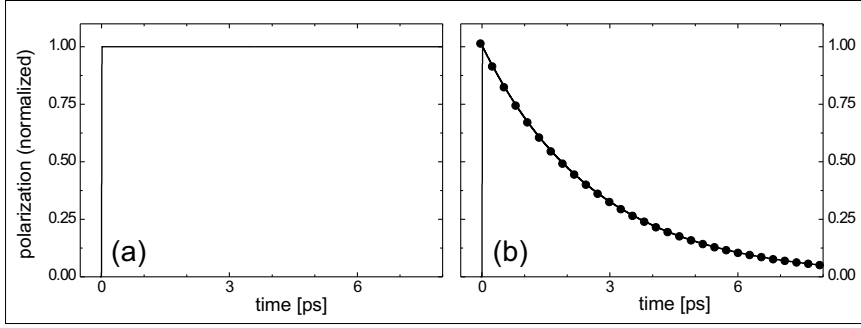
Figure 2.7: Exemplary study for the polarization Eq. (2.24) whose absolute value (a) stays constant if the P-equation Eq. (2.24) is solved with only the FDTD-$\boldsymbol{E}$ field as input, and (b) decays radiatively if all equations for $\boldsymbol{E}$, $\boldsymbol{H}$, and P are solved self-consistently. The dots indicate the analytical solution Eq. (2.25).

tion 2.3 use merely the electromagnetic fields as observables. Therefore, the structure is illuminated with an incoming plane wave $\boldsymbol{E}_{\mathrm{inc}}$ which is polarized along the quantum wires in x-direction and propagates in negative z-direction. The reflected and transmitted part of the $\boldsymbol{E}$- and $\boldsymbol{H}$-field are recorded for all times at the boundaries of the simulation space. The net flux through these boundaries with normal vector $\boldsymbol{n}$ is

$$\dot{W}_{\mathrm{refl/trans}} = \int d\sigma\, \boldsymbol{n}_{\mathrm{refl/trans}} \cdot \boldsymbol{S}_{\mathrm{refl/trans}} , \tag{2.27}$$

where $\boldsymbol{S} = \boldsymbol{E} \times \boldsymbol{H}$ is the Poynting vector, and contains all information about absorbed or gained energy per unit time since it holds that

$$W_{\mathrm{inc}} + W_{\mathrm{absorbed}} = W_{\mathrm{refl}} + W_{\mathrm{trans}} . \tag{2.28}$$

Here, $W = \int dt\, \dot{W}$ is the total net flux over all times. Transforming the fields into Fourier space allows one to obtain the semiconductor absorption spectrum as

$$\alpha(\omega) = 1 \; - \; \frac{\int d\sigma\, \boldsymbol{n}_{\mathrm{refl}} \cdot [\boldsymbol{E}_{\mathrm{refl}}(\omega, \boldsymbol{r}) \times \boldsymbol{H}_{\mathrm{refl}}(\omega, \boldsymbol{r})]}{\int d\sigma\, \boldsymbol{n}_{\mathrm{inc}} \cdot [\boldsymbol{E}_{\mathrm{inc}}(\omega, \boldsymbol{r}) \times \boldsymbol{H}_{\mathrm{inc}}(\omega, \boldsymbol{r})]}$$
$$- \; \frac{\int d\sigma\, \boldsymbol{n}_{\mathrm{trans}} \cdot [\boldsymbol{E}_{\mathrm{trans}}(\omega, \boldsymbol{r}) \times \boldsymbol{H}_{\mathrm{trans}}(\omega, \boldsymbol{r})]}{\int d\sigma\, \boldsymbol{n}_{\mathrm{inc}} \cdot [\boldsymbol{E}_{\mathrm{inc}}(\omega, \boldsymbol{r}) \times \boldsymbol{H}_{\mathrm{inc}}(\omega, \boldsymbol{r})]} \; . \tag{2.29}$$

A more technical description in terms of the FDTD-simulation is given in Fig. 2.8. First of all, during the numerical calculation it is sufficient to consider only one unit cell since due to the two-dimensional periodicity of the photonic crystal in the x-y-plane it is possible to apply periodic boundary conditions in
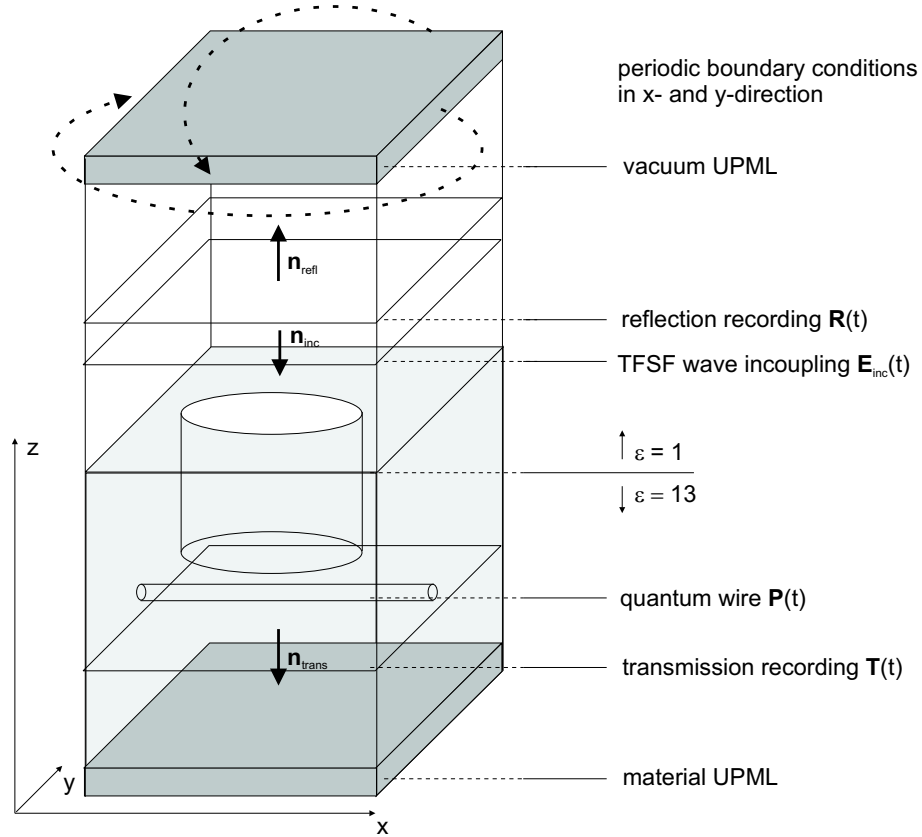
Figure 2.8: Setup and observables of the FDTD-simulation space. Explanation is given in the text.

these directions. The laser pulse, which is used for the investigation of the structure, is coupled into the lattice with the help of the TF-SF technique. This ensures that the exciting pulse solely travels in negative z-direction towards the photonic crystal and that all other waves pass unhamperedly the TF-SF plane. For this reason, the reflected part of the signal will reach the position marked as "reflection recording" and afterwards be damped to zero by the vacuum UPML absorbing boundary conditions assuring that $R(t)$ measures exclusively the reflected field. The same is true for $T(t)$: after going through the passive photonic crystal structure and interacting with the quantum wire the E and H fields are quantified at the "transmission recording" plane and absorbed by the material UPML. Having the values for $R(t)$, $T(t)$, and $E_{\text{inc}}(t)$ allows to determine the semiconductor absorption via formula Eq. (2.29).

Apparently, due to the UPML every reflected or transmitted signal is immediately absorbed after being recorded at its respective position. However, it should

be noted that a simulation run has to last considerably longer than the temporal width of the exciting pulse plus its pure travel-time due to the extension of the structure. On the one hand the polarization of the quantum wire, which is driven by the external field, decays on a slower time scale as compared to the exciting pulse and re-radiates a wave during that period. On the other hand the electromagnetic field may stay longer in a periodic crystal structure due to internal reflections at the interfaces between different dielectric constant ϵ [47]. Note, that the simple setup of the simulation space, Fig. 2.8, can only be used because of periodic boundary conditions and a normal incident plane wave. Otherwise the modeling would be much more complex.

2.2   The Quantum Wire in a Photonic Crystal

In subsection 2.2.1 the properties of the longitudinal part of the electromagnetic field, i.e., the Coulomb interaction, in a photonic crystal are discussed.[6] This modified potential enters the Hamiltonian describing the quantum wire which is presented in subsection 2.2.2. Finally, the equations of motion are derived in subsection 2.2.3.

2.2.1   The Modified Coulomb Interaction

It can be seen readily from the situation in Fig. 2.9(a) that the common Coulomb potential in a homogeneous dielectric

$$V_0(\boldsymbol{r}, \boldsymbol{r}') = V_0(|\boldsymbol{r} - \boldsymbol{r}'|) = \frac{1}{4\pi\epsilon_r\epsilon_0} \frac{1}{|\boldsymbol{r} - \boldsymbol{r}'|} \tag{2.30}$$

is altered when an interface is introduced, e.g., if two semi-infinite half-spaces with different dielectric constants are considered. Then, for a unit charge placed in region 1 Eq. (2.30) has to be corrected by [49]

$$\delta V(\boldsymbol{r}, \boldsymbol{r}_1) = \frac{1}{4\pi\epsilon_0} \frac{1}{\epsilon_1} \frac{\epsilon_1 - \epsilon_2}{\epsilon_1 + \epsilon_2} \frac{1}{\sqrt{(\boldsymbol{r} - \boldsymbol{r}_1)^2 + 4D^2}} \quad . \tag{2.31}$$

In Fig. 2.9(a), q denotes the test unit charge located at $\boldsymbol{r}$ and q_1 the source unit charge at $\boldsymbol{r}_1$. Both charges are placed in a region with dielectric constant ϵ_1 which is separated from another medium (region 2) via the plane ∂G_{12}. If the parameter D, i.e., the distance of the charges from the interface, is increased, the correction δV to the usual Coulomb potential becomes smaller. The symbol q_1' indicates that the expression Eq. (2.31) may be obtained via the image charge method [50].

Analogous for the photonic-crystal structure in Fig. 2.9(b) the Coulomb potential is modified because additional contributions which originate from induced surface polarizations at the interfaces have to be included. It has been shown in Ref. [21] that for such structures the generalized Coulomb potential V^C can be written as

$$
\begin{aligned}
V^C(\boldsymbol{r}, \boldsymbol{r}') &= V_0(\boldsymbol{r}, \boldsymbol{r}') + \delta V(\boldsymbol{r}, \boldsymbol{r}') \\
&= \frac{1}{4\pi\epsilon_0\epsilon(\boldsymbol{r}')} \frac{1}{|\boldsymbol{r} - \boldsymbol{r}'|} \\
&\quad - \frac{1}{4\pi\epsilon_0} \sum_{ij} \left(\frac{1}{\epsilon_i} - \frac{1}{\epsilon_j} \right) \int_{\partial D_{ij}} da'' \frac{1}{|\boldsymbol{r}'' - \boldsymbol{r}|} \boldsymbol{n}_i'' \cdot \boldsymbol{D}_i^L(\boldsymbol{r}'', \boldsymbol{r}') .
\end{aligned}
\tag{2.32}
$$

---

[6]A detailed derivation of the modified Coulomb interaction in a photonic crystal environment can be found in Refs. [24, 48].
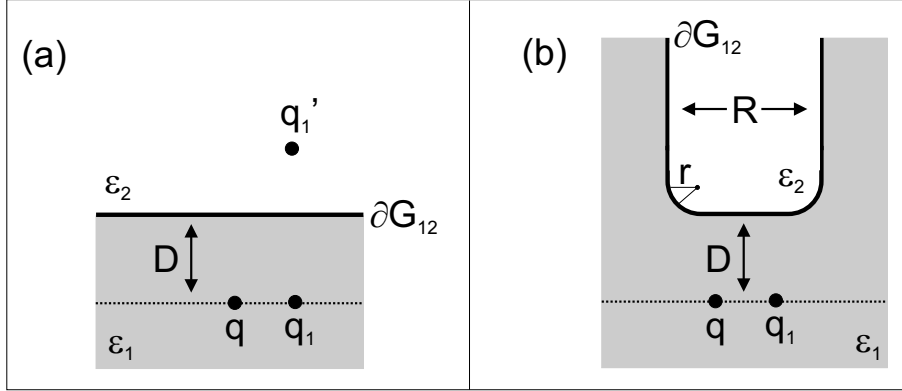
Figure 2.9: (a) Basic concept with two regions containing different dielectric media which are separated by a planar interface leading to an altered Coulomb interaction. (b) The same effects also arise in a photonic crystal. The region with dielectric constant ϵ_i is referred to as "region i" in the text.

Here, $\boldsymbol{D}_i^L$ is the dielectric displacement field and the indices i and j label the volumes of different dielectric constants ϵ_i and ϵ_j, respectively. ∂D_{ij} denotes the boundary area between two such volumes, and $\boldsymbol{n}_i$ is the surface normal at $\boldsymbol{r}''$. To calculate V^C, the dielectric displacement field $\boldsymbol{D}_i^L$ at the interfaces has to be known. This can be achieved by deriving an integral equation for $\boldsymbol{D}_i^L$ [48] which can be solved numerically for the designated geometries. Inserting the solution into Eq. (2.32), the generalized Coulomb potential V^C can be obtained in all regions of interest. Note, that in the case of a spatially inhomogeneous dielectric environment the potential V^C depends explicitly on the two coordinates $\boldsymbol{r}$ and $\boldsymbol{r}'$ of the interacting particles and not only on their relative distance $|\boldsymbol{r} - \boldsymbol{r}'|$. A brief derivation of Eq. (2.32) is given in appendix B.

2.2.2 The Material Hamiltonian

The microscopic properties of the semiconductor which is embedded in the photonic crystal system is described by the standard Hamiltonian [44]

$$\hat{H} = \hat{H}_{\text{single-particle}} + \hat{H}_{\text{Coulomb}} + \hat{H}_{\text{light-matter}}. \tag{2.33}$$

It contains the band-structure part of the quasi particles $\hat{H}_{\text{single-particle}}$, the many-body Coulomb interaction among the charge carriers close to a photonic crystal $\hat{H}_{\text{Coulomb}}$, and $\hat{H}_{\text{light-matter}}$ specifying the interaction of the semiconductor with a classical electromagnetic field which is calculated according to section 2.1.

For the inhomogeneous situation in a photonic crystal it is advantageous to write down the Hamilton operator in a real-space basis. Here, we use the electron

and hole creation (annihilation) operators $\hat{c}_1^+$ ($\hat{c}_1$) and $\hat{d}_1^+$ ($\hat{d}_1$), respectively, which create (destroy) a quasi particle at position $\boldsymbol{r}_1$. From now on, the space-dependent quantities are denoted by a shorthand notation via indices, e.g., $V_{12}^C \equiv V^C(\boldsymbol{r}_1, \boldsymbol{r}_2)$.

The single-particle part of the Hamiltonian describes the quasi-free motion of the electrons and the holes in effective mass approximation and reads

$$\hat{H}_{\text{single-particle}} \;=\; \int d\boldsymbol{r}_1 \left[\hat{c}_1^+ \left(E_{\text{gap}} - \frac{\hbar^2 \nabla_1^2}{2m_e} \right) \hat{c}_1 + \hat{d}_1^+ \left(-\frac{\hbar^2 \nabla_1^2}{2m_h} \right) \hat{d}_1 \right] . \tag{2.34}$$

Here, E_{gap} denotes the band-gap energy and m_e and m_h are the effective masses of the electrons and holes, respectively. For simplicity, we restrict ourselves to a treatment of a two-band situation where only a single conduction band and a single valence band is considered. This is sufficient to demonstrate the effects of the photonic environment on the material excitations. In principle, it is straightforward to extend the approach to a multi-band formalism, but then the numerical calculations would become more demanding.

The generalized Coulomb interactions V^C which has been given in subsection 2.2.1 enters the many-body part of the Hamiltonian

$$\hat{H}_{\text{Coulomb}} \;=\; \frac{e^2}{2} \int d\boldsymbol{r}_1 \int d\boldsymbol{r}_2 \, V_{12}^C \left(\hat{c}_1^+ \hat{c}_2^+ \hat{c}_2 \hat{c}_1 + \hat{d}_1^+ \hat{d}_2^+ \hat{d}_2 \hat{d}_1 - 2\hat{c}_1^+ \hat{d}_2^+ \hat{d}_2 \hat{c}_1 \right)$$
$$+ \frac{e^2}{2} \int d\boldsymbol{r}_1 \delta V_{11} (\hat{c}_1^+ \hat{c}_1 + \hat{d}_1^+ \hat{d}_1) . \tag{2.35}$$

It describes the repulsive interaction among electrons (terms $\propto \hat{c}^+ \hat{c}^+ \hat{c}\hat{c}$) and holes ($\propto \hat{d}^+ \hat{d}^+ \hat{d}\hat{d}$) as well as the attractive interaction between them ($\propto \hat{c}^+ \hat{d}^+ \hat{d}\hat{c}$). Additionally to the true many-body parts in the first line, Eq. (2.35) contains single-particle terms in the last line which stem from induced interface polarizations of the photonic crystal. In the case of a planar interface this corresponds to a self-interaction with an image charge, whereas in a homogeneous medium these contributions disappear.

For future analysis it is convenient to incorporate all single-particle terms into the single-particle Hamiltonian, i.e., to define

$$\hat{H}_{\text{effective-single-particle}} = \hat{H}_{\text{single-particle}} + \frac{e^2}{2} \int d\boldsymbol{r}_1 \delta V_{11}(\hat{c}_1^+ \hat{c}_1 + \hat{d}_1^+ \hat{d}_1) \tag{2.36}$$

and

$$\hat{H}_{\text{many-body}} = \hat{H}_{\text{Coulomb}} - \frac{e^2}{2} \int d\boldsymbol{r}_1 \delta V_{11}(\hat{c}_1^+ \hat{c}_1 + \hat{d}_1^+ \hat{d}_1) . \tag{2.37}$$

In this way, it can be seen that the electrons and holes in the system move in an additional potential which is spatially varying like the dielectric environment. One can then solve the Schrödinger equation with Eq. (2.36) by calculating Bloch-type eigenfunctions and, e.g., analyze the density-dependent absorption in quasi-equilibrium situations as done in subsection 2.3.2.

The light-matter interaction is treated semiclassically and is given in dipole approximation by

$$\hat{H}_{\mathrm{light-matter}} = -\int d\boldsymbol{r}_1 \boldsymbol{E}_1(t) \cdot \boldsymbol{\mu}_{eh}(\hat{d}_1\hat{c}_1 + \hat{c}_1^+\hat{d}_1^+)$$
$$= -\int d\boldsymbol{r}_1 \boldsymbol{E}_1(t) \cdot \hat{\boldsymbol{P}}_1. \qquad (2.38)$$

Here, $\boldsymbol{E}(t)$ is the transverse part of the electromagnetic field and $\boldsymbol{\mu}$ is the interband dipole matrix element which is taken to be a space-independent real number. The polarization density $\boldsymbol{P}(\boldsymbol{r}_1) = \langle\hat{\boldsymbol{P}}_1\rangle$ enters Maxwell's equation Eq. (2.5) and also determines the total optical polarization of the material system

$$\boldsymbol{P} = \int d\boldsymbol{r}_1 \boldsymbol{P}(\boldsymbol{r}_1). \qquad (2.39)$$

To calculate $\boldsymbol{P}(\boldsymbol{r}_1)$ the expectation values $\langle\hat{d}_1\hat{c}_1\rangle$ have to be known. Their determination is outlined in the following subsection.

2.2.3 Equation of Motion

The temporal evolution of the microscopic polarizations $p_{12}(t) = \langle\hat{d}_1\hat{c}_2\rangle$ can be derived using the Heisenberg equation of motion [51]

$$i\hbar\frac{\partial}{\partial t}p_{12}(t) = \langle[\hat{p}_{12}, \hat{H}]\rangle. \qquad (2.40)$$

Evaluating the commutator on the right hand side of the equation, one finds a coupling to four-operator expectation values due to the many-body part of the Hamiltonian $\hat{H}_{\mathrm{many-body}}$. For example, the commutator

$$\langle[\hat{d}_1\hat{c}_2, \int d\boldsymbol{r}_1' \int d\boldsymbol{r}_2' \hat{c}_{1'}^+\hat{c}_{2'}^+\hat{c}_{2'}\hat{c}_{1'}]\rangle \qquad (2.41)$$

yields terms containing the expectation values

$$\int d\boldsymbol{r}_3 \langle\hat{c}_3^+\hat{d}_1\hat{c}_2\hat{c}_3\rangle. \qquad (2.42)$$

The four-point quantities couple again to six-point quantities and so forth [44]. As done in chapter 4, we apply the time-dependent Hartree-Fock approximation

to truncate this infinite hierarchy, i.e., we factorize the four-operator expectation values into products of two-operator expectation values according to the rule [44, 52]

$$\langle \hat{c}_3^+ \hat{d}_1 \hat{c}_2 \hat{c}_3 \rangle \approx \langle \hat{c}_3^+ \hat{c}_3 \rangle \langle \hat{d}_1 \hat{c}_2 \rangle - \langle \hat{c}_3^+ \hat{c}_2 \rangle \langle \hat{d}_1 \hat{c}_2 \rangle \,. \tag{2.43}$$

Then, the equation of motion for the interband coherence reads

$$
\begin{aligned}
i\hbar \frac{\partial}{\partial t} p_{12} &= \left[E_{\text{gap}} - \frac{\hbar^2}{2m_h}\nabla_1^2 - \frac{\hbar^2}{2m_e}\nabla_2^2 + \frac{e^2}{2}\delta V_{11} + \frac{e^2}{2}\delta V_{22} - e^2 V_{12}^C \right] p_{12} \\
&\quad - \int d\boldsymbol{r}_3\, e^2 (V_{13}^C - V_{32}^C)(n_{33}^{e,\,eq} - n_{33}^{h,\,eq})p_{12} \\
&\quad + \int d\boldsymbol{r}_3\, e^2 (V_{13}^C - V_{32}^C)(n_{32}^{e,\,eq} p_{13} - n_{31}^{h,\,eq} p_{32}) \\
&\quad - \boldsymbol{\mu}_{eh} \cdot (\boldsymbol{E}_1 \delta_{12} - \boldsymbol{E}_1 n_{12}^{e,\,eq} - \boldsymbol{E}_2 n_{21}^{h,\,eq}) \,.
\end{aligned}
\tag{2.44}
$$

In Eq. (2.44) the abbreviations p for the interband coherence and n^e and n^h for the electron and hole intraband coherence, respectively, are used:

$$
\begin{aligned}
p_{12} &= \langle \hat{d}_1 \hat{c}_2 \rangle \,, \tag{2.45} \\
n_{12}^e &= \langle \hat{c}_1^+ \hat{c}_2 \rangle \,, \text{ and} \tag{2.46} \\
n_{12}^h &= \langle \hat{d}_1^+ \hat{d}_2 \rangle \,. \tag{2.47}
\end{aligned}
$$

It can be seen that the self-energies δV appear as potentials in the homogeneous part of Eq. (2.44). The term $(-e^2 V^C)$ constitutes the Coulomb attraction between electron and holes and gives rise to excitonic signatures in the optical spectra. The superscript "eq." for the densities indicates that for future considerations the populations are not calculated dynamically but rather quasi-equilibrium densities are inserted instead, see subsection 2.3.2.

For vanishing densities, $n^{e/h,eq} = 0$, Eq. (2.44) reduces to the equation

$$
\begin{aligned}
i\hbar \frac{\partial}{\partial t} p_{12} &= \left[E_{\text{gap}} - \frac{\hbar^2}{2m_h}\nabla_1^2 - \frac{\hbar^2}{2m_e}\nabla_2^2 + \frac{e^2}{2}\delta V_{11} + \frac{e^2}{2}\delta V_{22} - e^2 V_{12}^C \right] p_{12} \\
&\quad - \boldsymbol{\mu}_{eh} \cdot \boldsymbol{E}_1 \delta_{12}
\end{aligned}
$$
$$\tag{2.48}$$

which describes the polarization of the semiconductor in the linear regime when exciting the system from the ground state by a weak optical pulse. Note, that in the numerical calculations Eq. (2.48) and Eq. (2.44) are supplemented by a phenomenological dephasing rate γ.

2.3 Numerical Results

The combined semiconductor photonic-crystal system considered here consists of a periodic array of quantum wires located close to a two-dimensional photonic crystal. As already mentioned, it is possible to apply the theory in section 2.2 also to a quantum well, but then the numerical effort of solving Eq. (2.44) would be very demanding. Since the generalized Coulomb potential V^C explicitly depends on both positions of the two particles involved and not only on their relative distance, the commonly used transformation to relative and center-of-mass coordinates, where only the relative coordinate has to be resolved with high accuracy, is not reasonable. Thus, treating each coordinate at an exact level results in huge numerical complexity for an inhomogeneous system.

When reducing Eq. (2.44) to the ideal one-dimensional case, the exciton binding energy diverges due to the Coulomb potential V_0. To avoid this, a regularization parameter a_0 is introduced, i.e., $V_0 = 1/(4\pi\epsilon_r\epsilon_0(\mathbf{r} - \mathbf{r}' + a_0))$ is used instead. It has been shown that applying this potential for a wire with finite thickness yields excitonic resonances very close to those obtained from a full three-dimensional calculation if the radius of the wires is smaller than the exciton Bohr radius [44, 53]. In the following the parameter a_0 is chosen such that the exciton binding energy of the quantum wire resembles that of an ideal quantum well.

2.3.1 Linear Spectra

As starting point for the analysis linear absorption spectra are calculated, i.e., the field equations (2.5)-(2.6) are solved together with the material equation (2.48) using the parameters of Tab. D.2. Interesting features arise when the radius R of the air cylinders of the photonic crystal is altered, see Fig. 2.10(a)-(e).

For $R = 0$ the air holes are completely eliminated and the wires are surrounded by a homogeneous dielectric. Since the dielectric constant of the photonic crystal and the semiconductor material are chosen to be identical one expects to find the ordinary 1d-absorption spectra for this case [44]. As usual, for the used material parameters a strong 1s-exciton peak occurs at about 1.482 eV and the onset of the continuum starts at about 1.500 eV, see Fig. 2.10(e). The difference of these two values determines the exciton binding energy which is 18 meV, i.e., approximately four times the three-dimensional exciton binding energy[7].

If the radius is set to $R \to \infty$ the dielectric material in between the air cylinders is removed which corresponds to a situation where the quantum wires are located at the distance D from a planar interface. Again the absorption spectrum

---

[7]The binding energy in bulk GaAs is about $E_B^{\text{bulk}} = 4.2\,\text{meV}$; for an ideal quantum well (which shall be reproduced with the wire) one finds $E_B^{\text{QW}} = 4E_B^{\text{bulk}}$.
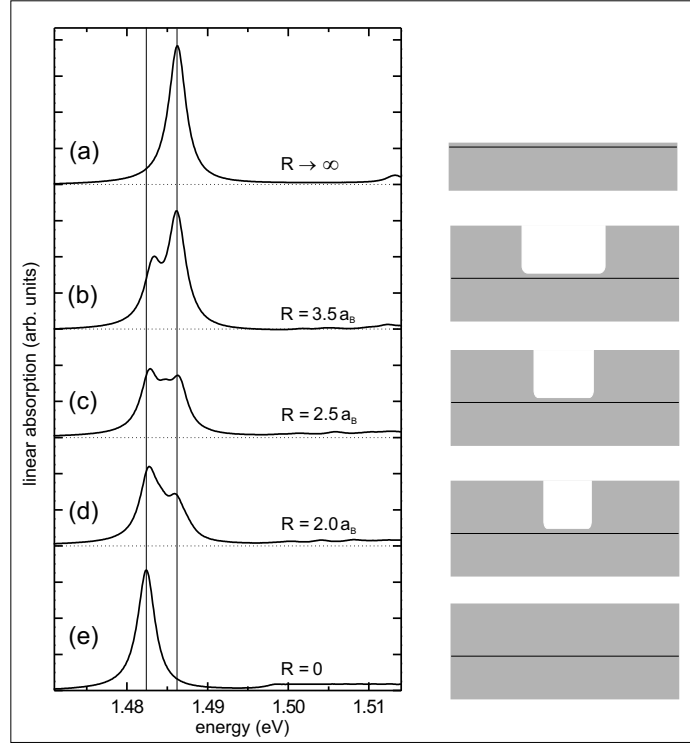
Figure 2.10: Calculated linear absorption spectra which depend on the radius of the air cylinders regarding the structure Fig. 2.1. $R = 0$ corresponds to a situation where the quantum wire array is surrounded by a homogeneous dielectric and $R \to \infty$ signifies the limiting case of a planar interface. The unit cell width was set to $d = 9.6a_B$ where $a_B = 13$ nm is the Bohr radius of a three-dimensional GaAs exciton. The right pictures show the proportion of dielectric (gray) to air and are drawn to scale. After Ref. [35].

shows an 1s-exciton resonance and the onset of the continuum, cp. Fig. 2.10(a), but both values are shifted towards higher energies compared to the case for $R = 0$. This is a consequence of the self energies δV that appear in Eq. (2.48) and lead to an increase of the energies of electrons and holes. Furthermore, the shift of the continuum absorption of about 16 meV is much bigger than the shift of the exciton resonance of about 4 meV yielding a larger exciton binding energy for the $R \to \infty$ case. An intuitive reason for the behavior of the binding energy is that the additional contributions to the common Coulomb are roughly proportional to $1/D$, cp. Eq. (2.31). When the semiconductor is close to air which has a lower dielectric constant compared to the material leading to the same sign for V_0 and δV this results in an enhanced electron-hole attraction and therefore in a larger exciton binding energy.

In the presence of the photonic crystal both scenarios compete with each other. There are charge carriers near the material-air interface underneath the air cylinders as well as underneath dielectric material which leads to a "mixture" of the effects in Fig. 2.10(a) and Fig. 2.10(e) depending on the actual radius of the cylinders. If $R = 0$ is increased to $R = 2.0a_B$, Fig. 2.10(d), the energetically lower peak becomes smaller in amplitude and the higher peak starts to show up. For $R = 2.5a_B$, Fig. 2.10(c), both signatures are roughly equally pronounced. This behavior continues until the situation of the planar interface is reached.
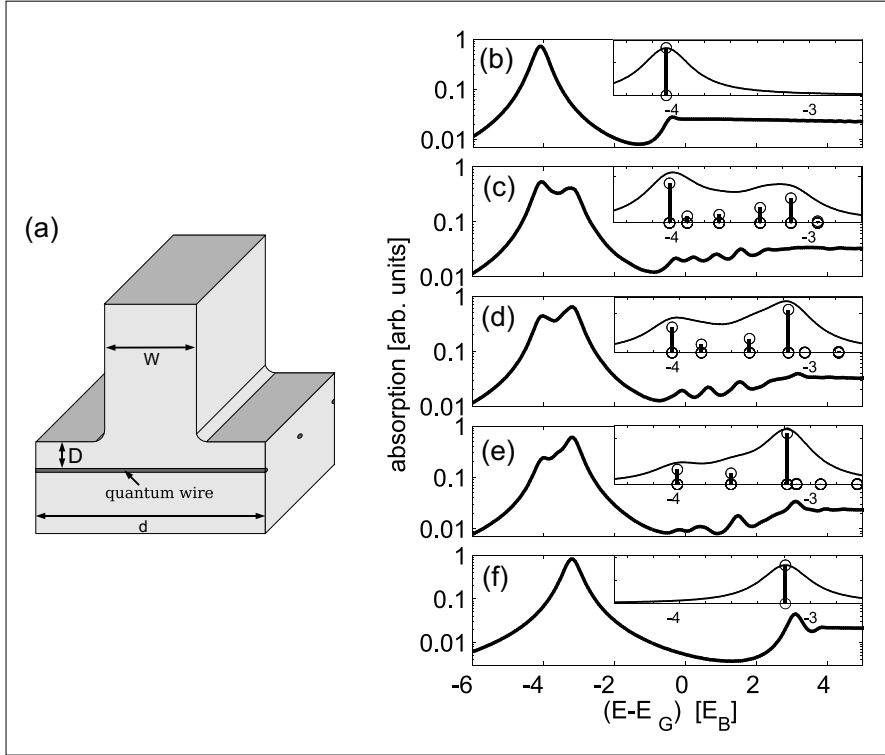
Figure 2.11: (a) Drawing of a unit cell of a rib-like photonic-crystal structure which is used because of the reduced numerical effort. Analog to the air-cylinder setup, D denotes the distance of the wires from the air interface and d the length of the unit cell. W is the width of slab. The parameters are $D = 0.2a_B$ and $d = 13.8a_B$. (b)-(f) Linear absorption spectra for different widths of the slab. W was set to $W = d$, $W = 2/3d$, $W = 1/2d$, $W = 1/3d$, and $W = 0$, respectively (from top to bottom). The insets show the contributing excitonic resonances to the absorption. Note, that the spectra are plotted on a logarithmic scale whereas the decomposition into resonances is displayed on a linear scale. Taken from Ref. [54].

A more detailed understanding of the interplay of the resonances in a similar

structure has been developed by Pasenow *et al.* in Ref. [54]. Therein, a rib-like arrangement of alternating dielectric materials has been investigated. One unit cell of the photonic crystal is shown in Fig. 2.11(a). An advantage of using such a setup is that one only needs a large number of grid points along the direction of the quantum wire whereas the distance between the wires can be kept small to simulate these system. In a sense, the numerical effort in a rib structure scales like $\mathcal{O}(d)$ when increasing the unit-cell length to analyze the $W \leftrightarrow d$ dependence[8]. This is not the case for the unit cell containing the air cylinder which has a $\mathcal{O}(d^2)$ complexity. However, since the principle effects, namely the transversal field propagation and the longitudinal Coulomb modification exist in both structures, analog features are to be expected in either case.

Fig. 2.11(b)-(f) display linear absorption spectra for various widths W of the ribs. Again, the common quantum wire result is recovered for $W = d$ corresponding to a homogeneous dielectric and a spectrum with one exciton but higher binding energy is obtained for $W = 0$ corresponding to an array of wires close to a planar interface. Furthermore, the typical double peak occurs for $0 < W < d$ and reveals the same behavior as in the case for the air cylinders when varying R. Note, that the order from the homogeneous-like to the half-space-like scenarios are reversed in Fig. 2.11(b)-(f) compared to Fig. 2.10(a)-(e).

More detailed information on all relevant exciton resonances is shown in the insets of Fig. 2.11. The bars display the energetic position of the resonances as well as the corresponding oscillator strengths. To get the excitonic states, the polarization equation Eq. (2.48) has been diagonalized[9]. The different widths of the slab enter via the self energies δV_{ii}. As expected, for the homogeneous and the half-space cases only a single exciton resonance contributes to the spectrum. However, for $0 < W < d$ a number of states participate in the absorption process as shown in the insets of Fig. 2.11(c)-(e). Nevertheless, for all considered widths W of the ribs the homogeneous and half-space excitons yield the most important contributions to the absorption which also sustains the interpretation of the double peak feature in case of the photonic crystal consisting of air cylinders discussed above.

The detailed knowledge of the distribution of the exciton resonances is not essentially required to study the optical gain of photonic crystal structures as done in subsection 2.3.3. However, it is possible to exploit the findings for different effects. For example, it has been demonstrated in Ref. [54] that one can excite a

---

[8]More precisely: The analysis of the dependence of the linear spectra on the ratio of material to air when enlarging the whole structure (not shown).

[9]Diagonalization yields the exciton eigenenergies $\epsilon_{X,i}$ and for convenience the respective oscillator strengths A_i are determined by fitting the absorption spectra by a sum of Lorentzian curves $\sum_i A_i/((E - \epsilon_{X,i})^2 - \gamma^2)$ to account for the space-dependent light-matter coupling. Here, γ is the dephasing constant also used in Eq. (2.48).

single or multiple excitonic states which are associated with their particular wave functions by using a properly tuned spectrally-narrow laser pulse. Then, the generated carrier density is distributed according to these eigenfunctions in the coherent limit revealing a complicated dynamics of the created wave packets. As long as the dephasing processes are not decisive a time-dependent spacial patterning of the electron and hole densities can be achieved in this way [54]. If, however, the coherent regime is left the populations will relax towards quasi-equilibrium densities whose properties are presented in the next subsection for the crystal structure made up of air cylinders.

2.3.2 Quasi-Equilibrium Densities

The results discussed previously are obtained by solving the material equation Eq. (2.48) for weak excitation in the linear regime. Another aim is to calculate the microscopic polarization in the presence of quasi-equilibrium electron and hole distributions by using Eq. (2.44). In the following it is described how these densities are determined in real space.

As can be seen from Eq. (2.36), both the electrons and holes move in an additional potential δV which due to the photonic crystal varies periodically in space. That is why the electron and hole wave functions can be written according to the Bloch theorem [26] as

$$
\Psi_{\lambda,\mathbf{k}}^{e/h}(\mathbf{r}) = \frac{e^{i\mathbf{k}\cdot\mathbf{r}}}{L^{d'/2}} u_{\lambda,\mathbf{k}}^{e/h}(\mathbf{r}) \, , \tag{2.49}
$$

where $u_{\lambda,\mathbf{k}}^{e/h}(\boldsymbol{r})$ is the periodic Bloch function, λ the band index, $\boldsymbol{k}$ the wave vector, d' the dimensionality of the system, and L its length. Inserting the ansatz Eq. (2.49) into the Schrödinger equation yields eigenvalue equations for electrons

$$
\left[-\frac{\hbar^2}{2m_e}\Delta - i\frac{\hbar^2}{m_e}\boldsymbol{k}\cdot\nabla + \frac{\hbar^2 k^2}{2m_e} + E_{\text{gap}} + \frac{e^2}{2}\delta V(\boldsymbol{r},\boldsymbol{r}) \right] u_{\lambda,\mathbf{k}}^e(\boldsymbol{r}) = \epsilon_{\lambda,\mathbf{k}}^e u_{\lambda,\mathbf{k}}^e(\boldsymbol{r})
$$
$$\tag{2.50}$$

and for holes

$$
\left[-\frac{\hbar^2}{2m_h}\Delta - i\frac{\hbar^2}{m_h}\boldsymbol{k}\cdot\nabla + \frac{\hbar^2 k^2}{2m_h} + \frac{e^2}{2}\delta V(\boldsymbol{r},\boldsymbol{r}) \right] u_{\lambda,\mathbf{k}}^h(\boldsymbol{r}) = \epsilon_{\lambda,\mathbf{k}}^h u_{\lambda,\mathbf{k}}^h(\boldsymbol{r})
$$
$$\tag{2.51}$$

which basically differ in the masses of the quasi particles. Eqs. (2.50) and (2.51) are now diagonalized numerically in order to get the eigenvalues $\epsilon_{\lambda,\mathbf{k}}^{e/h}$ and the eigenfunctions $u_{\lambda,\mathbf{k}}^{e/h}(\boldsymbol{r})$.
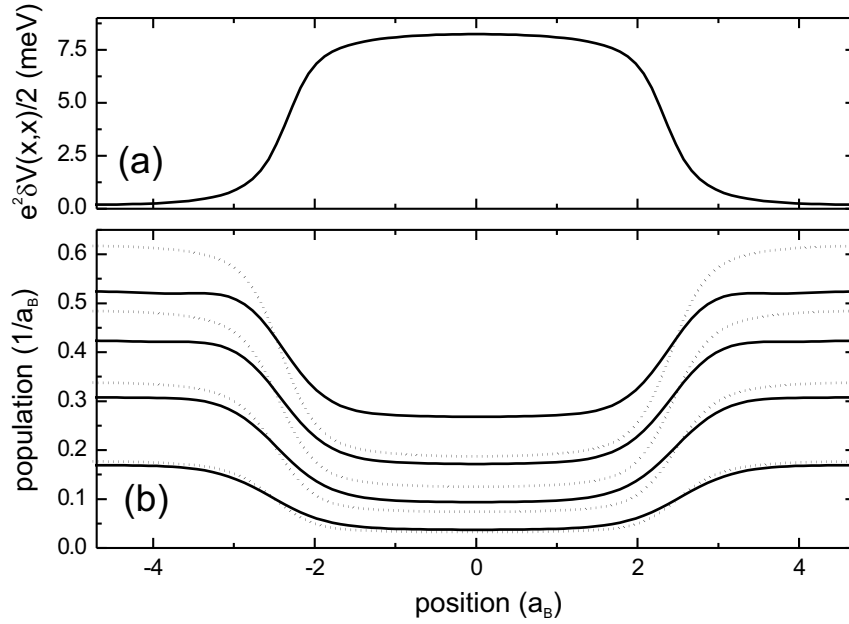
Figure 2.12:   Examination of a structure with a unit cell width of $d = 9.6a_B$ and an air cylinder radius of $R = 2.65a_B$ showing (a) the single-particle potential $(e^2/2)\delta V(x, x)$, which enters Eq. (2.50) and Eq. (2.51), and (b) the corresponding space-dependent electron and hole quasi-equilibrium densities. The total carrier densities are $n_{\text{total}}^{e/h} \in \{0.1/a_B,\ 0.2/a_B,\ 0.3/a_B,\ 0.4/a_B\}$ (from bottom to top), the temperature is set to $T = 50$ K, and the electron (hole) distributions are displayed as solid (dotted) lines. Note that the zero of the x-axis coincides with the center of the cylinder. Taken from Ref. [35].

Assuming quasi-equilibrium within each band, the particles are distributed according to the Fermi function

$$n_{\lambda,\mathbf{k}}^{e/h} = \frac{1}{e^{\beta(\epsilon_{\lambda,\mathbf{k}}^{e/h} - \mu^{e/h})} + 1}\,, \tag{2.52}$$

where $\beta = 1/(k_B T)$ is the inverse temperature and $\mu^{e/h}$ the chemical potential.

Hence, for a given total density n_{total} and fixed temperature T it is possible to determine the chemical potential since it holds that

$$n_{\text{total}}^{e/h} = \sum_{\lambda,\mathbf{k}} n_{\lambda,\mathbf{k}}^{e/h}\,. \tag{2.53}$$

Inserting $\mu^{e/h}$ into Eq. (2.52), the particle distributions are known in $\mathbf{k}$-space. Transforming to real space coordinates yields the space-dependent quasi-

equilibrium electron and hole populations n_{12}^e and n_{12}^h, respectively,

$$n_{12}^{e/h,eq} = \frac{1}{L^{d'}} \sum_{\lambda,\mathbf{k}} u_{\lambda,\mathbf{k}}^{e/h*}(\boldsymbol{r_1}) u_{\lambda,\mathbf{k}}^{e/h}(\boldsymbol{r_2}) \frac{1}{e^{\beta(\epsilon_{\lambda,\mathbf{k}}^{e/h} - \mu^{e/h})} + 1} \; . \tag{2.54}$$

Fig. 2.12(b) shows several carrier distributions for a fixed temperature of $T = 50$ K where the total density is chosen in the range from $n_{\text{total}} = 0.1/a_B$ to $n_{\text{total}} = 0.4/a_B$. Since the thermal energy of $k_B T = 4.3$ meV is smaller than the spatial variation of the additional potential δV, the particles predominantly arrange according to the self energy which is displayed in Fig. 2.12(a). It can be clearly seen that the carriers accumulate in the regions in between the cylinders, i.e., they avoid the regions of high single-particle potential. The effect is more pronounced for holes than for electrons since they have a larger effective mass.

2.3.3   Density-Dependent Spectra

The linear spectra examined in subsection 2.3.1 alter appreciably in the presence of electron and hole densities. The carriers are spatially distributed as described in subsection 2.3.2 for various total densities and fixed temperature. First, the photonic crystal is removed and replaced by a homogeneous medium to study the density-dependent effects alone. The results are shown in Fig. 2.13. For $n_{\text{total}} = 0$ the linear absorption spectrum Fig. 2.10(e) is recovered, i.e., the spectrum is basically dominated by the 1s-exciton peak at 1.482 eV. Increasing the carrier densities in the range $0 < n_{\text{total}} < 0.3/a_B$ the peak height diminishes. The bleaching is due to the electron and hole densities $n_{12}^{e/h,eq}$ which are now present in Eq. (2.44) wherein the term $\left(\boldsymbol{E}_1 \delta_{12} - \boldsymbol{E}_1 n_{12}^{e,eq} - \boldsymbol{E}_2 n_{21}^{h,eq} \right)$ leads to a reduced absorption of light. When the density is increased even further the absorption of the exciton resonance vanishes and becomes negative for large n_{total} meaning that optical gain is achieved. In the latter case the semiconductor is so highly excited that the incoming light field is amplified. The shift of the resonances is due to band gap renormalization and is of minor importance for the actual analysis.

In Fig. 2.14 the density-dependent spectra for the entire material system, i.e., a quantum wire embedded in a photonic crystal structure, are displayed. The radius of the air cylinders is set to $R = 2.65 a_B$ so that the typical double peak absorption occurs for $n_{\text{total}} = 0$. Qualitatively, both resonances behave like the one in the homogeneous system and their height is reduced for increasing total density. However, the bleaching of the energetically lower peak is much more pronounced than that of the higher peak. At a certain density the lower resonance already shows gain whereas the higher one is still absorbing. The situation becomes transparent by recognizing that due to the photonic crystal the quasi-equilibrium electron and hole densities are spatially inhomogeneously distributed, see subsection 2.3.2.
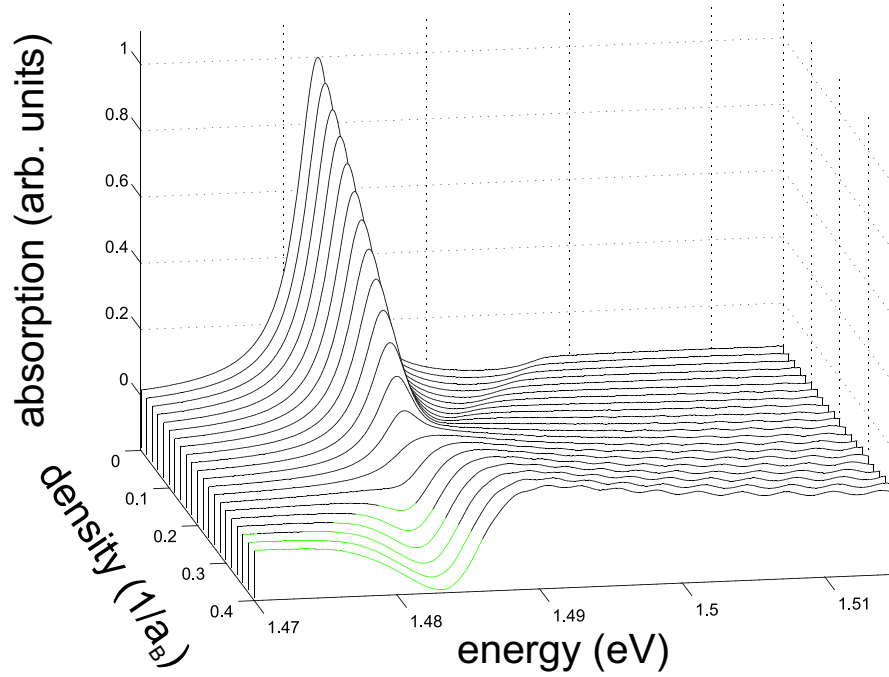
Figure 2.13: Dependence of the absorption/gain spectra on the total carrier density n_{total} for an array of quantum wires which is homogeneously surrounded by dielectric material. Gain (highlighted) occurs for densities $n_{\text{total}} \geq 0.3/a_B$. Taken from Ref. [35].

According to Fig. 2.12(b) more carriers can be found in between the air cylinders than beneath the cylinders. That is way the lower peak which is associated with the former positions reacts more sensitively to a change of the total density.

The most striking effect of the inhomogeneous dielectric environment can be observed by comparing Fig. 2.13 and Fig. 2.14. Whereas optical gain in the homogeneous structure occurs at a total density of about $n_{\text{total}} = 0.3/a_B$ the use of the photonic crystal reduces the gain threshold to about $n_{\text{total}} = 0.24/a_B$. Furthermore, the absolute gain-peak height is enhanced in the inhomogeneous case if spectra for the same n_{total} are considered.

The structure can, in principle[10], be optimized to increase the gain even further. Since the charge carriers prefer to accumulate in the space regions below the dielectric it would be desirable to design the system in such a way that also the electric field has its strongest contributions at these positions. The unit cell with a width of $d = 9.6a_B$ which has been used in the previous calculations is shown

---

[10]The simulations are limited by the computer power: On a current Pentium4 (3GHz) machine the calculation of a spectrum for the $d = 9.6a_B$ unit cell takes more than one day and for the $d = 24.2a_B$ unit cell more than one week, respectively.
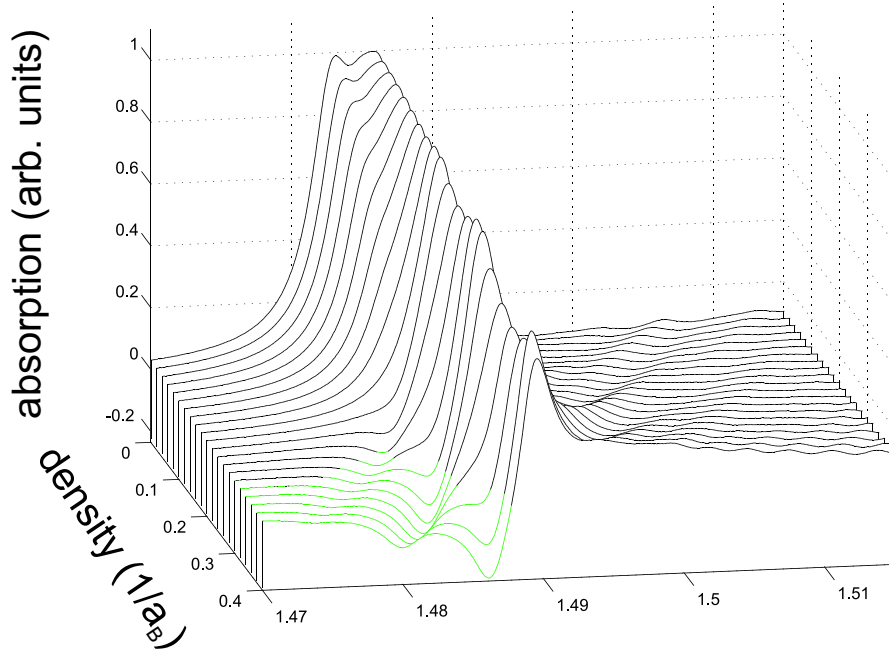
Figure 2.14: Analogous to Fig. 2.13 the dependence of the absorption/gain spectra on the total carrier density n_{total} is shown but for an inhomogeneous structure, i.e., the array of quantum wires is located close to a photonic crystal. Gain (highlighted) is already present for the lower peak for $n_{\text{total}} \geq 0.24/a_B$. Taken from Ref. [35].

in Fig. 2.15(a). Below, additionally the single-particle potential and the absolute value of the time integrated electric field

$$T(\boldsymbol{r}) = \int_{-\infty}^{\infty} dt \, |\boldsymbol{E}(\boldsymbol{r}, t)| \tag{2.55}$$

are plotted. Note, that in the simulations the active material was removed and $T(\boldsymbol{r})$ was solely recorded at the position of the quantum wire. Since the exciting pulse was again chosen to be ultrashort and therefore has a broad spectrum, the time-integrated field is only a rough estimate for the decisive part of the light-matter interaction. Nevertheless, it can be seen that $T(\boldsymbol{r})$ has high values below the cylinders, i.e., at those positions which are avoided by the electrons and holes, and low values underneath the dielectric. Although the curve shows this space-dependence it should be mentioned that it is displayed in arbitrary units. If the absolute value of maximum and minimum are compared one only finds a deviation of about 14% which means that the field is rather homogeneously distributed.

The situation changes if the structure in Fig. 2.15(b) having a unit-cell width of $d = 24.2a_B$ is examined. Though, again the single-particle potential is large
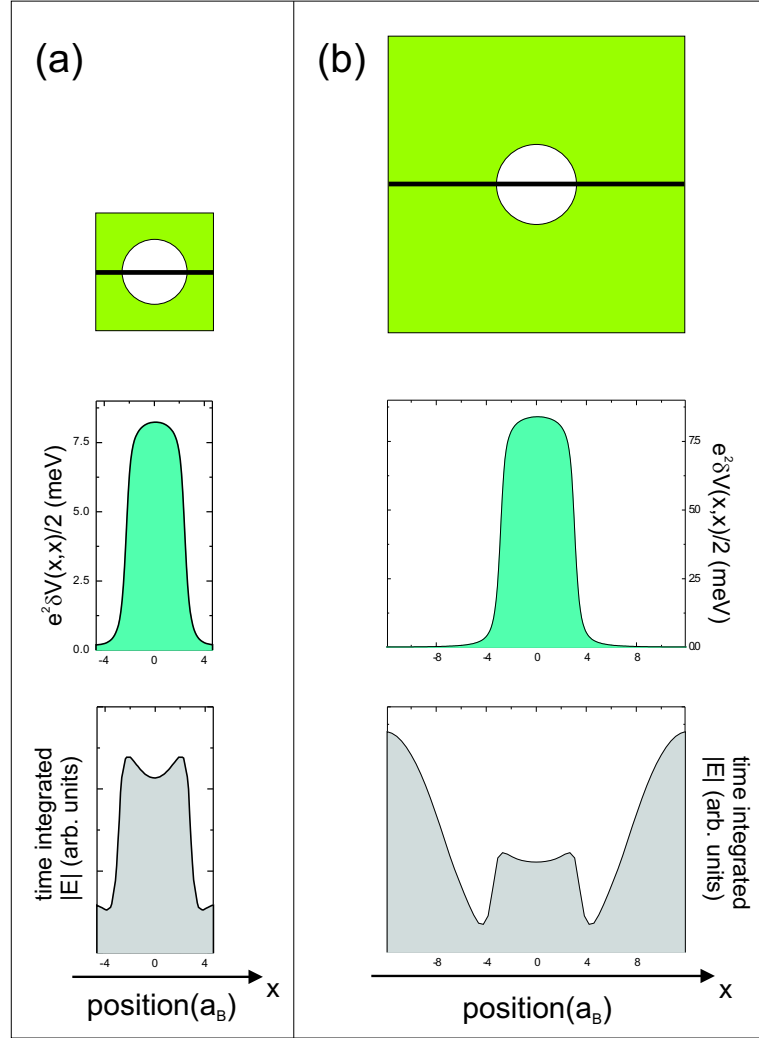
Figure 2.15: For two different unit cells with a width and radius of (a) $d = 9.6a_B$ and $r = 2.65a_B$ and (b) $d = 24.2a_B$ and $r = 3.26a_B$ the structure from the top, the single-particle potential $(e^2/2)\delta V(x,x)$, and the time-integrated absolute value of the electric field, Eq. (2.55), is shown. The potential and the field are recorded at the position (indicated by the black line in the upper row) of the quantum wire which is absent in the simulation. Structure (a) has been used for the calculations in Fig. 2.12-2.14. Note, that each x-axis is drawn to scale.

under the air cylinder, the quantity $T(\boldsymbol{r})$ exhibits its maxima at positions at which the carriers primarily accumulate, namely below the dielectric material. Moreover, the ratio between the maximum and the minimum of the time-integrated signal is approximately 32%. Hence, one would expect an enhanced light-matter

interaction compared to the smaller structure.

Figure 2.16: Comparing the optical response for two different unit cells: In each figure the results of structure Fig. 2.15(a) are displayed as thick solid line and of structure Fig. 2.15(b) as dotted line, respectively. In (a) the normalized linear absorption is shown for a homogeneous case of a planar interface where the original curve of the large structure (thin solid line) is mul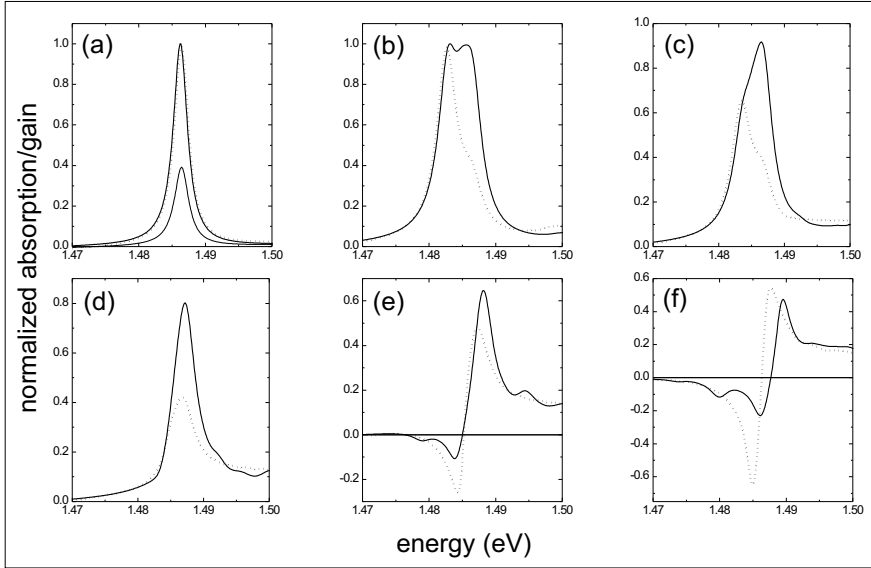tiplied by a geometric factor for better comparison. The absorption/gain for the particular photonic crystal structure for electron and hole quasi-equilibrium densities of $n_{\text{total}}^{e/h} \in \{0, 0.1/a_B, 0.2/a_B, 0.3/a_B, 0.4/a_B\}$ is displayed in the figures (b)-(f) (n_{total} increasing from (b) to (f)).

To study the whole hybrid system, again the quantum wire is included in the following. First, for a comparison between the "small" (**S**) and the "large" (**L**) unit cell the absorption spectra are calculated for the case of a planar interface. It can be observed in Fig. 2.16(a) that the absorption is much weaker for the **L** structure (thin solid line) than for the **S** structure (thick solid line). This is not surprising since the ratio of active to passive material is smaller in the former case. If the **L**-absorption is multiplied with a factor accounting for the geometric discrepancy, basically the same curve is recovered, see dotted line. Therefore, for the analysis of the spectra resulting from the inhomogeneous structuring displayed in Fig. 2.16(b)-(f) this very factor has been included.

In Fig. 2.16(b) the linear absorption spectra for both cases are shown in the presence of the photonic crystal. Every curve exhibits the double-peak characteristic, however, the upper peak is less pronounced for the **L** structure (dotted). This

is due the fact that fraction of dielectric to air is increased, cp. Fig. 2.15(a) and (b), which favors the lower resonance. With increasing density the lower peak is stronger bleached ((c)-(d)) and also yields a larger absolute value when the gain regime is reached ((e)-(f)). This means that the large unit cell in which the charge carriers as well as the electric field prefer to stay at similar positions is relatively more sensitive to a change of the total density than the smaller one.

The above effects could be even more intense if the overlap between the electromagnetic field and the charge carriers is further increased. For future studies one could think of explicitly exploiting the photonic crystal band structure by propagating the pulse in a direction parallel to the air cylinder lattice. Introducing defects into the crystal would allow to concentrate the light into certain regions of space which could be filled with active material. For example, in Ref. [55] a strongly coupled system in which a single quantum dot is embedded in a photonic crystal nanocavity is experimentally investigated. However, since in such a situation any symmetry is broken and no periodic boundary conditions can be applied, one would have to compute the *whole* structure in a three-dimensional simulation space. Nowadays, even the computation of pure photonic crystal properties (without any active material) by means of the 3D-FDTD code usually requires the computational power of large computer clusters. Hence, a challenging numerical problem is to be addressed.

Chapter 3

Intermezzo: Planar Chiral Nanostructures

"The pure and simple truth is rarely pure and never simple."
- Oscar Wilde

In the previous chapter, a theory to self-consistently describe a photonic crystal including semiconductor material with optical resonances has been developed. Certainly, applying this algorithm it is also possible to examine pure passive materials, i.e., structures that consist of different regions with fixed dielectric constant. In this category, e.g., planar chiral structures (PCS) can be found. They have become the subject of intense experimental and theoretical investigations quite recently [56–60]. Rather than looking at a single chiral element, PCS are mostly studied in a periodic arrangement, i.e., in a sense the structures may also be considered as a two-dimensional photonic crystal. In the following, a detailed analysis of light interaction with PCS is presented.
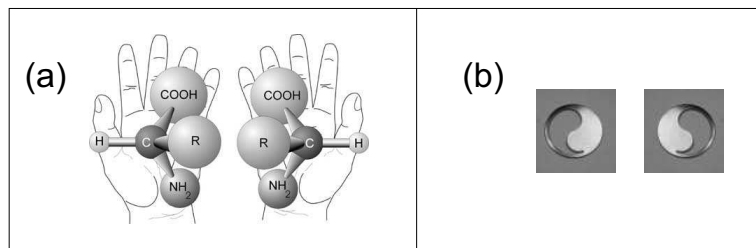

Figure 3.1: (a) The hands and the shown molecules are chiral in a three-dimensional sense. There exists no rotation or displacement which brings the enantiomers into congruence. (b) The ying-yang symbol is an example of a two-dimensional chiral object.

The original definition of chirality[1] is given for three-dimensional objects. Such objects are not superimposable on their mirror image regardless of how they are rotated. From this it follows that in three dimensions every item which possesses a plane of symmetry or a center of symmetry is achiral. Typical chiral objects are shown in Fig. 3.1(a). For example, it is well known that humans have one left and one right hand. Both hands cannot be brought into congruence with one another, however, they are, in general, their respective mirror images. These two forms are called enantiomers[2]. It is worth mentioning that chirality is not only a geometric peculiarity but manifests itself, e.g., in the physical and chemical properties of molecules [61]. Below it is analyzed how a *planar* chiral structure - more precisely, the different shape of the two enantiomers - influences the interaction of light with the material.

A two-dimensional chiral object can be seen in Fig. 3.1(b). Note, that this symbol is achiral in the common sense, since in three dimensions it would be possible to rotate it around an appropriate axis with angle π to obtain its mirror image. That is why the definition of chirality within the plane is somewhat relaxed: A planar structure is said to be chiral if it cannot be brought into congruence with its mirror image unless it is lifted from that plane.
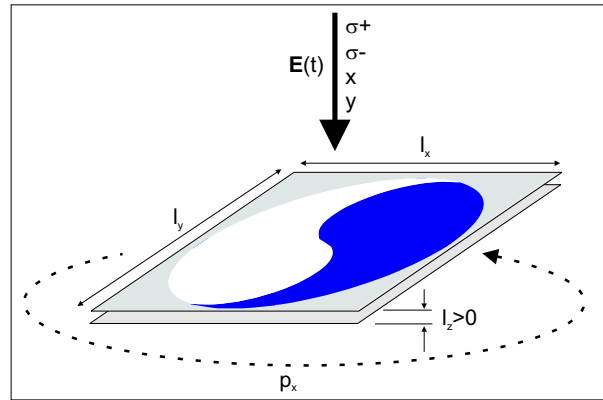
Figure 3.2: Simulation space (shown is one unit cell) for the PCS: A plane wave with defined polarization is normally incident onto an infinite two-dimensional array of planar chiral structures. Note, that the planarity is due to the different lengths $l_z \ll l_x = l_y$.

In the following analysis, the question is addressed to which extent the symmetry of the light-matter interaction can result from the planar chiral patterning alone. In doing so, the inner properties of the material are neglected and the different media which constitute the chiral object are described via a space-dependent

---

[1]The word chirality is derived from the Greek $\chi\epsilon\iota\rho$ (cheir) meaning "hand".
[2]The Greek $\epsilon\nu\alpha\nu\tau\iota\omega\zeta$ (enantios) means "opposite".

dielectric constant $\epsilon(\boldsymbol{r})$. The principle setup is depicted in Fig. 3.2. We consider an array of gammadions[3] which may be regarded as planar since the extension of the slab in z-direction l_z is much smaller than the width of the unit-cell $l_x = l_y$. During the numerical simulation only one unit-cell is computed and an infinite array is established by using periodic boundary conditions p_x and p_y in the x-y-plane. The light-matter interaction can be analyzed in detail by radiating a plane wave traveling in z-direction onto the structure which is either linearly or circularly polarized. Then, the reflected light is examined in the nearfield of the PCS.

To conveniently describe the properties of an object and its symmetry in technical terms the functions f and $f_\mathcal{R}$ as well as the operators $\mathcal{D}$ and $\mathcal{M}$ are introduced. Here, $f = f(\boldsymbol{r})$ denotes the patterning of a chiral structure and $f_\mathcal{R} = f_\mathcal{R}(\boldsymbol{r})$ refers to its enantiomeric form. The operation $\mathcal{D} = \mathcal{D}_\phi$ rotates the object ϕ counterclockwise and $\mathcal{M}$ mirrors it at a line in the plane[4]. For example, because of the four-fold rotational symmetry of a gammadion it holds that $f(\boldsymbol{r}) = f(\mathcal{D}_{n\pi/2}\boldsymbol{r})$ for all integers n. Also, it is true that $f(\mathcal{M}\boldsymbol{r}) = f_\mathcal{R}(\boldsymbol{r})$ if one chooses, e.g., the line $x = 0$ as axis of reflection ($x = y = 0$ being the center of the unit cell).

3.1 Numerical Results

The numerical simulations are based on Maxwell's equations for pure dielectric materials Eqs. (2.7)-(2.8) and are performed using the FDTD-method described in section 2.1. Fig. 3.3(a) shows the array of gammadions denoted as **L** from the top where the dark areas correspond to vacuum ($\epsilon(\boldsymbol{r}) = 1$) and the bright areas to material ($\epsilon(\boldsymbol{r}) > 1$). The dimension of a unit cell is on the order of the wavelength of the exciting light field. All numerical parameters are given in App. D.3-D.4. Besides the structure **L** also its enantiomeric form **R** has been plotted in Fig. 3.3(c). The question is how the PCS interact with light being polarized in different ways.

To answer this, the flow map (FM) during a propagation simulation is recorded, i.e., the total Poynting vector $\boldsymbol{S} = \boldsymbol{E} \times \boldsymbol{H}$ for the reflected light is calculated and projected onto the incident light propagation direction $\boldsymbol{n}_z$. The plane at which the FMs are determined is located in the near field of the reflected waves. The signal is collected over all times so that the quantity

$$FM(\boldsymbol{r}) = \int_{-\infty}^{\infty} dt \, \boldsymbol{n}_z \cdot \boldsymbol{S}(\boldsymbol{r}, t) \tag{3.1}$$

---

[3]A gammadion is a star-like structure which consists of (in the present case four) arms resembling the Greek capital letter Γ.

[4]Throughout the discussion the object is centered in the unit cell. That is why implicitly the rotation around the center and the mirroring along a line through the center is assumed.
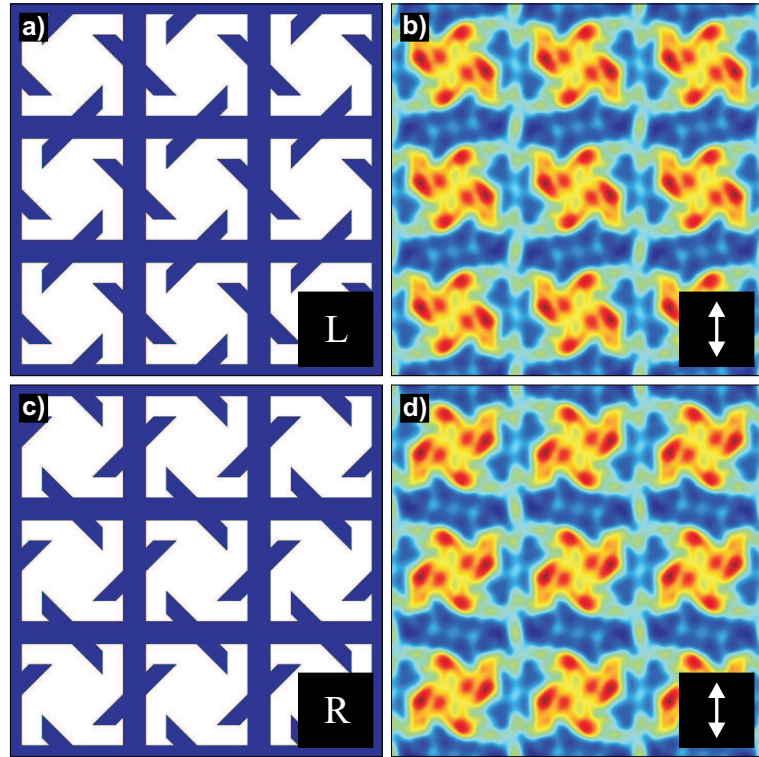
Figure 3.3: (a) An array of gammadions seen from the top and (b) the corresponding FM when exciting the PCS with linearly polarized light as indicated by the arrow. The equivalent pictures for the enantiomeric form are depicted in Figs. (c) and (d) . Taken from Ref. [62].

is used for comparison. Fig. 3.3(b) displays the FM which is obtained when illuminating the structure **L** with *linearly* polarized light as indicated by the arrow. Low intensity is coded with blue color changing over yellow to red which stands for higher intensities. Analog Fig. 3.3(d) shows the flow map of the enantiomer **R**. Not surprisingly, the FMs are also enantiomers of each other, i.e., Fig. 3.3(b) is the mirror image of Fig. 3.3(d). Note, however, that the originally existing four fold rotational symmetry of the gammadion is lost and that the intensities exhibit merely a two fold symmetry.

The situation is quite different if the structures are excited with *circularly* polarized light as can be seen in Fig. 3.4. If one illuminates the arrays **L** and **R** with, e.g., left circularly polarized light the observed FM are no mirror images of each other, see Fig. 3.4(a) and Fig. 3.4(c). Also, for right circularly polarized excitation the enantiomeric symmetry is broken. However, the mirror symmetry is conserved when comparing the FMs in such a way that besides the opposite
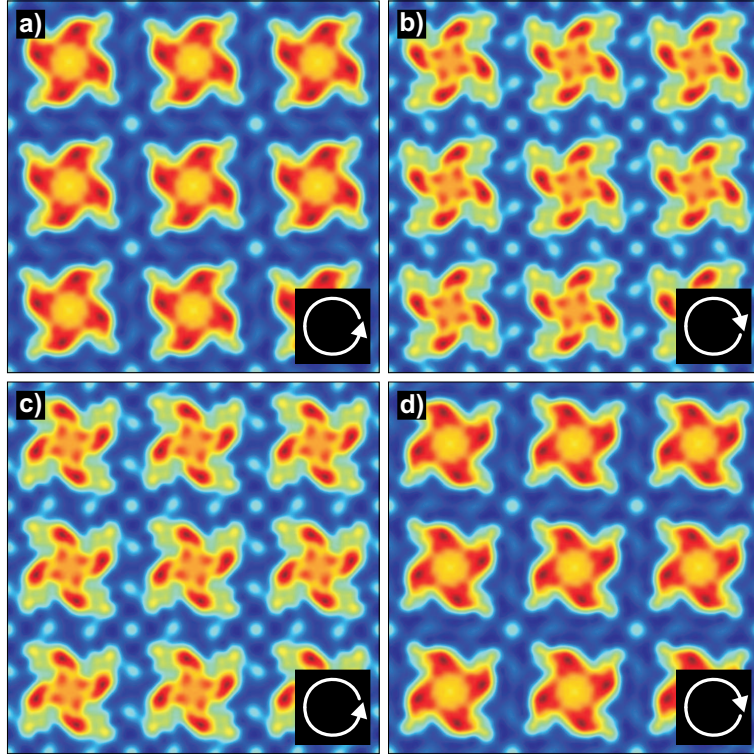
Figure 3.4: The FM of the PCS **L** (upper row) and **R** (lower row) if the enantiomers are excited with linearly polarized light as indicated by the arrows. Taken from Ref. [62].

chirality of the structure also the opposite light polarization is used. This can be seen by regarding Fig. 3.4(a) versus Fig. 3.4(d) and Fig. 3.4(b) versus Fig. 3.4(c), respectively. Note, that for all cases the four fold rotational symmetry is kept.

To analyze these phenomena beyond the model of purely dielectric material we also simulated unit cells consisting of a thin gold film in which one gammadion has been cut. Therefore, we applied the finite-element frequency-domain (FEM)[5] method and solved Maxwell's equations in the frequency domain along with the constitutive relation $\boldsymbol{D}(\boldsymbol{r}, \omega) = \epsilon(\boldsymbol{r}, \omega)\boldsymbol{E}(\boldsymbol{r}, \omega)$. To allow for losses in the material the gold was modeled with a *complex* dielectric constant $\epsilon(\boldsymbol{r}, \omega = \omega_0)$ at fixed frequency ω_0 whereas the vacuum was treated with $\epsilon \equiv 1$. The results of the simulations are shown in Fig. 3.5(a)-(d). Again, the broken enantiomeric symmetry is observed ((a), (c) and (b), (d)) and the mirror image of the original FM is obtained if both the handedness of the incident light field and the twist[6] of the medium is

---

[5]All FEM-calculations were carried out by A.V. Krasavin *et al.* from the University of Southampton.

[6]Here, reversing the twist of the material simply means using the enantiomer.
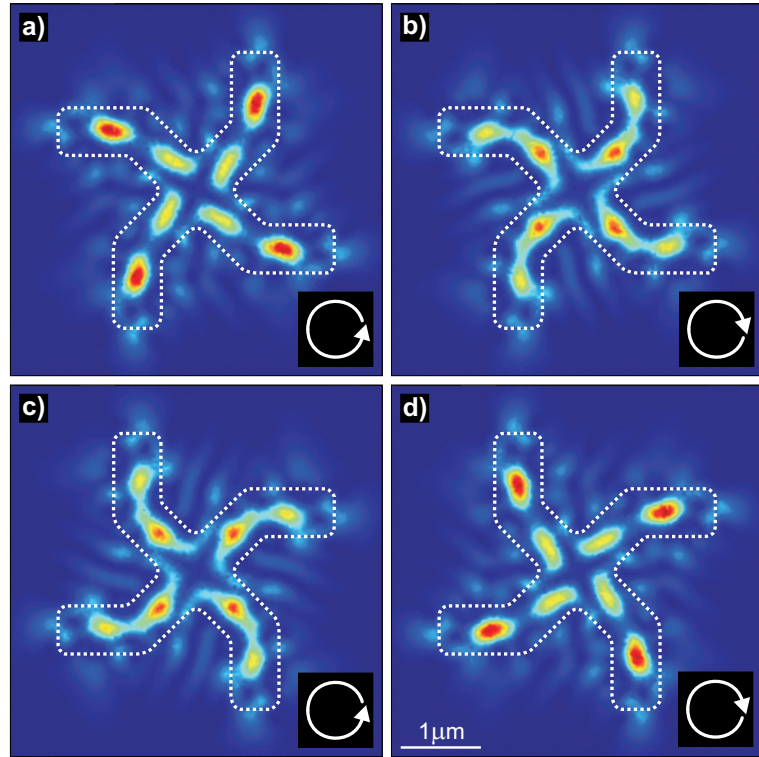
Figure 3.5: A single gammadion (the shape is indicated by the dashed line) is milled into a material with complex dielectric constant. Both enantiomers are excited with left- and right-circularly polarized light, respectively. Here, the FM are recorded after the reflected electromagnetic field passed through a cross-circularly polarized filter. Taken from Ref. [62].

reversed simultaneously ((a), (d) and (b), (c)). Thus, the same conclusion, namely that the interaction between PCS and light is sensitive to its polarization state, can be drawn from pure dielectric as well as from lossy PCS. In other words, the broken enantiomeric symmetry is a generic property of PCS. To get the proper mirror image in the FM one has to change the whole system, i.e., the mirror operation has to be applied to the material *and* the electromagnetic field.

3.2 Analytical Considerations

Although the outcomes of the previous section are quite intuitive it is worthwhile to elucidate the problem with a more formal description proposed by Stroucken [62, 63]. For this purpose, we start from the wave equation for the

electric field in frequency space

$$\nabla \times \nabla \times \boldsymbol{E} - \frac{\omega^2}{c^2}\boldsymbol{E} = \frac{\omega^2}{c^2}f(\boldsymbol{r})\chi(\omega)\boldsymbol{E}(\boldsymbol{r},\omega)\,, \tag{3.2}$$

where the polarization $\boldsymbol{P}$ has been expressed with the help of the linear response function χ and the patterning f

$$\boldsymbol{P}(t) = \int_{-\infty}^{t} dt'\, f(\boldsymbol{r})\chi(t-t')\boldsymbol{E}(t') \tag{3.3}$$

to conveniently account for the structure of the PCS. The magnetic field is determined from Eq. (2.8) yielding

$$\boldsymbol{H}(\boldsymbol{r},\omega) = -\frac{i}{\mu_0\omega}\nabla \times \boldsymbol{E}(\boldsymbol{r},\omega)\,. \tag{3.4}$$

According to Eq. (3.1) the transformation behavior of the FM can be analyzed by considering the projection

$$
\begin{aligned}
\boldsymbol{n}_z \cdot \boldsymbol{S}(\boldsymbol{r},\omega) &= \mathrm{Re}\left[\boldsymbol{n}_z \cdot (\boldsymbol{E}^*(\boldsymbol{r},\omega) \times \boldsymbol{H}(\boldsymbol{r},\omega))\right] \\
&= \mathrm{Re}\left[\boldsymbol{n}_z \cdot \left(\frac{1}{i\mu_0\omega}\boldsymbol{E}^*(\boldsymbol{r},\omega) \times \nabla \times \boldsymbol{E}(\boldsymbol{r},\omega)\right)\right] \\
&= \mathrm{Im}\left[\frac{1}{\mu_0\omega}\boldsymbol{n}_z \cdot \left(\sum_i E_i^*\nabla E_i - (\boldsymbol{E}^* \cdot \nabla)\boldsymbol{E}\right)\right]\,,
\end{aligned}
\tag{3.5}
$$

i.e., it is mainly required to investigate the influence of the symmetry operations on the electric field. Therefore, the formal solution of Eq. (3.2) may be written with the aid of the Green tensor which allows us finally to interpret the total electric field as functional of the incident field $\boldsymbol{E}_0(\boldsymbol{r},\omega)$ and the chiral patterning $f(\boldsymbol{r})$:

$$
\begin{aligned}
\boldsymbol{E}(\boldsymbol{r},\omega) &= \boldsymbol{E}_0(\boldsymbol{r},\omega) + \frac{\omega^2}{c^2}\int d^3r'\,\underline{\underline{G}}(\boldsymbol{r}-\boldsymbol{r}',\omega)f(\boldsymbol{r}')\chi(\omega)\boldsymbol{E}(\boldsymbol{r}',\omega) \\
&= \boldsymbol{E}\left[\boldsymbol{E}_0(\boldsymbol{r},\omega), f(\boldsymbol{r})\right]\,.
\end{aligned}
\tag{3.6}
$$

Introducing the definitions

$$\underline{\underline{G}}^{\mathrm{full}}(\boldsymbol{r},\omega) \equiv \underline{\underline{G}}(\boldsymbol{r},\omega) = \left(\underline{\underline{1}} + \frac{c^2}{\omega^2}\nabla \otimes \nabla\right)\mathcal{G}(\boldsymbol{r},\omega)\,, \tag{3.7}$$

$$\underline{\underline{G}}^{\mathrm{par}}(\boldsymbol{r},\omega) = \underline{\underline{1}}\,\mathcal{G}(\boldsymbol{r},\omega)\,, \quad \text{and} \tag{3.8}$$

$$\mathcal{G}(\boldsymbol{r},\omega) = \frac{1}{4\pi r}e^{i\omega r/c}\,, \tag{3.9}$$

one sees that $\mathcal{G}$ solves the scalar wave equation $-\Delta\mathcal{G} - \frac{\omega^2}{c^2}\mathcal{G} = \delta(r)$, the tensor $\underline{\underline{G}}^{\mathrm{full}}$ is the solution of the corresponding homogeneous equation of Eq. (3.2),

and $\underline{\underline{G}}^{\mathrm{par}}$ of the latter equation in *paraxial approximation*. This approximation is used quite frequently in optics and neglects the terms $(\nabla \cdot \boldsymbol{E})$, i.e., the $\boldsymbol{E}$-field is regarded as purely transverse [64]. That is why the difference between a full treatment of the electric field and the field in paraxial approximation shall be analyzed in more detail in the following. The fact that $\underline{\underline{G}}^{\mathrm{full}}$ indeed involves terms including $(\nabla \cdot \boldsymbol{E})$ and $\underline{\underline{G}}^{\mathrm{par}}$ does not can be seen by partially integrating the $\nabla \otimes \nabla \mathcal{G}(\boldsymbol{r}, \omega)$ part in Eq. (3.6). This leads to the expression

$$\int d^3 r' \, \mathcal{G}(\boldsymbol{r} - \boldsymbol{r}', \omega) \nabla \left(\nabla \cdot f(\boldsymbol{r}') \chi(\omega) \boldsymbol{E}(\boldsymbol{r}', \omega) \right) \tag{3.10}$$

which may be rewritten as

$$- \int d^3 r' \, \mathcal{G}(\boldsymbol{r} - \boldsymbol{r}', \omega) \nabla \left(\nabla \cdot \boldsymbol{E}(\boldsymbol{r}', \omega) \right) \tag{3.11}$$

since $\nabla \cdot \boldsymbol{D} = \epsilon_0 (\nabla \cdot E + \nabla \cdot f \chi \boldsymbol{E}) = 0$.

By considering the explicit forms of the Green functions Eqs. (3.7)-(3.9) one recognizes the particular transformation behavior

$$\mathcal{D}_\phi^{-1} \underline{\underline{G}}^{\mathrm{full}}(\mathcal{D}_\phi \boldsymbol{r}, \omega) \mathcal{D}_\phi = \underline{\underline{G}}^{\mathrm{full}}(\boldsymbol{r}, \omega) \,, \tag{3.12}$$

$$\mathcal{M}^{-1} \underline{\underline{G}}^{\mathrm{full}}(\mathcal{M} \boldsymbol{r}, \omega) \mathcal{M} = \underline{\underline{G}}^{\mathrm{full}}(\boldsymbol{r}, \omega) \,, \tag{3.13}$$

$$\underline{\underline{G}}^{\mathrm{par}}(\mathcal{D}_\phi \boldsymbol{r}, \omega) = \underline{\underline{G}}^{\mathrm{par}}(\boldsymbol{r}, \omega) \,, \quad \text{and} \tag{3.14}$$

$$\underline{\underline{G}}^{\mathrm{par}}(\mathcal{M} \boldsymbol{r}, \omega) = \underline{\underline{G}}^{\mathrm{par}}(\boldsymbol{r}, \omega) \,, \tag{3.15}$$

where Eqs. (3.14)-(3.15) are due to the fact that $\mathcal{D}_\phi$ ($\mathcal{M}$) commutes with the unit tensor as well as with $\mathcal{G}$. Now, the operators $\mathcal{D}_\phi$ and $\mathcal{M}$ are applied to the functional Eq. (3.6) which yields, after substituting $\boldsymbol{r}' \to \mathcal{D}_\phi \boldsymbol{r}'$ and $\boldsymbol{r}' \to \mathcal{M} \boldsymbol{r}'$ for the dummy integration variables, respectively, the expressions

$$\boldsymbol{E}(\mathcal{D}_\phi \boldsymbol{r}, \omega) = \boldsymbol{E}_0(\mathcal{D}_\phi \boldsymbol{r}, \omega)$$
$$+ \frac{\omega^2}{c^2} \int d^3 r' \, \underline{\underline{G}}^{\mathrm{full/par}}(\mathcal{D}_\phi \boldsymbol{r} - \mathcal{D}_\phi \boldsymbol{r}', \omega) f(\mathcal{D}_\phi \boldsymbol{r}') \chi(\omega) \boldsymbol{E}(\mathcal{D}_\phi \boldsymbol{r}', \omega)$$
$$\tag{3.16}$$

and

$$\boldsymbol{E}(\mathcal{M} \boldsymbol{r}, \omega) = \boldsymbol{E}_0(\mathcal{M} \boldsymbol{r}, \omega)$$
$$+ \frac{\omega^2}{c^2} \int d^3 r' \, \underline{\underline{G}}^{\mathrm{full/par}}(\mathcal{M} \boldsymbol{r} - \mathcal{M} \boldsymbol{r}', \omega) f(\mathcal{M} \boldsymbol{r}') \chi(\omega) \boldsymbol{E}(\mathcal{M} \boldsymbol{r}', \omega) \,.$$
$$\tag{3.17}$$

In *paraxial approximation* it is possible to insert the transformation properties Eq. (3.14)-(3.15) to immediately obtain the dependencies

$$
\begin{aligned}
\boldsymbol{E}^{\mathrm{par}}(\mathcal{D}_\phi \boldsymbol{r}, \omega) &= \boldsymbol{E}^{\mathrm{par}}\left[\boldsymbol{E}_0(\mathcal{D}_\phi \boldsymbol{r}, \omega), f(\mathcal{D}_\phi \boldsymbol{r})\right] \quad \text{and} & (3.18) \\
\boldsymbol{E}^{\mathrm{par}}(\mathcal{M} \boldsymbol{r}, \omega) &= \boldsymbol{E}^{\mathrm{par}}\left[\boldsymbol{E}_0(\mathcal{M} \boldsymbol{r}, \omega), f(\mathcal{M} \boldsymbol{r})\right]. & (3.19)
\end{aligned}
$$

Since a normally incident plane wave is invariant under rotations or mirror operations independent of its polarization state, i.e., $\boldsymbol{E}_0(\mathcal{D}_\phi \boldsymbol{r}, \omega) = \boldsymbol{E}_0(\mathcal{M} \boldsymbol{r}, \omega) = \boldsymbol{E}_0(\boldsymbol{r}, \omega)$, the scattered electric field reflects all symmetry properties of the PCS. This is also true for the projected Poynting vector Eq. (3.5) and therefore in paraxial approximation no enantiomeric symmetry breaking will occur.

However, this is completely different for the *full* treatment beyond the paraxial approximation. To make use of the transformation properties Eqs. (3.12)-(3.13), it is convenient to apply the operators $\mathcal{D}_\phi^{-1}$ and $\mathcal{M}^{-1}$ from the left to Eqs. (3.16)-(3.17). Then, the relations

$$
\begin{aligned}
\mathcal{D}_\phi^{-1} \boldsymbol{E}(\mathcal{D}_\phi \boldsymbol{r}, \omega) &= \mathcal{D}_\phi^{-1} \boldsymbol{E}\left[\mathcal{D}_\phi^{-1} \boldsymbol{E}_0(\mathcal{D}_\phi \boldsymbol{r}, \omega), f(\mathcal{D}_\phi \boldsymbol{r})\right] \quad \text{and} & (3.20) \\
\mathcal{M}^{-1} \boldsymbol{E}(\mathcal{M} \boldsymbol{r}, \omega) &= \mathcal{M}^{-1} \boldsymbol{E}\left[\mathcal{M}^{-1} \boldsymbol{E}_0(\mathcal{M} \boldsymbol{r}, \omega), f(\mathcal{M} \boldsymbol{r})\right] & (3.21)
\end{aligned}
$$

are obtained. A necessary condition for the FM fulfilling rotational symmetry is that the total electric field - and consequently the incident field $\boldsymbol{E}_0$ - satisfies the eigenvalue equation

$$
\mathcal{D}_\phi^{-1} \boldsymbol{E}_0(\mathcal{D}_\phi \boldsymbol{r}) = \lambda \boldsymbol{E}_0(\boldsymbol{r}). \tag{3.22}
$$

From the explicit representation of the operator

$$
\mathcal{D}_\phi = \begin{pmatrix} \cos\phi & \sin\phi & 0 \\ -\sin\phi & \cos\phi & 0 \\ 0 & 0 & 1 \end{pmatrix} \tag{3.23}
$$

the relevant eigenvalues $\lambda_{1,2} = \exp(\pm i\phi)$ and the corresponding eigenfunctions, i.e., the left and right handed circularly polarized states $(1, \pm i, 0)/\sqrt{2}$, are derived. This means that for circularly polarized light an arbitrary rotation of the PCS will be recovered in the FM what is consistent with Figs. 3.4 and 3.5. Moreover, since for $\phi = \pi$ the eigenvalues $\lambda_1 = \lambda_2$ are degenerate, any linear superposition of the eigenfunctions, including linearly polarized light, fulfills the eigenvalue equation. That is why the two-fold rotational symmetry in Fig. 3.3(b),(d) is kept. Moreover, this interesting feature has been observed in Ref. [65], too. Therein, apart from linearly and circularly polarized light, also *elliptically* polarized light has been used to simulate light propagation through a four-fold gammadion hole. It is found that the intensity distribution of the light behind the structure exhibits four-fold

rotational symmetry only in the case of circularly polarized light whereas two-fold rotational symmetry occurs otherwise. Since elliptically polarized light is also composed of both eigenstates $\boldsymbol{E}_0^{\pm}$ this agrees with the above argumentation.

The same scheme can be applied to analyze the enantiomeric symmetry of the system. The corresponding eigenvalue equation reads

$$\mathcal{M}^{-1}\boldsymbol{E}_0(\mathcal{M}\boldsymbol{r}) = \lambda \boldsymbol{E}_0(\boldsymbol{r})\,. \tag{3.24}$$

Using, e.g.,

$$\mathcal{M} = \begin{pmatrix} -1 & 0 & 0 \\ 0 & 1 & 0 \\ 0 & 0 & 1 \end{pmatrix} \tag{3.25}$$

to mirror along the $(x = 0)$-line yields the relevant eigenvalues $\lambda_{1,2} = \mp 1$ and the eigenfunctions which are the linearly polarized states $(1,0,0)$ and $(0,1,0)$ being polarized either parallel or perpendicular to the line of reflection. From this it follows that for the excitation condition in Fig. 3.3(b),(d) the enantiomeric symmetry is conserved in the FM. However, this is not the case for an arbitrary superposition of linearly polarized light. Particularly since circularly polarized light does not satisfy Eq. (3.24) because of $\mathcal{M}^{-1}\boldsymbol{E}_0^{\pm} \propto \boldsymbol{E}_0^{\mp}$, the enantiomeric symmetry is broken what can be observed in the Figs. 3.4-3.5.

Altogether, the analytical considerations presented here confirm the performed numerical simulations for all kinds of polarization states of the exciting light field. It is shown that a rather naive view of the problem, namely expecting to observe the mirror image of the FM when illuminating the mirror structure, holds only in the case of the paraxial approximation. In contrast, if the material is structured on the wavelength scale also the $(\nabla \cdot \boldsymbol{E})$ contributions have to be regarded which are automatically included in the discretized form of Maxwell's Eqs. (2.7)-(2.8). It is clear that the general symmetry properties presented in this section not only hold for the gammadion structure of Sec. 3.1 but for all planar rotationally symmetric or chiral objects.

Chapter 4

Optical Properties of Semiconductor Surfaces

"God created the solids, the devil their surfaces." - Wolfgang Pauli

Optical techniques have been widely used to study the dynamics of excitations in condensed matter systems. For bulk semiconductors and heterostructures for instance the four-wave-mixing (4WM) [66–69] and the pump-probe spectroscopy [70–72] revealed important information on the temporal evolution of coherent effects in these systems and allowed the detailed investigation of dephasing and recombination processes. Also for the analysis of surfaces optical techniques are important tools. However, due to the occurrence of surface states which are in general qualitatively different from bulk states the theoretical description of the material properties is quite challenging.

In section 4.1 a rigorous treatment for the surface states based on a microscopic theory is presented. Using quasi-particle wave functions and dispersions obtained from *ab initio* band-structure calculations in combination with the semiconductor Bloch equations it is possible to take genuine surface properties into account and compute the optical properties of the Si(111)-(2×1) surface on a fully microscopic level. So far, results on linear optical spectra (surface excitons) have already been achieved with the help of many-body perturbation theory and subsequent solution of the Bethe-Salpeter equation. The advantage of the method introduced here is its straightforward extension to the description of nonlinear optical properties.

The aim of section 4.2 is the phenomenological modeling of a five-wave-mixing (5WM) experiment performed at the Si(001)-c(4×2) surface. Certainly, it would be desirable to also have a microscopic understanding of the occurring processes at this surface, but unlike to section 4.1 the considered structure is more complex and has not been treated this way up to now. Not only it is more difficult

to characterize theoretically the experimental technique which makes use of multi-photon transitions but also the examined surface has to be described with various relevant states accounting for the optical response. Basically, 5WM is a measurement which combines the 4WM-technique and second-harmonic generation (SHG). On the one hand, since the SHG is dipole forbidden in centrosymmetric bulk materials, the method is intrinsically surface sensitive for those materials. On the other hand, applying a 4WM-like method allows one to excite the semiconductor surface with a number of laser pulses from different directions and detect the radiated field in a background-free diffraction direction. A general level-model to describe a 5WM-process is shown in Fig. 4.1. Because the incoming fields have
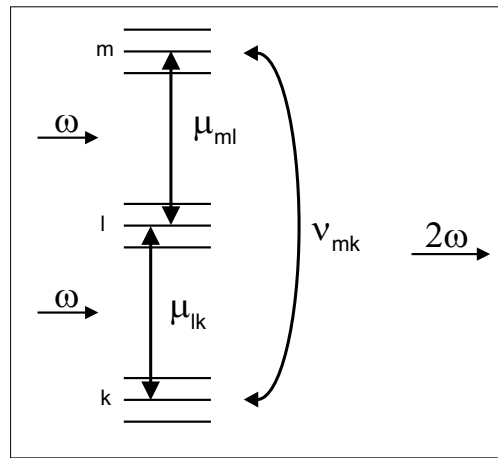

Figure 4.1: Scheme of a three-band multi-level system used to phenomenologically describe the wave-mixing experiment. All exciting pulses have a frequency close to ω and the SHG-signal is detected at 2ω. The corresponding matrix elements are denoted by $\boldsymbol{\mu}$ and $\boldsymbol{\nu}$, respectively.

approximately the frequency ω and the measured 5WM-signal is recorded at the doubled frequency 2ω, the minimal model has to consist of at least three (multi-) levels. From the modeling point of view, the physical nature of these states is not clear beforehand. They could either be true surface states or bulk states which take part in the optical mixing process. However, the distribution of the levels can be motivated from known facts of the considered material. More detailed information about the structural properties of the Si(001)-c(4×2) surface and the geometrical set-up of the experiment is given in subsection 4.2.2. It is analyzed which basic properties have to be included into the phenomenological model to reproduce the experimental findings.

4.1 Microscopic Approach for Si(111)-(2×1)

In this section a microscopic theory which is capable of describing the dynamics of optical surface excitations is presented. First, an introduction to the approach which combines the semiconductor Bloch equations with an *ab-initio* band-structure calculation is given in subsection 4.1.1. In subsection 4.1.2 numerical results in the linear regime are compared to previous model calculations and experiments. The theory is extended to the nonlinear case in subsection 4.1.3.

4.1.1 Semiconductor Bloch Equations for Surfaces

Again, the Hamiltonian for the microscopic description of the system reads

$$\hat{H} = \hat{H}_{\text{single-particle}} + \hat{H}_{\text{Coulomb}} + \hat{H}_{\text{light-matter}} \,. \tag{4.1}$$

However, compared to subsection 2.2.2, the respective parts are expanded into a k-space basis to take advantage of the underlying two-dimensional periodicity parallel to the surface.[1] Therefore, the band structure term becomes

$$\hat{H}_{\text{single-particle}} = \sum_{\mathbf{k}} E_{\mathbf{k}}^{e} \hat{c}_{\mathbf{k}}^{+} \hat{c}_{\mathbf{k}} + \sum_{\mathbf{k}} E_{\mathbf{k}}^{h} \hat{d}_{-\mathbf{k}}^{+} \hat{d}_{-\mathbf{k}} \,, \tag{4.2}$$

where $\hat{d}^{+}$ ($\hat{c}^{+}$) is a hole (electron) creation operator acting on the surface valence (conduction) band. The corresponding annihilation operator is denoted by $\hat{d}$ ($\hat{c}$). The energy dispersion of the surface valence (conduction) band is labeled $E_{\mathbf{k}}^{h}$ ($E_{\mathbf{k}}^{e}$). Note, that in the following the description is based on pure surfaces states and that bulk states are neglected. The special band structure of the considered surface makes this treatment possible, see Fig. 4.2 and the discussion below.

The Coulomb interaction is given by

$$
\begin{aligned}
\hat{H}_{\text{Coulomb}} \;=\; & \frac{1}{2} \sum_{\mathbf{k}',\mathbf{p},\mathbf{q}} V_{\mathbf{k}'+\mathbf{q},\mathbf{p}-\mathbf{q},\mathbf{p},\mathbf{k}'}^{cccc} \hat{c}_{\mathbf{k}'+\mathbf{q}}^{+} \hat{c}_{\mathbf{p}-\mathbf{q}}^{+} \hat{c}_{\mathbf{p}} \hat{c}_{\mathbf{k}'} \\
& + \frac{1}{2} \sum_{\mathbf{k}',\mathbf{p},\mathbf{q}} V_{-\mathbf{k}',-\mathbf{p},-\mathbf{p}+\mathbf{q},-\mathbf{k}'-\mathbf{q}}^{dddd} \hat{d}_{\mathbf{k}'+\mathbf{q}}^{+} \hat{d}_{\mathbf{p}-\mathbf{q}}^{+} \hat{d}_{\mathbf{p}} \hat{d}_{\mathbf{k}'} \\
& - \sum_{\mathbf{k}',\mathbf{p},\mathbf{q}} V_{\mathbf{k}'+\mathbf{q},-\mathbf{p},-\mathbf{p}+\mathbf{q},\mathbf{k}'}^{cddc} \hat{c}_{\mathbf{k}'+\mathbf{q}}^{+} \hat{d}_{\mathbf{p}-\mathbf{q}}^{+} \hat{d}_{\mathbf{p}} \hat{c}_{\mathbf{k}'} \\
& - \sum_{\mathbf{k}',\mathbf{p},\mathbf{q}} V_{-\mathbf{k}',\mathbf{k}'+\mathbf{q},\mathbf{q}-\mathbf{p},\mathbf{p}}^{dcdc} \hat{c}_{\mathbf{k}'+\mathbf{q}}^{+} \hat{d}_{\mathbf{p}-\mathbf{q}}^{+} \hat{c}_{\mathbf{p}} \hat{d}_{\mathbf{k}'} \,. \tag{4.3}
\end{aligned}
$$

_____

[1]Due to the two-dimensional periodicity only $\mathbf{k}_{\parallel}$ is a good quantum number. To simplify the notation, the subscript is dropped and the vector $\mathbf{k}$ is used in the following.

It contains terms describing the repulsion of equally charged carriers ($\hat{c}^+\hat{c}^+\hat{c}\hat{c}$ and $\hat{d}^+\hat{d}^+\hat{d}\hat{d}$), the attraction between electron and holes ($\hat{c}^+\hat{d}^+\hat{d}\hat{c}$) and the exchange term ($\hat{c}^+\hat{d}^+\hat{c}\hat{d}$). Usually, the latter contribution is omitted for direct bulk semiconductors and heterostructures since it is small in the vicinity of the Γ-point [73]. For the considered system here, however, the importance of the exchange term is not known a priori. The explicit form of the matrix elements is given on page 55.

The light-matter coupling is described by

$$\hat{H}_{\text{light}-\text{matter}} = -\mathbf{E}(t) \cdot \hat{\mathbf{P}} = -\mathbf{E}(t) \cdot \sum_{\mathbf{k}} \boldsymbol{\mu}_{\mathbf{k}}^{cd}\hat{c}_{\mathbf{k}}^+ \hat{d}_{-\mathbf{k}}^+ + \text{h.c.}, \qquad (4.4)$$

where $\mathbf{E}(t)$ is the time-dependent optical field and $\boldsymbol{\mu}_{\mathbf{k}}^{cd}$ is the interband dipole matrix element, see page 56.

To fully specify the Hamiltonian, the electronic dispersions E in Eq. (4.2) as well as the matrix elements V in Eq. (4.3) and $\boldsymbol{\mu}$ in Eq. (4.4) have to be known. Usually, e.g., for bulk semiconductors, it is often possible to use rather simple approximations. For example, close to the band edge the effective mass approximation often gives a good estimate for $E_{\mathbf{k}}$. However, due to the symmetry breaking at the surface, the situation considered here differs significantly from the three-dimensional case and therefore the quantities should be calculated regarding the actual geometrical structure of the system. Here, we apply the *GW* method[2] [74, 75] which directly yields the quasiparticle energy dispersion and the quasiparticle wave functions from which the relevant matrix elements can be computed. This approach is chosen as the starting point because it has been successfully used for the theoretical study of various semiconductor surfaces. In particular, linear optical properties of silicon and germanium surfaces have been described in good agreement with experimental measurements with the help of *ab-initio* calculations applying the local-density approximation followed by a subsequent *GW* approximation [75–81].

In the following the Si(111)-(2×1) surface is examined whose band structure is shown in Fig. 4.2. It can be seen that the surface bands D_{up} and D_{down}, respectively, appear in the band gap of the bulk material. The lowest (indirect) interband transition energy of bulk silicon is about 1.17eV whereas for the surface bands the (direct) gap is about 0.69eV. Thus, working with low enough excitation energy it is feasible to use a two band approximation which limits the numerical complexity considerably. In principle, it is straightforward to extend the formalism to other surfaces with arbitrary bands but then also, e.g., the bulk continuum states may have to be taken into account. The bands D_{up} and D_{down} have stronger dispersion along the $\overline{\Gamma J}$ and $\overline{K J'}$ line which means that the $\boldsymbol{k}$-sampling has to be more accu-

---

[2]The *ab-initio* calculations were performed by M. Rohlfing at the International University Bremen.
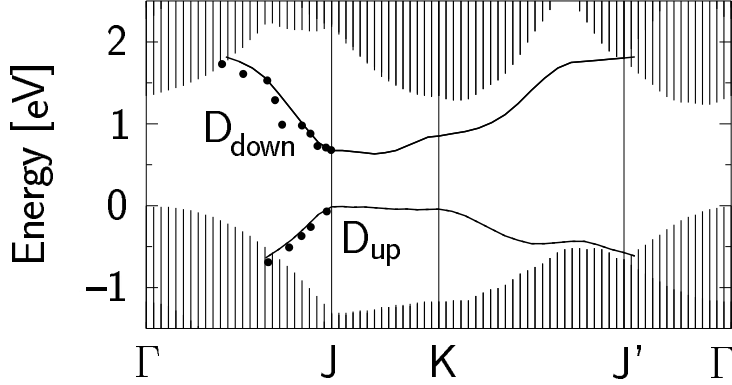
Figure 4.2: The Si(111)-(2×1) surface band structure taken from Ref. [75]. The D_up and the D_down bands are the surface valence and conduction band, respectively. The hatched areas display bulk states projected onto the surface.

rate in these directions while it can be coarser along the $\overline{JK}$ line. In total for the subsequent calculations 429 $\boldsymbol{k}$-points have been used.[3]

The Si(111)-(2×1) surface is simulated using a supercell geometry containing 16 silicon atoms saturated with two hydrogen atoms at the bottom per unit cell. A real space representation concerning the atomic arrangement is shown in Fig. 4.3(a) where several unit cells in x- and y-direction are plotted. The topmost atoms in the slab are responsible for the formation of the surface bands: the outermost Si-atoms depicted as black circles in Fig. 4.3(b) can be associated with the D_up band and the approximately 0.51Å lower lying Si-atoms indicated by white circles give rise to the D_down band [79]. If the relevant atoms which take part in optical surface experiments are viewed from the top the typical quasi one-dimensional zigzag chains, referred to as Pandey chains [82], can be recognized. They are the reason for the well-known strongly anisotropic optical behavior of this surface which also becomes apparent in the following calculations. It should be noted that for computational convenience the slab is artificially repeated in the z-direction. In this way the set-up is periodically arranged in all space directions allowing easily to write down the wave functions in a plane wave expansion

$$\varphi_{n,\mathbf{k}}(\boldsymbol{r}) = e^{i\mathbf{k}\cdot\boldsymbol{r}} u_{n,\mathbf{k}}(\boldsymbol{r}) = e^{i\mathbf{k}\cdot\boldsymbol{r}} \sum_{\{j\}} c_{n,\mathbf{k},\{j\}}\, e^{i\mathbf{G}_{\{j\}}\cdot\boldsymbol{r}}\,. \qquad (4.5)$$

Here, the Bloch functions $u_{n,\mathbf{k}}$ are expanded involving the coefficients $c_{n,\mathbf{k},\{j\}}$ and the reciprocal lattice vectors $G_{\{j\}} \equiv G_{jlm} = j\mathbf{b}_1 + l\mathbf{b}_2 + m\mathbf{b}_3$ where j,

---

[3]The line of weak dispersion is referred to as x-direction and of strong dispersion as y-direction, respectively. The number of $\boldsymbol{k}$-points is $n_x = 11$ and $n_y = 39$ with $n_x \cdot n_y = 429$. The sampling in y-direction is ten times finer than in y-direction.
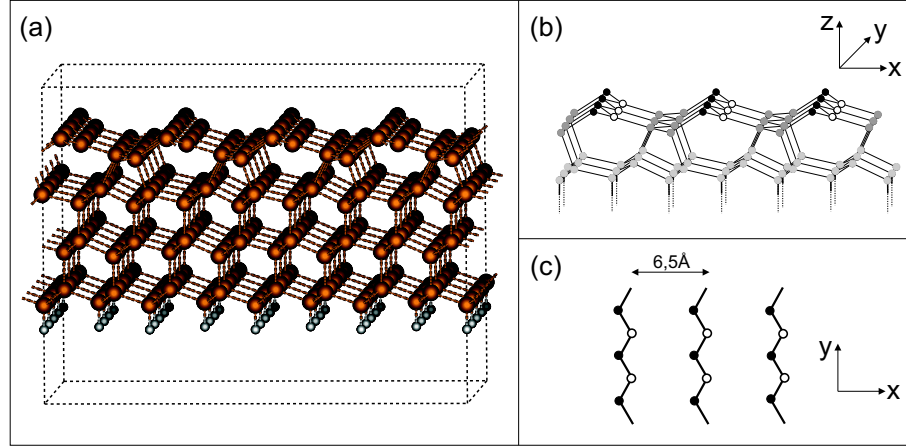
Figure 4.3: (a) The alignment of the atoms used for the calculations [83]. (b) Emphasizing the D_{up} and D_{down} atoms, see text. (c) Pandey chains viewed from the top.

l, m are integers and the $\mathbf{b}_{1,2,3}$ are the basis vectors which span the reciprocal lattice.[4] n denotes the band index $n \in \{d, c\}$. This representation is advantageous to describe the delocalized in-plane surface states and to make use of the two-dimensional periodicity of the surface. However, a lot of plane waves are needed in order to localize a state in the z-direction. A typical wave function is depicted in Fig. 4.4. Considering the changes in the probability density along the x-direction, Fig. 4.4(a), one clearly sees that the quasiparticles mainly stay in the Pandey chains which are separated approximately by 6.5Å. Within such a chain they are completely delocalized, cp. Fig. 4.4(b). As expected for a surface state the wave function is concentrated near the silicon-vacuum interface at $z = 0$, Fig. 4.4(c), and rapidly decays to zero in either z-direction. In the latter graph the white region refers to the vacuum and the gray region to silicon.

Knowing the wave functions φ the Coulomb matrix elements can be computed via the six-dimensional integral

$$V_{\mathbf{k}_1\mathbf{k}_2\mathbf{k}_3\mathbf{k}_4}^{l_1 l_2 l_3 l_4} = \int d^3 r_1 d^3 r_2 \, \varphi_{l_1,\mathbf{k}_1}^*(\mathbf{r}_1) \varphi_{l_2,\mathbf{k}_2}^*(\mathbf{r}_2) V(\mathbf{r}_1, \mathbf{r}_2) \varphi_{l_3,\mathbf{k}_3}(\mathbf{r}_2) \varphi_{l_4,\mathbf{k}_4}(\mathbf{r}_1) .$$

$$(4.6)$$

The superscript of V indicates the bands and the subscript the wave vectors of the involved wave functions. Furthermore, a statically screened Coulomb potential is assumed which reads in real-space representation

$$V(\mathbf{r}_1, \mathbf{r}_2) = \frac{\exp(-\kappa|\mathbf{r}_1 - \mathbf{r}_2|)}{\epsilon|\mathbf{r}_1 - \mathbf{r}_2|} .$$

$$(4.7)$$
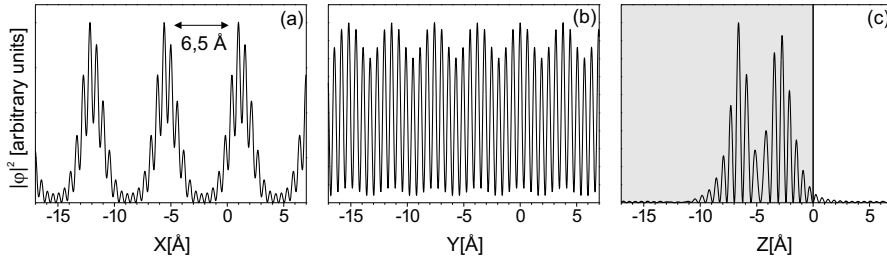
---

[4]See also Tab. D.5 in App. D.

Figure 4.4: Squared modulus of a typical wave function $|\varphi_{n,\mathbf{k}}(\boldsymbol{r})|^2$ of the Si(111)-(2×1) surface as function of one component while the others stay fixed.

The introduction of the screening parameter κ ensures that the matrix elements are not considerably affected by the artificial repetition of the slab in z-direction if the inverse screening length κ^{-1} is on the order of the extension of the supercell in that direction. At the same time, the screening should be weak enough to influence the interaction parallel to the surface only slightly. Both requirements are fulfilled for $\kappa^{-1} \approx 20\text{Å}$. It has been checked on a trial basis by using the potential

$$V(\mathbf{r}_1, \mathbf{r}_2) = \frac{\Theta(L_c - |\mathbf{r}_1 - \mathbf{r}_2|)}{\epsilon|\mathbf{r}_1 - \mathbf{r}_2|} \tag{4.8}$$

that slab-slab interactions have to be suppressed since otherwise spurious resonances appear in the linear spectra. In Eq. (4.8) Θ is the Heaviside function and L_c is a cut-off parameter. For $|\mathbf{r}_1 - \mathbf{r}_2| < L_c$ Eq. (4.8) resembles the usual Coulomb potential and for $|\mathbf{r}_1 - \mathbf{r}_2| > L_c$ it is zero. If L_c is set to about 20Å, approximately the same exciton binding energy is found as for the Yukawa potential with $\kappa^{-1} \approx 20\text{Å}$; the deviation is less than a few percent. However, since a screened potential is more physical than a simple cut-off, the potential in Eq. (4.7) has been used exclusively in the following. In addition, the dielectric constant appearing in Eq. (4.7) was fixed to $\epsilon = 6.0$ which is an average of the dielectric constants of silicon and vacuum.

Also the dipole matrix elements describing the light-matter interaction are computed using the quasiparticle wave functions

$$\boldsymbol{\mu}_{\mathbf{k}}^{cd} = -e \int d^3r\, \varphi_{c,\mathbf{k}}^*(\mathbf{r})\, \mathbf{r}\, \varphi_{d,\mathbf{k}}(\mathbf{r}) \,. \tag{4.9}$$

Since a homogeneous excitation of the surface is assumed, only vertical optical transitions are present in $\boldsymbol{k}$-space.

The complete scheme to specify the Hamiltonian is again shown in the following diagram:

$$
\text{ab initio method} \rightarrow
\begin{cases}
E_{\mathbf{k}}^{e/h} \\
\varphi_{c/d,\mathbf{k}}(\mathbf{r}) \rightarrow
\begin{cases}
V_{\mathbf{k,q,k,q}}^{cccc}, \; V_{\mathbf{k,q,k,q}}^{dddd}, \; V_{\mathbf{k,q,k,q}}^{cddc}, \; V_{\mathbf{k,q,q,k}}^{dcdc} \\
\boldsymbol{\mu}_{\mathbf{k}}^{cd}
\end{cases}
\end{cases}
$$

The quasiparticle energies appear directly in the Hamiltonian whereas the quasiparticle wave functions determine the Coulomb and dipole matrix elements, respectively.

The dynamical properties of the system are calculated via the Heisenberg equations of motion. Applying the time-dependent Hartree-Fock approximation results in coupled equations for the interband coherence $p_{\mathbf{k}} = \langle \hat{d}_{-\mathbf{k}}\hat{c}_{\mathbf{k}}\rangle$ and the electron and hole densities $n_{e,\mathbf{k}} = \langle \hat{c}_{\mathbf{k}}^{+}\hat{c}_{\mathbf{k}}\rangle$ and $n_{h,\mathbf{k}} = \langle \hat{d}_{-\mathbf{k}}^{+}\hat{d}_{-\mathbf{k}}\rangle$, respectively.

$$
\begin{aligned}
-i\frac{\partial}{\partial t}p_{\mathbf{k}} &= -(E_{\mathbf{k}}^{e} + E_{\mathbf{k}}^{h})p_{\mathbf{k}} \\
&\quad +(1 - n_{e,\mathbf{k}} - n_{h,\mathbf{k}})\left[\boldsymbol{\mu}_{\mathbf{k}}^{cd}\cdot\mathbf{E}(t) + \sum_{\mathbf{q}}(V_{\mathbf{k,q,k,q}}^{cddc} - V_{\mathbf{q,k,k,q}}^{dcdc})p_{\mathbf{q}}\right] \\
&\quad +p_{\mathbf{k}}\sum_{\mathbf{q}}\left(V_{\mathbf{k,q,k,q}}^{cccc}n_{e,\mathbf{q}} + V_{\mathbf{k,q,k,q}}^{dddd}n_{h,\mathbf{q}}\right) ,
\end{aligned} \tag{4.10}
$$

$$
\begin{aligned}
-i\frac{\partial}{\partial t}n_{e,\mathbf{k}} &= (\boldsymbol{\mu}_{\mathbf{k}}^{cd}p_{\mathbf{k}}^{*} - \boldsymbol{\mu}_{\mathbf{k}}^{cd*}p_{\mathbf{k}})\cdot\mathbf{E}(t) \\
&\quad +p_{\mathbf{k}}^{*}\sum_{\mathbf{q}}(V_{\mathbf{k,q,k,q}}^{cddc} - V_{\mathbf{q,k,k,q}}^{dcdc})p_{\mathbf{q}} - p_{\mathbf{k}}\sum_{\mathbf{q}}(V_{\mathbf{q,k,q,k}}^{cddc} - V_{\mathbf{k,q,q,k}}^{dcdc})p_{\mathbf{q}}^{*} ,
\end{aligned} \tag{4.11}
$$

$$
\begin{aligned}
-i\frac{\partial}{\partial t}n_{h,\mathbf{k}} &= (\boldsymbol{\mu}_{\mathbf{k}}^{cd}p_{\mathbf{k}}^{*} - \boldsymbol{\mu}_{\mathbf{k}}^{cd*}p_{\mathbf{k}})\cdot\mathbf{E}(t) \\
&\quad +p_{\mathbf{k}}^{*}\sum_{\mathbf{q}}(V_{\mathbf{k,q,k,q}}^{cddc} - V_{\mathbf{q,k,k,q}}^{dcdc})p_{\mathbf{q}} - p_{\mathbf{k}}\sum_{\mathbf{q}}(V_{\mathbf{q,k,q,k}}^{cddc} - V_{\mathbf{k,q,q,k}}^{dcdc})p_{\mathbf{q}}^{*} .
\end{aligned} \tag{4.12}
$$

These equations are quite similar to the standard semiconductor Bloch equations [44, 84] which are used, e.g., for the study of bulk semiconductors. Inspecting the Coulomb sums reveals that all momentum states are coupled due to the many-body interaction. Besides, for the energies appearing in Eq. (4.10) one finds the typical Hartree-Fock energy renormalizations ($\sum_{\mathbf{q}} V_{\mathbf{k,q,k,q}}^{cccc}n_{e,\mathbf{q}}$) and ($\sum_{\mathbf{q}} V_{\mathbf{k,q,k,q}}^{dddd}n_{h,\mathbf{q}}$) for the electron and hole single-particle energies, respectively. Moreover, the phase space filling $(1 - n_{e,\mathbf{k}} - n_{h,\mathbf{k}})$ enters as a pre-factor for the effective light field. However, the Coulomb matrix elements showing up in the

Eqs. (4.10)-(4.12) have a substantially different structure. Whereas in the three-dimensional case the Coulomb interaction of the carriers depends simply on their relative distance in real space – because of the presence of an isotropic medium which leads to the potential $V_{\mathbf{q}} = V_q \propto 1/q^2$ in $\mathbf{k}$-space – the matrix elements used here have a more complicated indexing. Furthermore, it should be noted that the exchange contribution, which enters the equations of motion with opposite sign compared to the direct Coulomb term, slightly reduces the attraction between electrons and holes.

4.1.2 Linear Regime

In the linear optical regime it is sufficient to solve only Eq. (4.10) with vanishing densities, i.e., $n_{e,\mathbf{k}} = n_{h,\mathbf{k}} = 0$. From this the total macroscopic polarization can be computed as the sum over all microscopic polarizations

$$\boldsymbol{P}(t) = \sum_{\mathbf{k}} \boldsymbol{\mu}_{\mathbf{k}}^{cd} p_{\mathbf{k}} \tag{4.13}$$

yielding the linear absorption $\alpha(\omega) \propto \omega \, \mathrm{Im}[\boldsymbol{P}(\omega)]$ after a Fourier transform [44].

However, for better comparison with the available experimental data it is instructive to calculate the differential reflectivity spectrum [85]

$$\frac{\Delta R}{R}(\omega) = \frac{8\pi d}{\mathrm{Re}[\epsilon_{\mathrm{bulk}} - 1]} \frac{1}{\lambda} \, \mathrm{Im} \left[\frac{\sum_{\mathbf{k}} \mu_{\mathbf{k},i}^{cd} \, p_{\mathbf{k}}(\omega)}{E_i(\omega)} \right] \tag{4.14}$$

which is proportional to the linear absorption. Here, λ is the vacuum wavelength, i labels the polarization direction of the light field, and d is the thickness of the slab. Experimentally $\frac{\Delta R}{R}(\omega)$ is detected by measuring the reflectivity of the surface before and after oxidation from the ratio $(R_{\mathrm{clean}} - R_{\mathrm{ox}})/R_{\mathrm{ox}}$. Since the oxidation is associated with the destruction of the surface states one effectively removes the bulk contributions in this measurement.

The interband coherences $p_{\mathbf{k}}$ are driven by the external field via $\boldsymbol{\mu}_{\mathbf{k}}^{cd} \cdot \mathbf{E}(t)$. Therefore, if one artificially neglects the Coulomb interaction, i.e., $V \equiv 0$ for all index combinations, it is easily possible to examine how the system reacts on different polarization directions of the exciting pulse. The information about the surface geometry is incorporated in the dipole matrix elements which are determined according to Eq. (4.9). The results of such a calculation using the parameters in Tab. D.5 is shown in Fig. 4.5. If the light field is polarized perpendicular to the Pandey chains the detected signal is very weak. If, however, it is polarized parallel to the chains the absorption contributes considerably. These findings also persist with Coulomb interaction [86] and are consistent with experimental observations
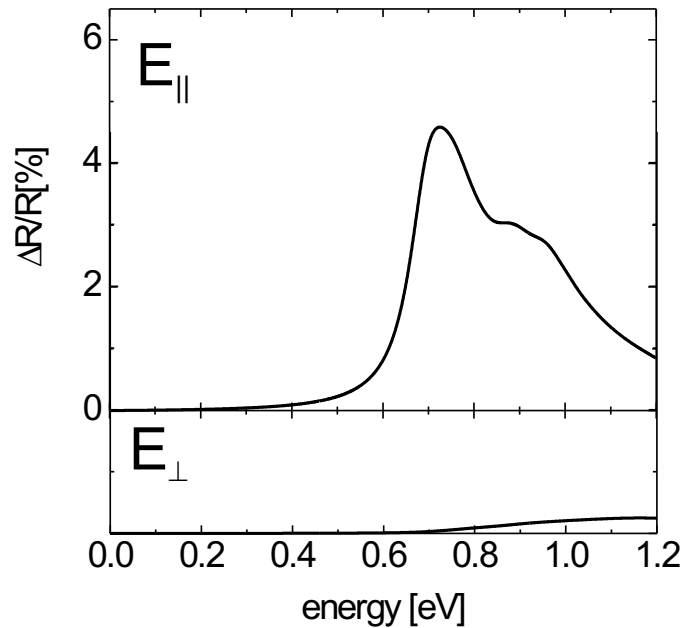
Figure 4.5: The calculated differential reflectivity spectrum of the Si(111)-(2×1) surface for artificially switched off Coulomb interaction. The exciting field is polarized parallel or perpendicular to the Pandey chains. The ordinates have the same scale, i.e., the signal is small for perpendicular polarization.

in Refs. [85,87,88]. Thus, the following discussion concentrates on the excitation of the surface with light polarized in y-direction, i.e., parallel to the chains.

Solving Eq. (4.10) *with* Coulomb interaction and inserting the $p_{\mathbf{k}}$'s into Eq. (4.14) yields the differential reflectivity spectrum shown as solid line in Fig. 4.6. It is basically dominated by a single surface exciton resonance which is located at about 0.45 eV. The calculations have been performed by supplementing the equations for the microscopic polarizations with phenomenological decay rates resulting in a homogeneous broadening of 50 meV. Additionally, the experimental data from Ref. [87] has been plotted, see dots in Fig. 4.6. Not only the spectral position of the resonance of the computed curve but also its height are in good agreement with the measured values. The dashed line shows again the spectrum without Coulomb interaction. From the difference of the energetical positions of the surface gap and the surface exciton one can determine an exciton binding energy of about 0.25 eV. Very similar results were obtained in Ref. [75] where the Bethe-Salpeter equation for electron-hole excitations has been solved
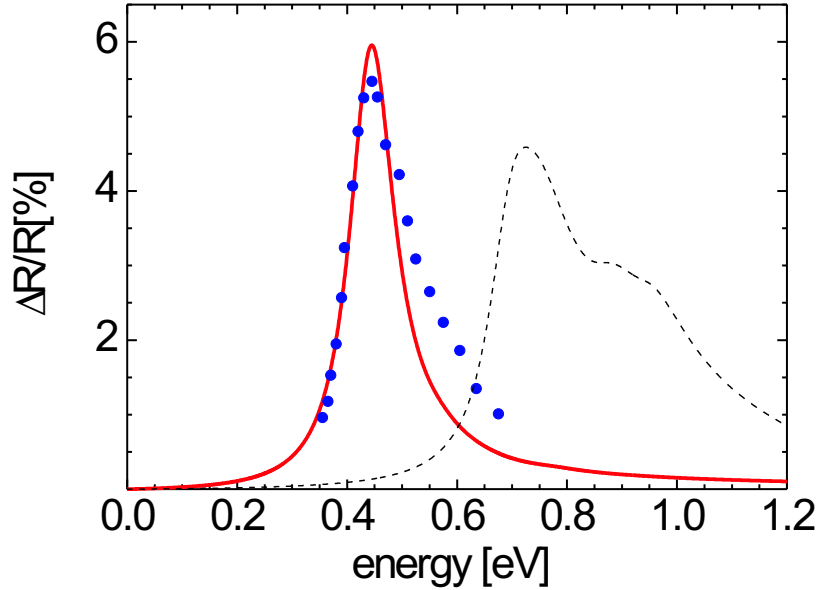
Figure 4.6: Differential reflectivity spectrum of the Si(111)-(2×1) surface. The solid line shows the calculated signal, the dots refer to experimental values, and for comparison the result with vanishing Coulomb interaction Fig. 4.5 is replotted, see dashed line. In all cases the exciting pulse was polarized parallel to the chains. After Ref. [89].

using matrix diagonalization. This demonstrates the reasonableness of the presented approach in the linear regime.

4.1.3   Nonlinear Regime

For the discussion of nonlinear effects, also the carrier densities $n_{e,\mathbf{k}}$ and $n_{h,\mathbf{k}}$ have to be computed, i.e., Eqs.(4.10)-(4.12) have to be solved simultaneously. In the following, the optical Stark effect of the Si(111)-(2×1) surface exciton will be investigated. The Stark effect behavior of excitons in direct-gap semiconductor heterostructures is well understood [44, 90, 91] and since the linear spectrum of the considered surface is mainly governed by one resonance similar results are to be expected here.

The principle set-up of the experiment is sketched in Fig. 4.7. The surface is excited with a spectrally narrow pump pulse which is tuned sufficiently below the exciton to ensure an off-resonant pumping. With the help of an ultrashort, i.e., spectrally-broad probe pulse, the changes of the absorption spectrum depending

on the pump intensity are monitored. Temporally the probe pulse arrives at the maximum of the pump pulse. In the numerical evaluation the pump pulse is treated nonpertubatively whereas the probe pulse is weak enough to be taken into account only up to first order [92]. The relevant parameters are given in Tab. D.6.
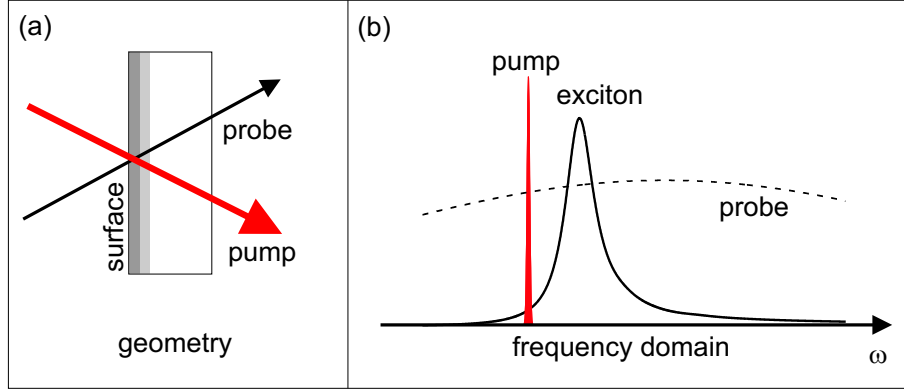

Figure 4.7: (a) Schematic geometry used to investigate the optical Stark effect: A strong pump pulse is incident on the surface while the induced absorption changes are monitored by a weak pulse. (b) Spectral distribution of the respective pulses.

The effect of varying the pump intensity on the absorption spectra can be seen in Fig. 4.8. In the left graph, Fig. 4.8(a), the full absorption spectra $\alpha(\omega)$ are shown and in the right graph, Fig. 4.8(b), the corresponding differential absorption spectra are displayed. The latter is defined as [44]

$$\delta\alpha(\omega) = \alpha(\omega)[\text{with pump}] - \alpha(\omega)[\text{without pump}] \tag{4.15}$$

and can be used beneficially for analyzing the arising features beyond the linear case. For instance, the differential absorption exhibits a dispersive line shape with positive contributions on the energy above and negative contributions below the exciton. This correlates with a blueshift (shift to higher energies) of the exciton resonance itself in the full spectra. Basically, the shifting-behavior can be understood with the help of a two level system coupled to a strong periodic electric field. The field causes a renormalization of the energies leading to new optical transitions in the system.

An additional feature which can be observed in Fig. 4.8 is the reduction of the exciton's peak height with increasing pump intensity. It is due to the blocking term $(1 - n_{e,\mathbf{k}} - n_{h,\mathbf{k}})$ appearing in Eq. (4.10). Since for low enough excitation intensities a pulse generates more carriers the stronger it is, the absorption of the probe beam decreases with increasing pump intensity resulting in the so called "bleaching".
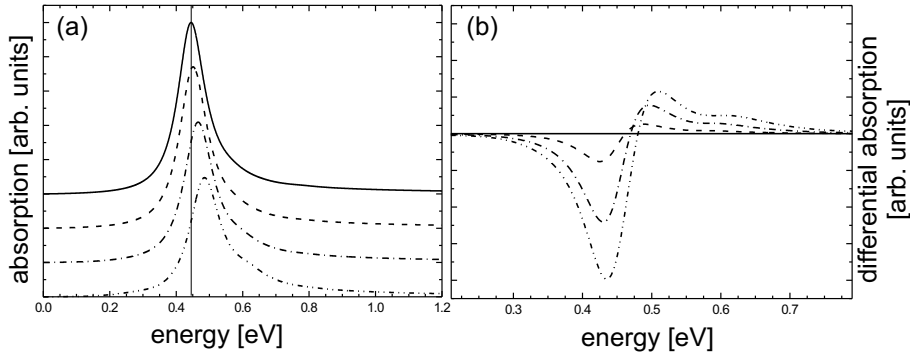
Figure 4.8: (a) Absorption spectra for different pump intensities I (displaced vertically). The linear spectrum ($I = 0$) is plotted as a solid line, the other relative intensities are $I = I_0$ (dashed), $I = 4I_0$ (dash-dotted), and $I = 9I_0$ (dash-dot-dotted). (b) The corresponding differential absorption spectra. Taken from Ref. [89].

Of course, the pump-induced effects depend on the detuning of the pump pulse. Since the polarizations and densities become smaller the more off-resonant the excitation takes place, the total nonlinear optical response of the surface is also reduced if the detuning is increased. This can be seen in Fig. 4.9 where the dependence of bleaching on the detuning of the pump pulse has been plotted for different excitation intensities. For all intensities the bleaching is large if the detuning is small and it becomes less pronounced if the system is excited farther below the exciton. However, it turns out that this development is more apparent for low pump intensities, i.e., the detuning dependence is steeper in that case. Due to saturation effects the strength of the system's excitation is limited. Thus, the bleaching can hardly be increased even for smaller detuning if the pumping is strong.

As in the linear case, also for the investigation of the optical Stark effect it becomes transparent that the nonlinear optical properties of the Si(111)-(2×1) surface are dominated by one strong exciton resonance. These findings are in agreement with those expected for quasi-one-dimensional systems and emphasize once more the fact that the surface structure is build up of the Pandey chains which exhibit a much stronger coupling along each chain than between them.

Generally, one may ask whether the analysis performed so far is valid concerning the treatment of the equations of motion on the Hartree-Fock level. To answer this question and to find novel nonlinear properties of the particular surface the theory has recently been extended in Ref. [93] to study many-body correlations. In this work the equations of motion have been set up in the so-called coherent $\chi^{(3)}$-limit which allows the description of the coherent dynamics of the system up
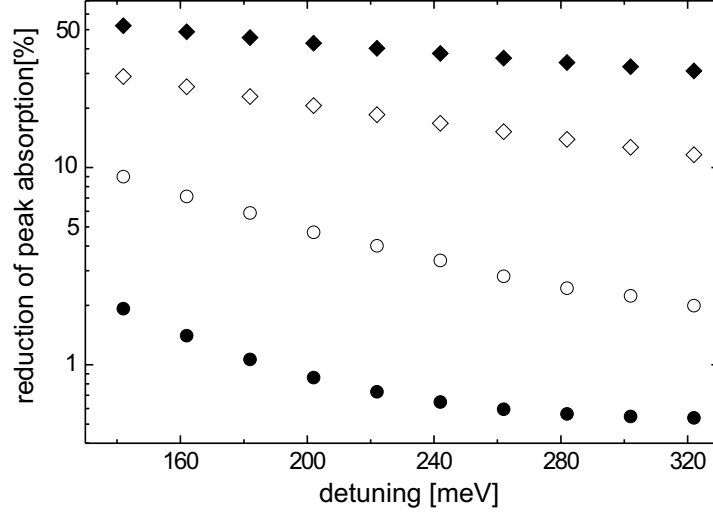
Figure 4.9: For various intensities the percentage of bleaching, i.e., the reduction of the absorption peak height compared to the linear spectrum, is shown on a logarithmic scale as function of the detuning of the pump pulse below the surface exciton. The relative intensities are $I_1/16$, $I_1/4$, I_1, and $4I_1$ displayed as closed circles, open circles, open diamonds, and closed diamonds, respectively. Taken from Ref. [89].

to third order in the exciting field [94, 95]. With the $\chi^{(3)}$-theory, it is in particular possible to investigate biexcitonic effects which give rise to new signatures in the optical spectra [90]. Thus, besides the two-point amplitude $p = \langle \hat{d}\hat{c} \rangle$ it is also necessary to calculate the four-point quantity $B = \langle \hat{d}\hat{c}\hat{d}\hat{c} \rangle$.[5] All density-like variables can be expressed via conservative laws with the help of these quantities in the coherent limit.

The detailed analysis of the equations which are derived and solved in Ref. [93] is rather involved and shall not be considered here. However, it is possible to check the results presented above and gain some general insight into the dependence of the differential absorption on the detuning of the pump pulse by projecting the full set of equations onto a simple three level system containing a ground state with zero energy, a single-exciton state p, and a biexciton state $\bar{B}$, respectively [91, 93]. This allows to integrate the resulting equations analytically for the following exciting light field

$$E(t) = \tilde{E}_{\mathrm{pump}} e^{i\epsilon_{\mathrm{pump}} t/\hbar} + \tilde{E}_{\mathrm{probe}} \delta(t) . \tag{4.16}$$

---

[5]Sometimes it is useful to examine $\bar{B}$, i.e., the pure correlation part of B from which the Hartree-Fock contributions have been removed.

Here, a cw-pump containing one single frequency $\epsilon_{\text{pump}}/\hbar$ and a spectrally white probe pulse are considered. Furthermore, the differential absorption Eq. (4.15) can be written as the sum of three terms

$$\delta\alpha(\omega) = \delta\alpha^{pb}(\omega) + \delta\alpha^{C,1st}(\omega) + \delta\alpha^{C,corr}(\omega)\,, \tag{4.17}$$

where "pb" denotes the Pauli-blocking contribution, "$C,1st$" is the first-order Coulomb term, and "$C,corr$" the correlation contribution [90, 96]. Only the last term includes true correlation effects in the sense that it is due to four-point quantities (containing $\bar{B}$) whereas the other two terms arise already in a third-order Hartree-Fock theory.

Let Δ be the detuning between the pump and the exciton state p, i.e., $\Delta = \epsilon_{\text{pump}} - \epsilon_p$, and the biexciton energy approximately twice the exciton energy $\epsilon_{\bar{B}} \approx 2\epsilon_p$. Then, it can be shown [91, 93] that for large detuning[6] the leading terms of the respective contributions behave as

$$
\begin{aligned}
\delta\alpha^{pb}(\omega) &\propto |\Delta|^{-1} &,& \\
\delta\alpha^{C,1st}(\omega) &\propto |\Delta|^{-2} &,& \quad \text{and} \\
\delta\alpha^{C,corr}(\omega) &\propto |\Delta|^{-3} &.&
\end{aligned}
\tag{4.18}
$$

Since the regime for analyzing the optical Stark effect in the limit of large detuning basically fulfills the above mentioned criteria, one can see from Eq. (4.18) that a description with the help of Eqs. (4.10)-(4.12) derived in time-dependent Hartree-Fock approximation is tolerable because the most decisive terms are included in that theory. However, for resonant and near-resonant excitation at the exciton the correlation terms play an important role. It should be noted that the conclusions with the help of the reduced model leading to Eq. (4.18) are also confirmed by numerical solutions of the full set of $\chi^{(3)}$-equations [93].

---

[6]At least the detuning has to be considerably larger the exciton linewidth.

4.2   Phenomenological Approach for Si(001)-c(4×2)

This section starts with the derivation of the optical Bloch equations for a three-band multi-level system in subsection 4.2.1. These equations are used in subsection 4.2.2 to investigate a particular 5WM-experiment at a Si(001)-c(4×2) surface. A brief comment on phenomenological models in general is presented in subsection 4.2.3.

4.2.1   Optical Bloch Equations for Second-Harmonic Generation

According to the phenomenological model in Fig. 4.1, see page 51, the corresponding Hamiltonian

$$\hat{H} = \hat{H}_0 + \hat{H}_{\text{light}-\text{matter}} \tag{4.19}$$

contains the term $\hat{H}_0$ which includes the energies of the different levels and the term $\hat{H}_{\text{light}-\text{matter}}$ describing the coupling between the system and a classical light field. Distinct from section 4.1, in the following analysis the many-body interaction is not considered explicitly in that kind of treatment.

The material part can be written as sum over the energies of the relevant states, i.e.,

$$H_0 = \sum_k \epsilon_k \hat{c}_k^+ \hat{c}_k + \sum_l \epsilon_l \hat{c}_l^+ \hat{c}_l + \sum_m \epsilon_m \hat{c}_m^+ \hat{c}_m \,. \tag{4.20}$$

From now on the convention will be used to label the states of the lowest band with k, of the intermediate band with l, and that of the highest band with m, respectively.

The light matter interaction is given in dipole approximation by

$$\hat{H}_{\text{light}-\text{matter}} = -\mathbf{E}(t) \cdot \hat{\mathbf{P}} \,. \tag{4.21}$$

The description of a SHG experiment requires the inclusion of ω-resonant as well as 2ω-resonant contributions into the polarization operator

$$\hat{\mathbf{P}} = \hat{\mathbf{P}}^{(\omega)} + \hat{\mathbf{P}}^{(2\omega)} \,. \tag{4.22}$$

Here, the definitions

$$\hat{\mathbf{P}}^{(\omega)} = \sum_{lk} (\boldsymbol{\mu}_{lk} \hat{c}_l^+ \hat{c}_k + \boldsymbol{\mu}_{lk}^* \hat{c}_k^+ \hat{c}_l) + \sum_{ml} (\boldsymbol{\mu}_{ml} \hat{c}_m^+ \hat{c}_l + \boldsymbol{\mu}_{ml}^* \hat{c}_l^+ \hat{c}_m) \tag{4.23}$$

and

$$\hat{\mathbf{P}}^{(2\omega)} = \sum_{mk} (\boldsymbol{\nu}_{mk} \hat{c}_m^+ \hat{c}_k + \boldsymbol{\nu}_{mk}^* \hat{c}_k^+ \hat{c}_m) \tag{4.24}$$

have been introduced where $\boldsymbol{\mu}$ and $\boldsymbol{\nu}$ are the dipole matrix elements according to Fig 4.1. The considered experiment, however, is performed with incident pulses which have a frequency close to ω. This means that predominantly the resonant transitions occurring in $\hat{\mathbf{P}}^{(\omega)}$ will be driven by the field and therefore the approximation

$$\hat{H}_{\text{light}-\text{matter}} \approx -\mathbf{E}(t) \cdot \hat{\mathbf{P}}^{(\omega)} \tag{4.25}$$

is feasible. Nevertheless, the measured SHG-signal is proportional to $\langle \hat{\mathbf{P}}^{(2\omega)} \rangle$.

In order to determine the temporal evolution of the three-band multi-level system, one has to set up the equations of motion for the interband coherences

$$p_{lk}^{(\omega)} = \langle \hat{c}_l^+ \hat{c}_k \rangle , \qquad p_{ml}^{(\omega)} = \langle \hat{c}_m^+ \hat{c}_l \rangle , \qquad p_{mk}^{(2\omega)} = \langle \hat{c}_m^+ \hat{c}_k \rangle , \tag{4.26}$$

and the intraband coherences

$$n_{kk'} = \langle \hat{c}_k^+ \hat{c}_{k'} \rangle , \qquad n_{ll'} = \langle \hat{c}_l^+ \hat{c}_{l'} \rangle , \qquad n_{mm'} = \langle \hat{c}_m^+ \hat{c}_{m'} \rangle . \tag{4.27}$$

For equal index i, the expectation value $\langle n_{ii} \rangle$ is the population of the state i. Note, that $p_{mk}^{(2\omega)}$ directly enters into the SHG-signal.

Evaluating Heisenberg's equation, Eq. (2.40) on page 26, for each operator combination and taking expectation values results in the coupled set of equations

$$\begin{aligned}
\frac{\partial}{\partial t} p_{lk}^{(\omega)} = \ & -\frac{i}{\hbar}(\epsilon_k - \epsilon_l)p_{lk}^{(\omega)} \\
& -\frac{i}{\hbar}\mathbf{E}(t) \cdot \sum_{k'} \boldsymbol{\mu}_{lk'}^* n_{k'k} + \frac{i}{\hbar}\mathbf{E}(t) \cdot \sum_{l'} \boldsymbol{\mu}_{l'k}^* n_{ll'} \\
& -\frac{i}{\hbar}\mathbf{E}^*(t) \cdot \sum_{m'} \boldsymbol{\mu}_{m'l} p_{m'k}^{(2\omega)} ,
\end{aligned} \tag{4.28}$$

$$\begin{aligned}
\frac{\partial}{\partial t} p_{ml}^{(\omega)} = \ & -\frac{i}{\hbar}(\epsilon_l - \epsilon_m)p_{ml}^{(\omega)} \\
& -\frac{i}{\hbar}\mathbf{E}(t) \cdot \sum_{l'} \boldsymbol{\mu}_{ml'}^* n_{l'l} + \frac{i}{\hbar}\mathbf{E}(t) \cdot \sum_{m'} \boldsymbol{\mu}_{m'l}^* n_{mm'} \\
& +\frac{i}{\hbar}\mathbf{E}^*(t) \cdot \sum_{k'} \boldsymbol{\mu}_{lk'} p_{mk'}^{(2\omega)} ,
\end{aligned} \tag{4.29}$$

$$\begin{aligned}
\frac{\partial}{\partial t} p_{mk}^{(2\omega)} = \ & -\frac{i}{\hbar}(\epsilon_k - \epsilon_m)p_{mk}^{(2\omega)} \\
& -\frac{i}{\hbar}\mathbf{E}(t) \cdot \sum_{l'} \boldsymbol{\mu}_{ml'}^* p_{l'k}^{(\omega)} + \frac{i}{\hbar}\mathbf{E}(t) \cdot \sum_{l'} \boldsymbol{\mu}_{l'k}^* p_{ml'}^{(\omega)} ,
\end{aligned} \tag{4.30}$$

$$
\frac{\partial}{\partial t} n_{kk'} = -\frac{i}{\hbar} (\epsilon_{k'} - \epsilon_k) n_{kk'}
$$
$$
- \frac{i}{\hbar} \mathbf{E}^*(t) \cdot \sum_l \boldsymbol{\mu}_{lk} p_{lk'}^{(\omega)} + \frac{i}{\hbar} \mathbf{E}(t) \cdot \sum_l \boldsymbol{\mu}_{lk'}^* p_{lk}^{(\omega)*}, \qquad (4.31)
$$

$$
\frac{\partial}{\partial t} n_{ll'} = -\frac{i}{\hbar} (\epsilon_{l'} - \epsilon_l) n_{ll'}
$$
$$
+ \frac{i}{\hbar} \mathbf{E}^*(t) \cdot \sum_k \boldsymbol{\mu}_{l'k} p_{lk}^{(\omega)} - \frac{i}{\hbar} \mathbf{E}(t) \cdot \sum_k \boldsymbol{\mu}_{lk}^* p_{l'k}^{(\omega)*}
$$
$$
- \frac{i}{\hbar} \mathbf{E}^*(t) \cdot \sum_m \boldsymbol{\mu}_{ml} p_{ml'}^{(\omega)} + \frac{i}{\hbar} \mathbf{E}(t) \cdot \sum_m \boldsymbol{\mu}_{ml'}^* p_{ml}^{(\omega)*}, \qquad (4.32)
$$

and

$$
\frac{\partial}{\partial t} n_{mm'} = -\frac{i}{\hbar} (\epsilon_{m'} - \epsilon_m) n_{mm'}
$$
$$
+ \frac{i}{\hbar} \mathbf{E}(t)^* \cdot \sum_l \boldsymbol{\mu}_{m'l} p_{ml}^{(\omega)} - \frac{i}{\hbar} \mathbf{E}(t) \cdot \sum_l \boldsymbol{\mu}_{ml}^* p_{m'l}^{(\omega)*}. \qquad (4.33)
$$

To numerically solve Eqs. (4.28)-(4.33) it is convenient to expand the variables in powers of the exciting light field and to time integrate the respective quantities order by order. Depending on the particular experiment only certain coherences contribute and likewise the directions of the incoming pulses and the measured signal determine the spatial directions of all in-between needed quantities which have to be calculated. Furthermore, each density-like equation is supplemented by a relaxation term proportional to the inverse of the relaxation time T_1 and all interband coherences are damped with the dephasing time T_2. In doing so the temporal decay of the considered quantities which is naturally due to microscopic processes is modeled in a phenomenological way.

4.2.2 Three-Pulse Second-Harmonic Generation

In this subsection the optical Bloch equations, Eqs. (4.28)-(4.33), are used to elucidate the main features observed in a 5WM-experiment at a Si(001)-c(4×2) surface [97–99]. The semiconductor is excited with three ultrashort laser pulses, denoted as a, b, and c, respectively, of frequency ω which impinge on the sample from different directions. Fig. 4.10 shows this scenario schematically: the incident fields have the wave vectors $\mathbf{k}_a$, $\mathbf{k}_b$, and $\mathbf{k}_c$, and the diffracted 2ω signal is detected along the line $\mathbf{K} = 2\mathbf{k}_c + \mathbf{k}_b - \mathbf{k}_a$. For low excitation intensities it is sufficient to calculate the quantities which arise up to fourth-order in the field. The

optical Bloch equations have to be solved for all coherences and populations that finally contribute to the fourth-order polarization

$$P^{(2\omega)}[4; (-1|1|2)] \quad = \quad \sum_{mk} (\boldsymbol{\nu}_{mk} p_{mk}^{(2\omega)}[4; (-1|1|2)] + \boldsymbol{\nu}_{mk}^{*} p_{mk}^{(2\omega)*}[4; (-1|1|2)]) .$$

(4.34)

The explicit system of equations containing all relevant variables is given in appendix C[7].
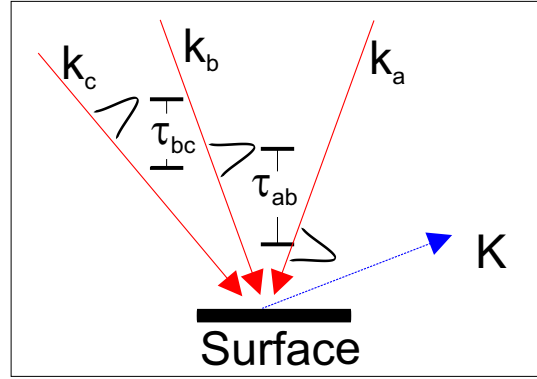
Figure 4.10: Sketch of the five-wave-mixing experiment: Three beams whose time-ordering can be arbitrarily arranged are incident on the surface from different directions and the generated second-harmonic signal is measured in a background-free diffraction direction.

One of the advantages of the 5WM-technique is that it is possible to probe interband coherences as well as populations by adequately choosing the respective delays of the pulses. For example, if the two beams a and b arrive approximately at the same time, i.e., if they have temporal overlap, and the third beam c is incident considerably later, the SHG signal contains information about the carrier relaxation at the surface. On the other hand, varying the delay between a and b allows one to investigate the dephasing-behavior of the optical polarizations at ω-frequency. Even the dynamics of the second-order 2ω polarization is accessible if beam c arrives first.

The following figures show various dependencies of the SHG-intensity on different time delays. Here, the definitions $\tau_{ab} = t_a - t_b$ and $\tau_{bc} = t_c - t_b$ are used, where $t_{a,b,c}$ represents the real time of the pulse. This means that a pulse sequence of normal order a, b, c corresponds to delay times $\tau_{ab} < 0$ and $\tau_{bc} > 0$.

---

[7]Further comments on the notation in Eq. (4.34) can also be found in appendix C.

Figure 4.11: The graph shows the time-integrated second-harmonic intensity (Eq. (4.35)) for various (fixed) τ_{bc} as function of the delay $\tau_{a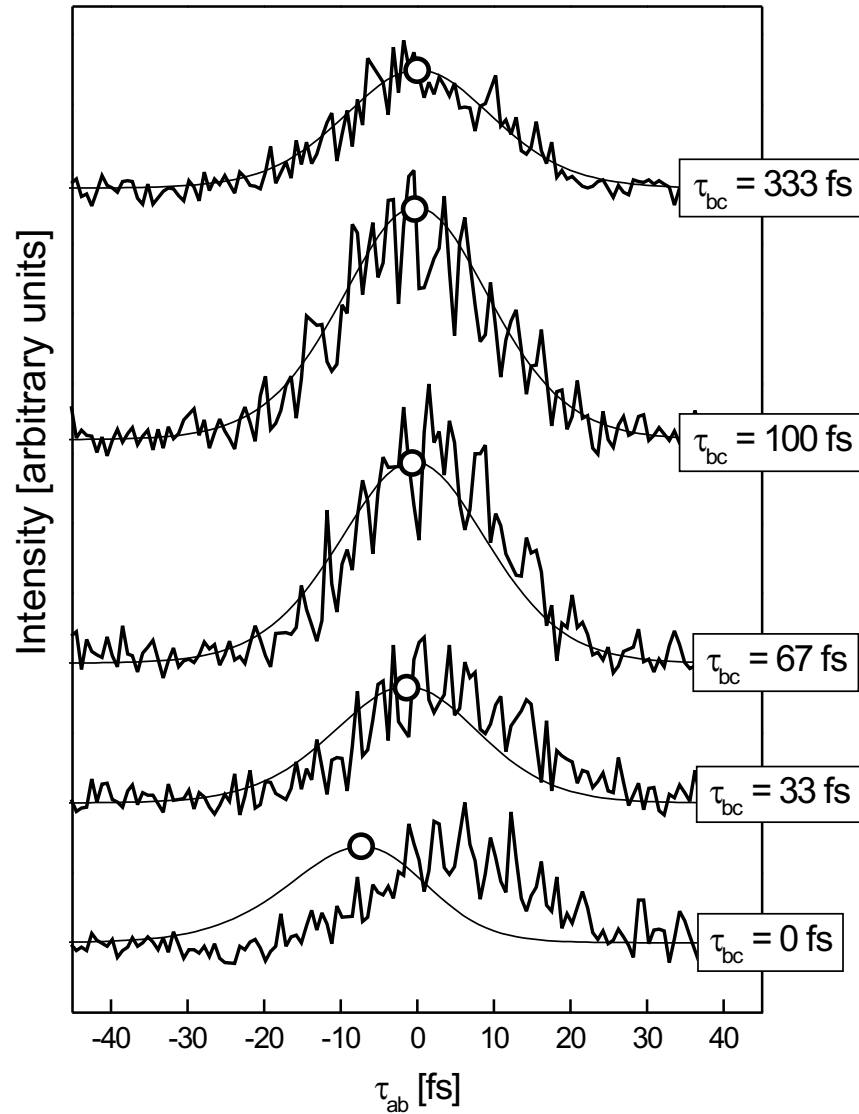b}$. The thick lines represent experimental data [97] and the thin lines are results of calculations described below. For illustration the maximum of each curve which enters Fig. 4.12 has been marked with a circle. After Ref. [98].

In Fig. 4.11, the time-integrated SH-intensities

$$I_{\tau_{bc}}(\tau_{ab}) = \int dt \, |P^{(2\omega)}[4;(-1|1|2)](t,\tau_{ab},\tau_{bc} = \text{fixed})|^2 \qquad (4.35)$$

depending on τ_{ab} are plotted. Each curve corresponds to a different delay time τ_{bc} which is kept fixed while the delay τ_{ab} is varied. The experimental data [97] are displayed as thick solid lines and show in either case a sharply peaked 2ω response close to $\tau_{ab} = 0$. The thin lines are results of model calculations which are discussed below, see page 73.

First of all, the peak intensity of the SHG signal is analyzed in detail. If one picks out the maximum for each of the time-integrated curves and relates it to the delay τ_{bc} one obtains Fig. 4.12. Here, the maxima from a series of measurements are plotted as black circles for a range of τ_{bc} of several hundreds of femtoseconds. A striking feature of this graph is that the SH-intensity exhibits a delayed rise on the order of 50-100 fs. More precisely, it has a sharp local maximum at $\tau_{bc} = 0$, steps through a minimum at $\tau_{bc} = 13$ fs and reaches its absolute maximum at about 100 fs.

This is surprising since intuitively one would expect the maximum to appear around $\tau_{bc} = 0$ as the result of the coherent interaction of all three beams what becomes transparent if the model in Fig. 4.1 is reduced to a simple three-level model. Then, the calculated intensity has the shape displayed in Fig. 4.13. In this graph the dotted line was obtained by solving the optical Bloch equations for a single three-level system (model (b) in Fig. 4.13) whereas the solid line is the result of using an inhomogeneous ensemble of three-level systems whose $|l\rangle$ states were shifted in energy (model (a) in Fig. 4.13). Clearly, a strong peak can be observed for the simultaneous arrival of all pulses for both cases. Since the intermediate states in model (a) are mostly detuned with respect to the incident pulse, i.e., the pulses a and b create on the average less population in these levels than for model (b), the peak around $\tau_{bc} = 0$ is even more pronounced for (a). It should be noted that the curves have been normalized in such a way that their long term limits coincide. The input parameters for the calculations are given in Tab. D.7.

To find a more appropriate model system explaining the delayed rise we thoroughly examine the most important characteristics of the Si(001)-c(4×2) surface band structure, see Fig. 4.14(a). Since the laser system which is used in the experiment delivers photons with energies of $\hbar\omega = 1.55$ eV a resonant transition between the D_{up} and D_{down} band may occur in such a way that the excited electrons are generated high up in the band. This process is depicted as $\mathbf{k}_{\parallel,1}$ in Fig. 4.14(a). Having an excess amount of energy, the electrons will rapidly scatter towards lower energies and accumulate in another region of $\mathbf{k}$-space. The relaxation could be phonon assisted or due to Coulomb scattering. When the other pulses arrive
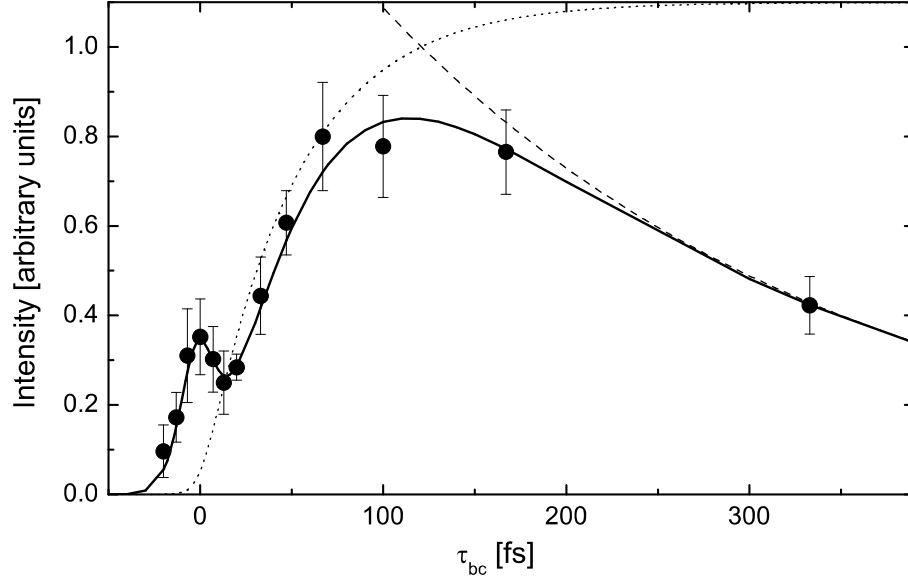
Figure 4.12: The graph displays data extracted from Fig. 4.11 and similar measurements namely the second-harmonic peak intensity, i.e., the maximum of the 5WM signal for varying τ_{ab} (and fixed τ_{bc}) as function of τ_{bc}. The black circles are taken from experimental results, the solid line follows from a calculation using the model in Fig. 4.14(b). The dashed and dotted line show the relaxation and population of the intermediate state of the model system as described in the text. Taken from Ref. [98].

somewhat later, they might involve transitions with different energies and momenta. Particularly, the emission of the 2ω-photon could take place at $\mathbf{k}_{\parallel,2} \neq \mathbf{k}_{\parallel,1}$.

These properties are incorporated straightforwardly in a model consisting of two coupled three-level systems which is sketched in Fig. 4.14(b). The system which is denoted as S corresponds to the $\mathbf{k}_{\parallel,1}$-situation in $\boldsymbol{k}$-space. The transition between $|k\rangle$ and $|l\rangle$ is chosen such that it is resonant with ω, all other transitions are considered to contribute less and therefore their matrix elements have been reduced (indicated as dashed lines). For the S'-system the $|l'\rangle$ state has been decreased in energy, i.e., the lower and upper transitions are detuned with respect to ω. On the other hand, the matrix element $\boldsymbol{\nu}_{k'm'}$ was enhanced in order to increase the 2ω-response which is assumed to take place predominantly at $\mathbf{k}_{\parallel,2}$. Both systems are linked together by a population transfer from state $|l\rangle$ to $|l'\rangle$.

Calculated data using this model and the corresponding Eqs. (C.1)-(C.14) are plotted in Fig. 4.12. The solid line clearly shows the particular behavior of the SH-intensity having a local maximum around 0 and a delayed absolute maximum. The shape can be understood by recognizing that the pulses a and b create a much stronger population at S than at S' since the former transition is driven
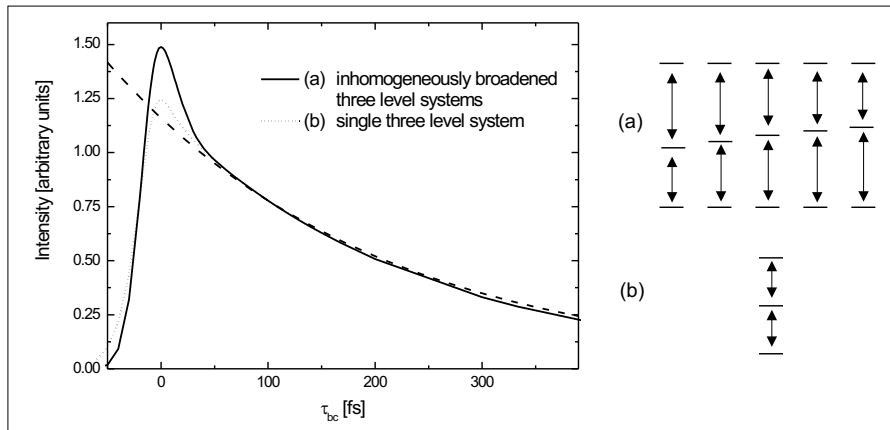
Figure 4.13: Exemplary model calculations for the second-harmonic peak intensity with an inhomogeneous ensemble of three-level systems, see solid line (model (a)), and a single three-level system, see dotted line (model (b)) which are deficient to explain the delayed rise. The relaxation behavior from Fig. 4.12 indicated as dashed line has been replotted.
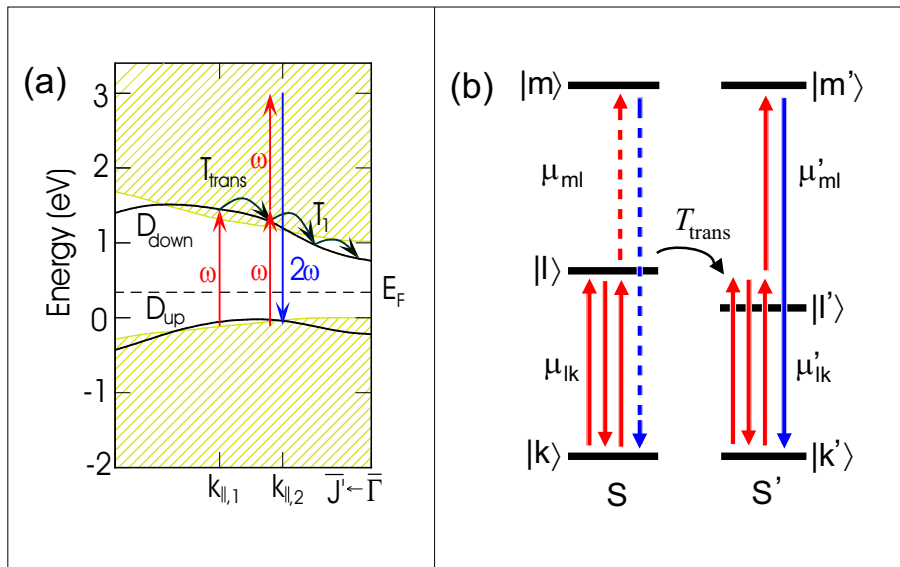
Figure 4.14: (a) Band structure of the Si(001)-c(4×2) surface taken from Ref. [100]. (b) Two coupled three-level systems which represent the most important transitions in the band structure; explanation is given in the text.

resonantly. In the course of time, this population is transferred from the state $|l\rangle$

to $|l'\rangle$ meaning that the parameter T_{trans} determines the position of the delayed peak with respect to τ_{bc}. Its relative height compared to the local maximum is dependent on the value of the matrix element of the 2ω transition. Altogether, the model calculations with the chosen parameters reproduce very well the experimental findings. For explanatory reason two more curves are displayed in Fig. 4.12. The dashed line represents a graph proportional to $\exp^2(-t/T_1)$ and demonstrates that the long term decay of the SH-intensity is determined by the carrier relaxation time T_1. The dotted line[8] depicts the population of the state $|l'\rangle$ and emphasizes once more that the second peak is mainly due to the transfer process and that the carriers excited directly at $\mathbf{k}_{\|,2}$ play a minor role.

Turning back to the time-integrated plot Fig. 4.11 the model can be checked in more detail. The computed signals are inserted as thin solid lines. For large τ_{bc}, i.e., when it is possible to interpret the experiment in terms of a diffraction off a transient grating, the experimental and the theoretical curves are in good agreement. The peak height, the peak position as well as the width of the signal are reproduced well. However, if $|\tau_{bc}|$ is small and is on the order of a few pulse widths meaning that all three pulses begin to overlap, a temporal shift towards negative τ_{ab} can be observed for the calculated intensity. This shift is marginally present for $\tau_{bc} = 33$ fs and becomes more apparent for $\tau_{bc} = 0$ fs, cp. Fig. 4.11, which indicates that the proposed model does not match the experiment in this regime. It is clear that the simple model does not include all characteristics which might play an important role for this time-ordering of the pulses. For example, three-photon resonances which could be decisive when all beams are simultaneously present are neglected completely. Furthermore, only discrete levels have been considered and the continuum of off-resonant transitions has not been taken into account. Surely, as for all phenomenological approaches, also the current model is valid only in a certain parameter range. Nevertheless, it is appropriate to describe the feature of the delayed rise quite well. Particularly the idea of the carrier relaxation within the D_{down} band which involves the pumping and probing at different points in $\mathbf{k}$-space and therefore the transfer of population on a time scale of about $T_{\mathrm{trans}} \approx 50$ fs has been sustained by the experiments of Ref. [101].

4.2.3   Two-Pulse Second-Harmonic Generation

As pointed out above, the validity of the parameter range of phenomenological models should be carefully inspected. This shall be demonstrated by shortly reviewing the results presented in Refs. [99, 103]. The aim is the description of a two-pulse second harmonic experiment performed on a the Si(111)-(7×7) surface. The principle set up is sketched in Fig. 4.15(a): Two pulses a and b traveling

---

[8]To obtain this line T_1 was set to infinity and $n_{l'l'}$ of the S'-system was recorded.
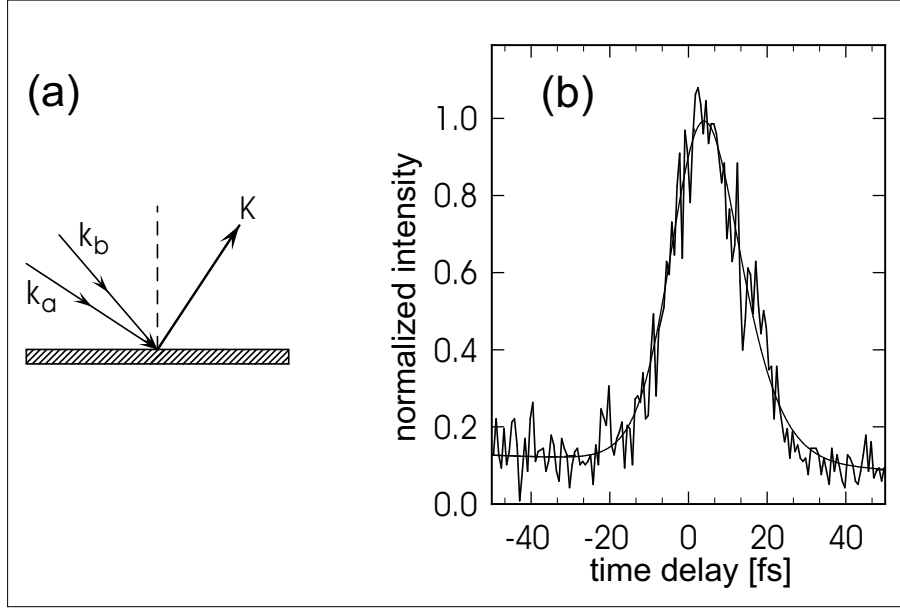
Figure 4.15: (a) Schematical diagram of a five-wave-mixing experiment using two laser beams. (b) Experimental data for the second-harmonic intensity taken from Ref. [102], the line is a guide to the eye.

in direction $\mathbf{k}_a$ and $\mathbf{k}_b$ impinge on the surface and the diffracted signal in direction $\mathbf{K} = 3\mathbf{k}_b - \mathbf{k}_a$ is measured. This geometry is very similar to the common four-wave mixing[9] though due to the upconversion from an ω to a 2ω signal an additional photon is involved changing the detection direction and making the process surface specific since now it is of fourth-order in the exciting field. In terms of nonlinear optics the time-integrated intensity is given by

$$I(\tau) = \int dt \, |P^{(2\omega)}[4; (-1|3)](t, \tau)|^2 \,. \tag{4.36}$$

Here, τ is the delay between the two pulses where $\tau > 0$ corresponds to a situation where pulse a is incident before pulse b. Fig. 4.15(b) displays experimental data for the SHG intensity when the surface is excited with two ultrashort laser pulses with duration shorter than 14 fs. Clearly, the diffracted signal decays on a very short time scale having a full width half maximum of less than 20 fs. In the following, the question is addressed whether it is possible to obtain any information on the dephasing time T_2 entering the microscopic polarization equation from a phenomenological model.

---

[9]The four-wave mixing is a third order process and the signal is detected in the background free direction $\mathbf{K} = 2\mathbf{k}_b - \mathbf{k}_a$, see, e.g., Ref. [104].

It has been motivated in Ref. [103] that the modeling of the SHG experiment at the Si(111)-(7×7) surface has at least to include an energetic distribution of the lowest level in a three level-system. The reason is that the ultrashort laser pulses cover a wide spectrum of transition energies and that it is likely that the continuum of bulk states which overlap with the surface states participate in the optical response. However, there exist in principle two different superpositions to fulfill this requirement. One which is from now on referred to as "inhomogeneous" model is shown in Fig. 4.16(b) and the other one which is called "homogeneous" model in Fig. 4.16(d).

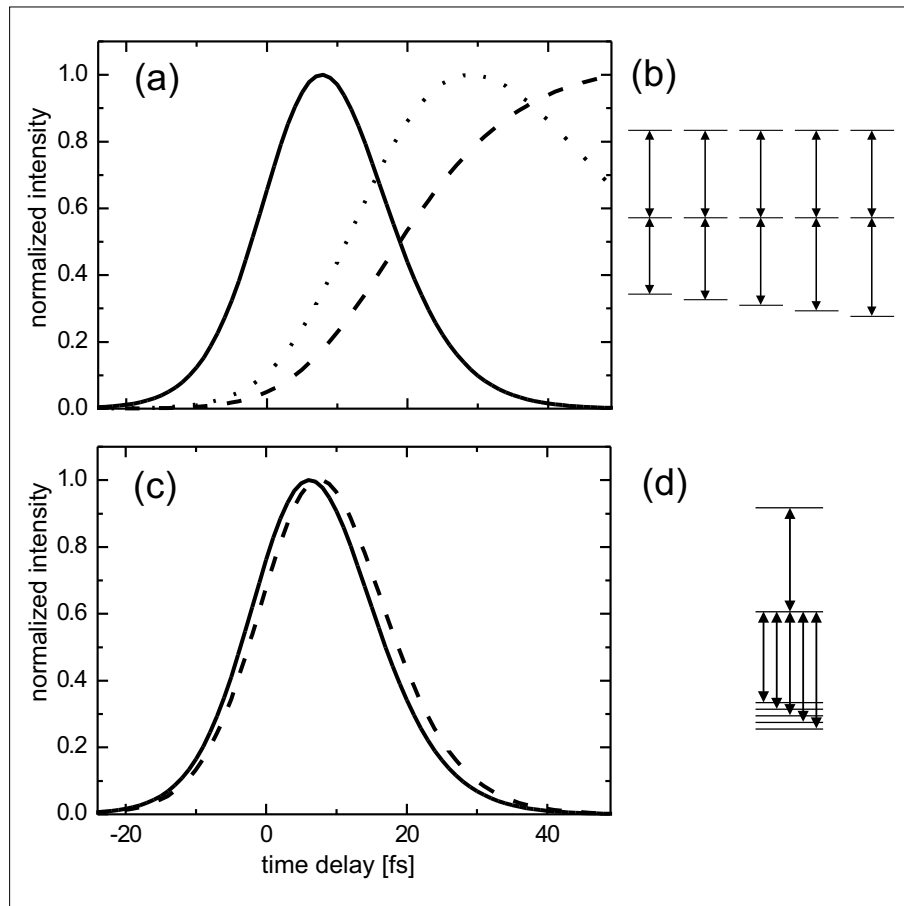Figure 4.16: (a) Numerical results for the inhomogeneous model shown in (b). The lines correspond to a dephasing time of $T_2 = 3$ fs (solid), $T_2 = 100$ fs (dotted), and $T_2 = \infty$ (dashed). (c) Outcomes if the homogeneous model (d) is applied. The dephasing times are $T_2 = 3$ fs (solid) and $T_2 = \infty$ (dashed). After Ref. [99].

The inhomogeneous model consists of an ensemble of uncoupled three-level

systems whose ground state energy differ slightly. This is a typical photon echo like situation [44, 104–106], i.e., due to the inhomogeneous broadening of the lowest transition the time-resolved signal will "re-phase" and emit a light pulse depending on the delay time τ. If the dephasing is neglected completely, the time-integrated curve stays at a constant value for large τ. More precisely, regarding time-integrated 4WM for $T_2 = \infty$, the signal rises with increasing time delay and reaches its maximum when the delay equals the temporal width of the photon echo. This width is generally determined by the energetic distribution of the inhomogeneous levels and the spectral width of the exciting pulses. For finite T_2 the time-integrated intensity is proportional to $\exp(-4\tau/T_2)$ in the long time limit. The results of the SHG experiment can be qualitatively understood with the 4WM concept involving an additional photon. Numerical calculations solving the corresponding optical Bloch equations for the model are shown in Fig. 4.16(a) displaying the SHG-intensities for different dephasing times T_2. Obviously a very short dephasing time is required to come close to the experimental findings with the inhomogeneous model.

However, turning to the homogeneous model the situation is completely different. As can be seen from Fig. 4.16(d) all valence band states are coupled to the same excited state. This leads to an irreversible decay of the polarization [107] and therefore the time-integrated signal decays even for infinite dephasing time. Fig. 4.16(c) shows the simulated results for $T_2 = 3$ fs and $T_2 = \infty$ which are basically identical. Thus, within the homogeneous model one cannot draw any conclusion about the dephasing time.

The two examples visualize the difficulties occurring when working with phenomenological models. Approximately the same results (rapid decay of the SH-intensity) may be reproduced with very different model assumptions: the inhomogeneous model requires T_2 times less than 5 fs whereas the homogeneous model even works with $T_2 \rightarrow \infty$. Thus, in general it is desirable to analyze every process on a microscopic basis.

Chapter 5

Summary and Outlook

In chapter 2 a theory to self-consistently treat the vector Maxwell semiconductor Bloch equations is developed. That way it is possible to describe the coupled dynamics of the electromagnetic field and the photoexcitations of the material. In section 2.1 the standard FDTD-method is introduced which allows the numerical solution of Maxwell's equation for pure dielectrics. Moreover, the algorithm is extended to include the polarization originating from an optically active material. This polarization is computed using a microscopic theory, section 2.2, which accounts for the modified Coulomb interaction in the considered structure.

As an application, in section 2.3 hybrid semiconductor photonic crystal systems, e.g., an array of quantum wires near to a two-dimensional photonic crystal, are analyzed. The theory includes the proper description of both the longitudinal as well as the transversal electromagnetic field which arise from the structured dielectric environment. It is shown that these effects induce a space-dependent band gap and excitonic resonances and also result in a spatially-inhomogeneous distribution of quasi-equilibrium electron and hole populations. This leads to observable changes in the absorption/gain spectra of the hybrid system compared to a homogeneous surrounding. As a consequence, basically two strong excitonic peaks appear in the spectra depending on the volume ratio between material and air. Under the considered conditions it is possible to have gain for the energetically lower excitonic resonance at smaller total densities than in a homogeneous medium. Furthermore, it is demonstrated that the relative influence on the absorption/gain due to a change in the carrier density is more pronounced if the field is concentrated in that regions in which the charge carriers predominantly accumulate.

The tailoring of hybrid structures offers a great variety of interesting applications in the future. First of all, one could improve the individual components of the system. By changing the geometric structure of the photonic crystal, e.g., by using a different type of lattice, varying the dimensionality of the

periodicity, exchanging the constitutive dielectric materials and their volume ratio, it is possible to determine a desired density of states for light. The active semiconductor material could be modified as well. One could include quantum dots, wires, and wells into the structure. The theory presented in section 2.2 could be extended beyond Hartree-Fock approximation. Above all it is preferable to apply a more sophisticated laser description which also treats the carrier densities on a dynamic level. Certainly, the most spectacular features could arise when adjusting both the photonic crystal and the active material. If due to the periodic longitudinal modulations the charge carriers are suitably accumulated and match a proper electromagnetic mode this could result in superradiant light emission. Even the non-periodic concentration of light in regions with high carrier density could lead to interesting effects in the strong coupling regime.

In chapter 3 the interaction between electromagnetic waves and planar chiral nanostructures is investigated. It is shown by means of numerical calculations in section 3.1 that the properties of the reflected light depend on the polarization state of the exciting field. If the incident wave is circularly polarized, the enantiomeric symmetry is broken, i.e., when the planar chiral structure is exchanged with its mirror structure the resulting flow maps are no mirror images of each other. This is only the case if both, the chirality of the material and the handedness of the exciting light field, are changed simultaneously. Regarding the symmetry of the considered gammadions it is found that for circularly polarized excitation the four-fold rotational symmetry of the structure can be observed in the flow maps whereas for linearly polarized excitation they only exhibit a two-fold rotational symmetry.

The numerical results are confirmed by a theoretical analysis in section 3.2. In a detailed derivation it is pointed out that the effects can only be understood using the full Maxwell's equations since otherwise, e.g., when applying the paraxial approximation, the enantiomeric symmetry is *not* broken.

So far, the material in the numerical simulations has been described by a fixed dielectric constant. One could extend this treatment to account for the metallic nature of the gammadions which are mostly used in the experiments to study planar chirality. Altering the arrangement of the individual chiral elements forming the complete array and making use of photonic-crystal like effects could enhance the "optical activity" for certain frequencies. In any case, planar chiral structures could be useful for technical applications, since the artificial construction allows to tailor the size of the structure. In contrast to, e.g., naturally occurring chiral molecules, one could take advantage of the effects in arbitrary wave-length regions.

In chapter 4 an investigation of optical properties of semiconductor surfaces is presented. Generally, the situation at a surface is quite different from bulk material and therefore common approximations cannot be applied to those systems. For particular surfaces, two kinds of approaches are pursued: A complete microscopic treatment in Sec. 4.1 and a phenomenological description in Sec. 4.2.

The microscopic approach which is used to describe the linear and nonlinear optical properties of the Si(111)-(2×1) surface is based upon the semiconductor Bloch equations. All relevant matrix elements which enter the Hamiltonian of the system, namely the energy dispersions of the quasi particles, the dipole matrix elements, and the Coulomb matrix elements are directly obtained via *ab-initio* band structure theory. It is shown that the calculated linear spectra are in good agreement with experimental results and previous calculations. The optical response exhibits an obvious anisotropic behavior which is related to its geometric structure, i.e., the formation of Pandey chains. It is demonstrated that the linear spectrum is dominated by one strongly absorbing excitonic resonance and that the exciton binding energy is approximately 250 meV. Furthermore, the theory is used to study the nonlinear regime. As an application the dynamical optical Stark effect is analyzed. The dependence of the pump-induced absorption changes on the pump intensity is investigated revealing a blue shift and bleaching of the exciton resonance for increasing pump intensity. It is mentioned that the method can be further extended to also describe many-body correlations in the optical response of the Si(111)-(2×1) surface. In principle, it is straightforward to apply this approach to other semiconductor surfaces, however, one may be limited by numerical matters. Since the actual geometric structure has to be considered to set up the Hamiltonian, the treatment is in general numerically quite demanding. The reason why the method is conveniently applicable for the particular case of Si(111)-(2×1) surface is that due to the occurrence of merely two surface bands the number of participating surface states is restricted and still manageable.

The situation is more complicated for the presented three-pulse five-wave-mixing experiment at a Si(001)-c(4×2) surface. A more complex surface band structure and the particular experiment, i.e., the detection of a 2ω photon after the excitation with several beams, involves too many states to make a microscopic treatment easily possible. Therefore, a phenomenological approach is chosen to describe the main experimentally observed features of the SHG-signal. The attention is basically turned to the delayed peak in the measured time-delay-dependent 2ω intensity. It is proven by numerically solving the optical Bloch equations that this characteristic peak can be explained with the help of two coupled three-level systems which are connected to each other via a transfer process. Considering the band structure the transfer probably corresponds to a scattering of the excited electrons within the D_{down} surface band which occurs on time scales of about

50-250 fs. This process is favored by the model system since it is impossible to obtain the delayed peak by a mere superposition of three-level systems alone which would mean exciting and probing the surface at the same point in $\mathbf{k}$-space. Although the experimental data is reproduced very well for the present case it is pointed out explicitly that phenomenological models do not have predictive ability in general. Therefore, a two-pulse five-wave-mixing experiment at a Si(111)-(7×7) surface is reviewed showing that no conclusions about the dephasing time can be obtained as long as the nature of the underlying states is unknown. Nevertheless, as demonstrated for the Si(001)-c(4×2) surface, phenomenological models may provide indications about the microscopic processes if they are combined with experimental findings.

In future treatments it is desirable to go beyond the phenomenological modeling and base the theory on a microscopic description. This comprises miscellaneous surfaces – not only the ones considered here – and different types of surface specific experiments. It is straightforward to include multiple bands into the formalism presented in section 4.1. Moreover, as has been shown, the coupling to continuum states may be decisive for the optical response of a surface. Thus, it is a outstanding challenge to incorporate these states into the microscopic description. A further extension would be the proper treatment of scattering processes. Beyond the inclusion of phenomenological dephasing and relaxation times one could account for, e.g., carrier-carrier or carrier-phonon scattering at the surface. It would be also interesting to abandon the perfect two-dimensional periodicity and to investigate disordered surfaces or to study effects due to the adsorption of impurity atoms and molecules.

"Now this is not the end. It is not even the beginning of the end. But it is, perhaps, the end of the beginning." - Winston Churchill

Zusammenfassung

Gegenstand der vorliegenden Arbeit ist die Licht-Materie-Wechselwirkung in räumlich inhomogenen Halbleiterstrukturen. In den Kapiteln 2, 3 und 4 werden grundlegende Eigenschaften herausgearbeitet, die dadurch entstehen, dass die untersuchten Systeme von dreidimensionaler räumlicher Homogenität abweichen. Darunter ist zu verstehen, dass sowohl das (anregende) Lichtfeld inhomogen verteilt (Kap. 2 und 3) als auch die intrinsischen Materialeigenschaften des Halbleiters räumlich strukturiert sein können (Kap. 2 und 4).

In **Kapitel 2** wird eine Theorie entwickelt, die es ermöglicht, Halbleiterstrukturen zu beschreiben, die sich in der Nähe eines photonischen Kristalls befinden. Dabei hat man unter anderem zwei Effekten Rechnung zu tragen: Zum einen modifiziert die Anwesenheit des photonischen Kristalls die Zustandsdichte des elektromagnetischen Feldes, d.h. durch die periodische Strukturierung des Dielektrikums bildet sich eine Bandstruktur für Licht aus, die unter Umständen Bandlücken oder Defektmoden aufweisen kann. Zum anderen schlagen sich die vorhandenen Grenzflächen zwischen den verschiedenen Dielektrika in den intrinsischen Eigenschaften des Halbleiters nieder, da die Coulomb-Wechselwirkung über Oberflächen-Polarisationen zu räumlich modifizierten Teilchenenergien führt. Zunächst wird eine Theorie zur selbstkonsistenten Lösung der Vektor-Maxwell-Halbleiter-Bloch-Gleichungen vorgestellt, die beide Effekte berücksichtigt.

Bei der Untersuchung der Spektren einer Hybrid-Struktur, bei der periodisch angeordnete Halbleiterquantendrähte unter einem zweidimensionalen photonischen Kristall platziert werden, sind sowohl räumlich veränderliche Exzitonresonanzen als auch Bandkanten-Verschiebungen zu beobachten. Desweiteren stellt man eine räumliche, durch die dielektrische Strukturierung verursachte, Verteilung der Elektron- und Loch-Quasi-Gleichgewichtsdichten fest. Insgesamt führt dies zu beträchtlichen Änderungen in den dichteabhängigen Absorptions-/Gewinnspektren: Im Wesentlichen findet man zwei starke exzitonische Resonanzen, die sich unterschiedlich verhalten. Insbesondere zeigt die

niederenergetische Resonanz des vorliegenden Hybridsystems bereits "Gewinn" für Dichten, bei denen dies in einem homogenen System noch nicht der Fall wäre. Dies liegt daran, dass die Ladungsträger sich in den Bereichen konzentrieren, die mit dieser Resonanz assoziiert werden können. Es wird ferner gezeigt, dass durch eine Erhöhung des Feld-Ladungsträger-Überlaps in genau jenen Bereichen, die Sensitivität auf eine Dichteänderung verstärkt werden kann.

Kapitel 3 beschäftigt sich mit planaren chiralen Nanostrukturen und der Frage, wie die Symmetrieeigenschaften der einzelnen "Komponenten", nämlich die Symmetrie der chiralen Struktur und die des anregenden Lichtfeldes, die Gesamtsymmetrie des Licht-Materie-Systems beeinflussen. Dazu wird eine bestimmte planare chirale Struktur, ein sogenanntes Gammadion, mit linear oder zirkular polarisiertem Licht angeregt und die Eigenschaften des reflektierten Lichts untersucht. Es stellt sich heraus, dass die Intensitätsverteilung im Falle der zirkularen Anregung konkret davon abhängt, ob das einfallende Lichtfeld links- bzw. rechtszirkular polarisiert ist. Geht man von der chiralen Struktur zu deren Enantiomer – also zu deren Spiegelbildstruktur – über und behält den Drehsinn des anregenden Feldes bei, ist eine Brechung der enantiomerischen Symmetrie zu beobachten, d.h. das reflektierte Licht zeigt keine Spiegelsymmetrie im Vergleich zur ersteren Anregung. Dies ist nur der Fall, wenn neben der Struktur auch die Händigkeit des Lichts geändert wird. Die Symmetrieeigenschaften werden sowohl numerisch als auch analytisch untersucht. Bei der analytischen Ableitung wird zudem deutlich, dass der Symmetriebruch durch die Behandlung der vollen Maxwell-Gleichungen sichtbar wird und z.B. nach einer Paraxialnäherung nicht vorhanden wäre.

Lineare und nichtlineare optische Eigenschaften von verschiedenen Silizium-Halbleiteroberflächen werden in **Kapitel 4** behandelt. Die Inhomogenität des Systems kommt hierbei durch das Abweichen von der vollen dreidimensionalen Periodizität im Vergleich zu Volumenmaterial zustande. Dies führt zu Oberflächen-zuständen, die im Allgemeinen andere Eigenschaften als Volumenzustände besitzen.

Für die Si(111)-(2×1) Oberfläche wird eine mikroskopische Theorie vorgestellt, die auf den Halbleiter-Bloch-Gleichungen basiert. Alle relevanten Matrixelemente werden dazu aus einer *ab-initio* Rechnung bestimmt. Es zeigt sich, dass die mit dieser Theorie gewonnenen linearen Absorptionsspektren in guter Übereinstimmung mit experimentellen Daten und anderen theoretischen Rechnungen sind. Das lineare Spektrum ist hauptsächlich durch eine stark absorbierende Exzitonresonanz geprägt. Außerdem hängt die optische Antwort

dieser Oberfläche von der Polarisation des anregenden Pulses ab, was mit der geometrischen Struktur – den Oberflächen-Pandey-Ketten – zusammenhängt. Die Theorie ist gleichfalls auf den nichtlinearen Fall erweiterbar. Bei der Untersuchung des dynamischen optischen Stark Effekts ist eine Blauverschiebung und ein Ausbleichen der Exzitonresonanz festzustellen.

Die Si(001)c(4×2) Oberfläche wird mittels eines phänomenologischen Modells beschrieben. Die Modellierung durch zwei gekoppelte Drei-Niveau-Systeme erweist sich als geeignet, um die wichtigsten Merkmale eines Fünf-Wellen-Misch-Experiments an dieser Oberfläche zu reproduzieren. Im Experiment wird ein verzögerter Anstieg der gebeugten frequenzverdoppelten Lichtintensität beobachtet, der aufgrund von Streuungen der Elektronen im D_{down} Oberflächenband verursacht werden könnte. Diesem Mechanismus wird im Niveau-Modell durch einen Dichtetransfer zwischen den beiden Subsystemen Rechnung getragen, was eine gute Reproduktion des Experiments ermöglicht.

Die hier vorgestellten Ergebnisse zur Licht-Materie-Wechselwirkung in räumlich inhomogenen Halbleiterstrukturen sind nicht nur von fundamentalem Interesse, sondern können sich auch auf die Entwicklung optoelektronischer Bauelemente auswirken. So wird es etwa durch die fortschreitende Miniaturisierung wichtiger, dabei auftretende Oberflächeneffekte zu berücksichtigen. Ebenso wäre es bei der Konzeption von Laserstrukturen denkbar, durch die Verwendung photonischer Kristalle effektivere Geräte zu konstruieren.

Appendix A

System of FDTD-Equations

The Eqs. (A.1)-(A.6) in App. A.1 represent the finite-difference expressions for the Maxwell equations Eqs. (2.7)-(2.8). Any material properties of describable objects are included via the space-dependent electrical permittivity (magnetic permeability) ϵ (μ), hence the set up of equations for $\boldsymbol{E}$ and $\boldsymbol{H}$ are sufficient. Additionally in App. A.2 the electric displacement $\boldsymbol{D}$ and the magnetic induction $\boldsymbol{B}$ are introduced to account for the artificial absorbing boundary medium.

A.1 Three-Dimensional Standard FDTD Equations

$$
\begin{aligned}
E_x|_{i,j+1/2,k+1/2}^{n+1/2} = E_x|_{i,j+1/2,k+1/2}^{n-1/2} + \frac{\Delta t}{\Delta r \; \epsilon|_{i,j+1/2,k+1/2}} \\
\times \left(H_z|_{i,j+1,k+1/2}^{n} - H_z|_{i,j,k+1/2}^{n} - H_y|_{i,j+1/2,k+1}^{n} + H_y|_{i,j+1/2,k}^{n} \right)
\end{aligned}
$$
(A.1)

$$
\begin{aligned}
E_y|_{i-1/2,j+1,k+1/2}^{n+1/2} = E_y|_{i-1/2,j+1,k+1/2}^{n-1/2} + \frac{\Delta t}{\Delta r \; \epsilon|_{i-1/2,j+1,k+1/2}} \\
\times \left(H_x|_{i-1/2,j+1,k+1}^{n} - H_x|_{i-1/2,j+1,k}^{n} - H_z|_{i,j+1,k+1/2}^{n} + H_z|_{i-1,j+1,k+1/2}^{n} \right)
\end{aligned}
$$
(A.2)

$$
\begin{aligned}
E_z|_{i-1/2,j+1/2,k+1}^{n+1/2} = E_z|_{i-1/2,j+1/2,k+1}^{n-1/2} + \frac{\Delta t}{\Delta r \; \epsilon|_{i-1/2,j+1/2,k+1}} \\
\times \left(H_y|_{i,j+1/2,k+1}^{n} - H_y|_{i-1,j+1/2,k+1}^{n} - H_x|_{i-1/2,j+1,k+1}^{n} + H_x|_{i-1/2,j,k+1}^{n} \right)
\end{aligned}
$$
(A.3)

$$
\begin{aligned}
H_x|_{i-1/2,j+1,k+1}^{n+1} = {} & H_x|_{i-1/2,j+1,k+1}^{n} + \frac{\Delta t}{\Delta r \mu} \times \left(E_y|_{i-1/2,j+1,k+3/2}^{n+1/2} \right. \\
& - E_y|_{i-1/2,j+1,k+1/2}^{n+1/2} - E_z|_{i-1/2,j+3/2,k+1}^{n+1/2} + \left. E_z|_{i-1/2,j+1/2,k+1}^{n+1/2} \right)
\end{aligned}
$$

(A.4)

$$
\begin{aligned}
H_y|_{i,j+1/2,k+1}^{n+1} = {} & H_y|_{i,j+1/2,k+1}^{n} + \frac{\Delta t}{\Delta r \mu} \times \left(E_z|_{i+1/2,j+1/2,k+1}^{n+1/2} \right. \\
& - E_z|_{i-1/2,j+1/2,k+1}^{n+1/2} - E_x|_{i,j+1/2,k+3/2}^{n+1/2} + \left. E_x|_{i,j+1/2,k+1/2}^{n+1/2} \right)
\end{aligned}
$$

(A.5)

$$
\begin{aligned}
H_z|_{i,j+1,k+1/2}^{n+1} = {} & H_z|_{i,j+1,k+1/2}^{n} + \frac{\Delta t}{\Delta r \mu} \times \left(E_x|_{i,j+3/2,k+1/2}^{n+1/2} \right. \\
& - E_x|_{i,j+1/2,k+1/2}^{n+1/2} - E_y|_{i+1/2,j+1,k+1/2}^{n+1/2} + \left. E_y|_{i-1/2,j+1,k+1/2}^{n+1/2} \right)
\end{aligned}
$$

(A.6)

A.2   Three-Dimensional FDTD-UPML Equations

For convenience the numbers $s_{x,y,z}$ are identified with

$$
s_{x,y,z} = 1 + \frac{\sigma_{x,y,z}}{i\omega\epsilon}
$$

(A.7)

when matching the tensor $\underline{\underline{s}}$ in Eq. (2.17) with Maxwell's equations in Fourier space. In this way s is related to the electric conductivity σ which gives rise to a lossy artificial material. Its value can be varied depending on the position to achieve an excellent absorbing boundary [36]. The greater σ is the stronger the UPML absorb. However, one has to ensure a smooth increase of the loss parameter in order to keep the spurious reflection small. A typical space-dependent distribution is sketched in Fig. A.1.
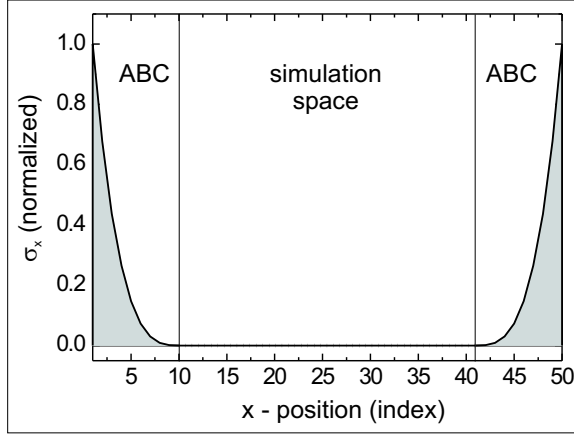
Figure A.1: Space-dependence of the loss parameter σ: Within the simulation space $\sigma \equiv 0$ holds, i.e., the general tensor has the form $\underline{s} \equiv \underline{1}$. At the boundary σ is rising in order to increase the absorbing ability of the UPML.

The finite-difference expressions for the x-component of $\boldsymbol{D}$ and $\boldsymbol{E}$ read

$$
D_x|^{n+1/2}_{i,j+1/2,k+1/2} = \left(\frac{2\,\epsilon|_{i,j+1/2,k+1/2} - \sigma_y \Delta t}{2\,\epsilon|_{i,j+1/2,k+1/2} + \sigma_y \Delta t} \right) D_x|^{n-1/2}_{i,j+1/2,k+1/2}
$$
$$
+ \frac{2\,\epsilon|_{i,j+1/2,k+1/2}\,\Delta t}{\Delta r\,(2\,\epsilon|_{i,j+1/2,k+1/2} + \sigma_y \Delta t)}
$$
$$
\times \left(H_z|^{n}_{i,j+1,k+1/2} - H_z|^{n}_{i,j,k+1/2} - H_y|^{n}_{i,j+1/2,k+1} + H_y|^{n}_{i,j+1/2,k} \right)
$$

$$(A.8)$$

and

$$
E_x|^{n+1/2}_{i,j+1/2,k+1/2} = \left(\frac{2\,\epsilon|_{i,j+1/2,k+1/2} - \sigma_z \Delta t}{2\,\epsilon|_{i,j+1/2,k+1/2} + \sigma_z \Delta t} \right) E_x|^{n-1/2}_{i,j+1/2,k+1/2}
$$
$$
+ \left(\frac{2\,\epsilon|_{i,j+1/2,k+1/2} + \sigma_x \Delta t}{(2\,\epsilon|_{i,j+1/2,k+1/2} + \sigma_z \Delta t)\,\epsilon|_{i,j+1/2,k+1/2}} \right) D_x|^{n+1/2}_{i,j+1/2,k+1/2}
$$
$$
- \left(\frac{2\,\epsilon|_{i,j+1/2,k+1/2} - \sigma_x \Delta t}{(2\,\epsilon|_{i,j+1/2,k+1/2} + \sigma_z \Delta t)\,\epsilon|_{i,j+1/2,k+1/2}} \right) D_x|^{n-1/2}_{i,j+1/2,k+1/2} \; .
$$

$$(A.9)$$

If one neglects the UPML-layers, i.e., if $\sigma = 0$ resulting in $\underline{s} = \underline{1}$ everywhere,

Eqs. (A.8)-(A.9) simplify to

$$D_x|_{i,j+1/2,k+1/2}^{n+1/2} = D_x|_{i,j+1/2,k+1/2}^{n-1/2} + \frac{\Delta t}{\Delta r}$$
$$\times \left(H_z|_{i,j+1,k+1/2}^{n} - H_z|_{i,j,k+1/2}^{n} - H_y|_{i,j+1/2,k+1}^{n} + H_y|_{i,j+1/2,k}^{n} \right)$$

$$(A.10)$$

and

$$E_x|_{i,j+1/2,k+1/2}^{n+1/2} = E_x|_{i,j+1/2,k+1/2}^{n-1/2}$$
$$+ \frac{1}{\epsilon|_{i,j+1/2,k+1/2}} D_x|_{i,j+1/2,k+1/2}^{n+1/2}$$
$$- \frac{1}{\epsilon|_{i,j+1/2,k+1/2}} D_x|_{i,j+1/2,k+1/2}^{n-1/2} \quad ,$$

$$(A.11)$$

respectively. Inserting Eq. (A.10) into Eq. (A.11) yields the standard FDTD-Eq. (A.1). Hence, the UPML equations are a consistent extension of the common FDTD equations in App. A.1.

Appendix B

General Coulomb Potential

In the following, the modified Coulomb potential, Eq. (2.32), is briefly derived. A more comprehensive presentation and remarks to the numerical treatment can be found in Refs. [24, 48].

$$
\begin{aligned}
V^C(\boldsymbol{r}, \boldsymbol{r}') &= \int d^3 r'' \, \delta(\boldsymbol{r} - \boldsymbol{r}'') V^C(\boldsymbol{r}'', \boldsymbol{r}') \\
&= -\frac{1}{4\pi} \int d^3 r'' \left(\Delta_{\mathbf{r}''} \frac{1}{|\boldsymbol{r} - \boldsymbol{r}''|} \right) V^C(\boldsymbol{r}'', \boldsymbol{r}') \\
&= \frac{1}{4\pi} \int d^3 r'' \left(\nabla_{\mathbf{r}''} \frac{1}{|\boldsymbol{r} - \boldsymbol{r}''|} \right) \cdot \nabla_{\mathbf{r}''} V^C(\boldsymbol{r}'', \boldsymbol{r}') \\
&= -\frac{1}{4\pi} \int d^3 r'' \left(\nabla_{\mathbf{r}''} \frac{1}{|\boldsymbol{r} - \boldsymbol{r}''|} \right) \cdot \boldsymbol{E}^L(\boldsymbol{r}'', \boldsymbol{r}') \\
&= -\frac{1}{4\pi} \int d^3 r'' \, \nabla_{\mathbf{r}''} \cdot \left(\frac{1}{|\boldsymbol{r} - \boldsymbol{r}''|} \boldsymbol{E}^L(\boldsymbol{r}'', \boldsymbol{r}') \right) \\
&\quad + \frac{1}{4\pi} \int d^3 r'' \, \frac{1}{|\boldsymbol{r} - \boldsymbol{r}''|} \nabla_{\mathbf{r}''} \cdot \boldsymbol{E}^L(\boldsymbol{r}'', \boldsymbol{r}') \\
&= \ldots
\end{aligned}
$$

$$
\begin{aligned}
\ldots \;=\; & -\frac{1}{4\pi}\sum_i \int_{G_i} d^3 r'' \, \nabla_{\mathbf{r}''} \cdot \left(\frac{1}{|\mathbf{r}-\mathbf{r}''|} \mathbf{E}^L(\mathbf{r}'',\mathbf{r}') \right) \\
& -\frac{1}{4\pi}\int d^3 r'' \, \frac{1}{|\mathbf{r}-\mathbf{r}''|} \nabla_{\mathbf{r}''} \cdot \nabla_{\mathbf{r}''} V^C(\mathbf{r}'',\mathbf{r}') \\
=\; & -\frac{1}{4\pi}\sum_i \int_{\partial G_i} da'' \, \mathbf{n}_i'' \cdot \left(\frac{1}{|\mathbf{r}-\mathbf{r}''|} \mathbf{E}^L(\mathbf{r}'',\mathbf{r}') \right) \\
& +\frac{1}{4\pi}\int d^3 r'' \, \frac{1}{\epsilon_0 \epsilon(\mathbf{r}'')|\mathbf{r}-\mathbf{r}''|}\delta(\mathbf{r}''-\mathbf{r}') \\
=\; & -\frac{1}{4\pi}\sum_{ij} \int_{\partial G_{ij}} da'' \, \frac{1}{|\mathbf{r}-\mathbf{r}''|}\mathbf{n}_i'' \cdot \left(\mathbf{E}_i^L(\mathbf{r}'',\mathbf{r}') - \mathbf{E}_j^L(\mathbf{r}'',\mathbf{r}') \right) \\
& +\frac{1}{4\pi\epsilon_0 \epsilon(\mathbf{r}')|\mathbf{r}-\mathbf{r}'|} \\
=\; & -\frac{1}{4\pi\epsilon_0}\sum_{ij} \left(\frac{1}{\epsilon_i} - \frac{1}{\epsilon_j} \right) \int_{\partial G_{ij}} da'' \, \frac{1}{|\mathbf{r}-\mathbf{r}''|}\mathbf{n}_i'' \cdot \mathbf{D}_i^L(\mathbf{r}'',\mathbf{r}') \\
& +V_0(|\mathbf{r}-\mathbf{r}'|) \\
=\; & V^C(\mathbf{r},\mathbf{r}') \tag{B.1}
\end{aligned}
$$

Appendix C

Optical Bloch Equations up to Fourth Order

The following system of equations constitutes the expansion of the optical Bloch Eqs. (4.28)-(4.33) up to fourth order in the exciting light field for all quantities which are necessary to calculate the time-resolved second-harmonic signal. Each variable carries the indices $[o; (a|b|c)]$ where o is the order of the field and the triple $(a|b|c)$ determines the contributing direction namely $\mathbf{K} = a\mathbf{k}_a + b\mathbf{k}_b + c\mathbf{k}_c$. Integrating the equations simultaneously in time yields $p^{(2\omega)}[4; (-1|1|2)]$ which enters Eq. (4.34).

$$\frac{\partial}{\partial t}p_{lk}^{(\omega)}[1; (1|0|0)] = -\frac{i}{\hbar}(\epsilon_k - \epsilon_l)p_{lk}^{(\omega)}[1; (1|0|0)] - \frac{i}{\hbar}\mathbf{E}(t)[(1|0|0)] \cdot \boldsymbol{\mu}_{lk}^*$$
$$(C.1)$$

$$\frac{\partial}{\partial t}p_{lk}^{(\omega)}[1; (0|1|0)] = -\frac{i}{\hbar}(\epsilon_k - \epsilon_l)p_{lk}^{(\omega)}[1; (0|1|0)] - \frac{i}{\hbar}\mathbf{E}(t)[(0|1|0)] \cdot \boldsymbol{\mu}_{lk}^*$$
$$(C.2)$$

$$\frac{\partial}{\partial t}p_{lk}^{(\omega)}[1; (0|0|1)] = -\frac{i}{\hbar}(\epsilon_k - \epsilon_l)p_{lk}^{(\omega)}[1; (0|0|1)] - \frac{i}{\hbar}\mathbf{E}(t)[(0|0|1)] \cdot \boldsymbol{\mu}_{lk}^*$$
$$(C.3)$$

$$\frac{\partial}{\partial t}n_{ll'}[2; (-1|1|0)] = -\frac{i}{\hbar}(\epsilon_{l'} - \epsilon_l)n_{ll'}[2; (-1|1|0)]$$
$$+\frac{i}{\hbar}\mathbf{E}(t)[(1|0|0)]^* \cdot \sum_k \boldsymbol{\mu}_{l'k}p_{lk}^{(\omega)}[1; (0|1|0)]$$
$$-\frac{i}{\hbar}\mathbf{E}(t)[(0|1|0)] \cdot \sum_k \boldsymbol{\mu}_{lk}^*p_{l'k}^{(\omega)}[1; (1|0|0)]^* \quad (C.4)$$

$$\frac{\partial}{\partial t}n_{ll'}[2;(-1|0|1)] = -\frac{i}{\hbar}(\epsilon_{l'}-\epsilon_l)n_{ll'}[2;(-1|0|1)]$$
$$+\frac{i}{\hbar}\mathbf{E}(t)[(1|0|0)]^* \cdot \sum_k \boldsymbol{\mu}_{l'k}p_{lk}^{(\omega)}[1;(0|0|1)]$$
$$-\frac{i}{\hbar}\mathbf{E}(t)[(0|0|1)] \cdot \sum_k \boldsymbol{\mu}_{lk}^* p_{l'k}^{(\omega)}[1;(1|0|0)]^* \quad \text{(C.5)}$$

$$\frac{\partial}{\partial t}n_{kk'}[2;(-1|1|0)] = -\frac{i}{\hbar}(\epsilon_{k'}-\epsilon_k)n_{kk'}[2;(-1|1|0)]$$
$$-\frac{i}{\hbar}\mathbf{E}(t)[(1|0|0)]^* \cdot \sum_l \boldsymbol{\mu}_{lk}p_{lk'}^{(\omega)}[1;(0|1|0)]$$
$$+\frac{i}{\hbar}\mathbf{E}(t)[(0|1|0)] \cdot \sum_l \boldsymbol{\mu}_{lk'}^* p_{lk}^{(1)*}[1;(1|0|0)]^* \quad \text{(C.6)}$$

$$\frac{\partial}{\partial t}n_{kk'}[2;(-1|0|1)] = -\frac{i}{\hbar}(\epsilon_{k'}-\epsilon_k)n_{kk'}[2;(-1|0|1)]$$
$$-\frac{i}{\hbar}\mathbf{E}(t)[(1|0|0)]^* \cdot \sum_l \boldsymbol{\mu}_{lk}p_{lk'}^{(\omega)}[1;(0|0|1)]$$
$$+\frac{i}{\hbar}\mathbf{E}(t)[(0|0|1)] \cdot \sum_l \boldsymbol{\mu}_{lk'}^* p_{lk}^{(1)*}[1;(1|0|0)]^* \quad \text{(C.7)}$$

$$\frac{\partial}{\partial t}p_{mk}^{(2\omega)}[2;(0|1|1)] = -\frac{i}{\hbar}(\epsilon_k-\epsilon_m)p_{mk}^{(2\omega)}[2;(0|1|1)]$$
$$-\frac{i}{\hbar}\mathbf{E}(t)[(0|1|0)] \cdot \sum_{l'} \boldsymbol{\mu}_{ml'}^* p_{l'k}^{(\omega)}[1;(0|0|1)]$$
$$-\frac{i}{\hbar}\mathbf{E}(t)[(0|0|1)] \cdot \sum_{l'} \boldsymbol{\mu}_{ml'}^* p_{l'k}^{(\omega)}[1;(0|1|0)] \quad \text{(C.8)}$$

$$\frac{\partial}{\partial t}p_{mk}^{(2\omega)}[2;(0|0|2)] = -\frac{i}{\hbar}(\epsilon_k-\epsilon_m)p_{mk}^{(2\omega)}[2;(0|0|2)]$$
$$-\frac{i}{\hbar}\mathbf{E}(t)[(0|0|1)] \cdot \sum_{l'} \boldsymbol{\mu}_{ml'}^* p_{l'k}^{(\omega)}[1;(0|0|1)] \quad \text{(C.9)}$$

$$\frac{\partial}{\partial t}p_{lk}^{(\omega)}[3;(-1|1|1)] = -\frac{i}{\hbar}(\epsilon_k - \epsilon_l)p_{lk}^{(\omega)}[3;(-1|1|1)]$$

$$-\frac{i}{\hbar}\mathbf{E}(t)[(0|1|0)] \cdot \sum_{k'}\boldsymbol{\mu}_{lk'}^* n_{k'k}^{(2)}[2;(-1|0|1)]$$

$$+\frac{i}{\hbar}\mathbf{E}(t)[(0|1|0)] \cdot \sum_{l'}\boldsymbol{\mu}_{l'k}^* n_{ll'}^{(2)}[2;(-1|0|1)]$$

$$-\frac{i}{\hbar}\mathbf{E}(t)[(0|0|1)] \cdot \sum_{k'}\boldsymbol{\mu}_{lk'}^* n_{k'k}^{(2)}[2;(-1|1|0)]$$

$$+\frac{i}{\hbar}\mathbf{E}(t)[(0|0|1)] \cdot \sum_{l'}\boldsymbol{\mu}_{l'k}^* n_{ll'}^{(2)}[2;(-1|1|0)]$$

$$-\frac{i}{\hbar}\mathbf{E}(t)[(0|0|1)]^* \cdot \sum_{m'}\boldsymbol{\mu}_{m'l}\, p_{m'k}^{(2\omega)}[2;(0|1|1)]$$

$$\text{(C.10)}$$

$$\frac{\partial}{\partial t}p_{lk}^{(\omega)}[3;(-1|0|2)] = -\frac{i}{\hbar}(\epsilon_k - \epsilon_l)p_{lk}^{(\omega)}[3;(-1|0|2)]$$

$$-\frac{i}{\hbar}\mathbf{E}(t)[(0|0|1)] \cdot \sum_{k'}\boldsymbol{\mu}_{lk'}^* n_{k'k}^{(2)}[2;(-1|0|1)]$$

$$+\frac{i}{\hbar}\mathbf{E}(t)[(0|0|1)] \cdot \sum_{l'}\boldsymbol{\mu}_{l'k}^* n_{ll'}^{(2)}[2;(-1|0|1)]$$

$$-\frac{i}{\hbar}\mathbf{E}(t)[(1|0|0)]^* \cdot \sum_{m'}\boldsymbol{\mu}_{m'l}\, p_{m'k}^{(2\omega)}[2;(0|0|2)]$$

$$\text{(C.11)}$$

$$\frac{\partial}{\partial t}p_{ml}^{(\omega)}[3;(-1|1|1)] = -\frac{i}{\hbar}(\epsilon_l - \epsilon_m)p_{ml}^{(\omega)}[3;(-1|1|1)]$$

$$-\frac{i}{\hbar}\mathbf{E}(t)[(0|1|0)] \cdot \sum_{l'}\boldsymbol{\mu}_{ml'}^* n_{l'l}^{(2)}[2;(-1|0|1)]$$

$$-\frac{i}{\hbar}\mathbf{E}(t)[(0|0|1)] \cdot \sum_{l'}\boldsymbol{\mu}_{ml'}^* n_{l'l}^{(2)}[2;(-1|1|0)]$$

$$+\frac{i}{\hbar}\mathbf{E}(t)[(1|0|0)]^* \cdot \sum_{k'}\boldsymbol{\mu}_{lk'}\, p_{mk'}^{(2\omega)}[2;(0|1|1)]$$

$$\text{(C.12)}$$

$$\frac{\partial}{\partial t} p_{ml}^{(\omega)}[3; (-1|0|2)] \;=\; -\frac{i}{\hbar}(\epsilon_l - \epsilon_m) p_{ml}^{(\omega)}[3; (-1|0|2)]$$

$$-\frac{i}{\hbar}\mathbf{E}(t)[(0|0|1) \cdot \sum_{l'} \boldsymbol{\mu}_{ml'}^* n_{l'l}^{(2)}[2; (-1|0|1)]$$

$$+\frac{i}{\hbar}\mathbf{E}(t)[(1|0|0)^* \cdot \sum_{k'} \boldsymbol{\mu}_{lk'} p_{mk'}^{(2\omega)}[2; (0|0|2)]$$

<div align="right">(C.13)</div>

$$\frac{\partial}{\partial t} p_{mk}^{(2\omega)}[4; (-1|1|2)] \;=\; -\frac{i}{\hbar}(\epsilon_k - \epsilon_m) p_{mk}^{(2\omega)}[4; (-1|1|2)]$$

$$-\frac{i}{\hbar}\mathbf{E}(t)[(0|0|1)] \cdot \sum_{l'} \boldsymbol{\mu}_{ml'}^* p_{l'k}^{(\omega)}[3; (-1|1|1)]$$

$$-\frac{i}{\hbar}\mathbf{E}(t)[(0|1|0)] \cdot \sum_{l'} \boldsymbol{\mu}_{ml'}^* p_{l'k}^{(\omega)}[3; (-1|0|2)]$$

$$+\frac{i}{\hbar}\mathbf{E}(t)[(0|0|1)] \cdot \sum_{l'} \boldsymbol{\mu}_{l'k}^* p_{ml'}^{(\omega)}[3; (-1|1|1)]$$

$$+\frac{i}{\hbar}\mathbf{E}(t)[(0|1|0)] \cdot \sum_{l'} \boldsymbol{\mu}_{l'k}^* p_{ml'}^{(\omega)}[3; (-1|0|2)]$$

<div align="right">(C.14)</div>

Appendix D

Numerical Parameters

Table D.1: Parameters used for the calculation of the radiative decay shown in Fig. 2.7.

TLS			
transition energy	$\hbar\omega_g$	$=$	1.5 eV
dipole matrix element	μ	$=$	3 eÅ
density of TLS	a_0^{-2}	$=$	5 nm^{-2}
pulse			
envelope (Gaussian)	$E(t)$	$=$	$e^{-\frac{(t-\tau)^2}{(\Delta t)^2}}$
central frequency	$\hbar\omega$	$=$	1.5 eV
temporal width	Δt	$=$	5 fs
delay	τ	$=$	0 ps

Table D.2: Parameters used to study the dependence of the linear absorption spectra on the air cylinder radius shown in Fig. 2.10 and to calculate the density-dependent spectra displayed in Fig. 2.13 and 2.14.

photonic crystal structure

width of unit cell	d	$=$	$9.6a_B$
distance from wire	D	$=$	$0.2a_B$
radius of air cylinder	R	$\in$	$\{0, 2.0a_B, 2.5a_B, 3.5a_B, \infty\}$

quantum wire

electron mass	m_e	$=$	$0.066m_0$ (m_0: free electron mass)
hole mass	m_h	$=$	$0.264m_0$
bandgap	E_{gap}	$=$	1.5 eV
Coulomb regularization	a_0	$=$	$0.16a_B$
homogeneous broadening	γ	$=$	1.3 meV

pulse

envelope (Gaussian)	$E(t)$	$=$	$e^{-\frac{(t-\tau)^2}{(\Delta t)^2}}$
central frequency	$\hbar\omega$	$=$	1.5 eV
temporal width	Δt	$=$	5 fs
delay	τ	$=$	0 ps

Table D.3: Parameters used to investigate chiral structures with the aid of the FDTD-method. The results are shown in Fig. 3.3 and Fig.3.4.

Chiral Structure			
unit cell length	L	$=$	2500 nm
gammadion width[a]	W	$=$	2000 nm
film thickness	T	$=$	175 nm
groove width	G	$=$	450 nm
dielectric constant material	ϵ	$=$	13
pulse			
envelope (Gaussian)	$E(t)$	$=$	$e^{-\frac{(t-\tau)^2}{(\Delta t)^2}}$
vacuum wavelength	λ	$=$	827 nm
temporal width	Δt	$=$	5 fs
delay	τ	$=$	0 ps

[a]In the present case the width of the gammadion is defined as side length of the square with minimum area which covers it completely.

Table D.4: Parameters used for the investigation of chiral structures Fig. 3.5 applying the FEM-method which were performed at the University of Southampton by A.V. Krasavin *et al.*

unit cell length	L	$=$	4100 nm
gammadion width	W	$=$	3400 nm
film thickness	T	$=$	140 nm
groove width	G	$=$	600 nm
dielectric constant for gold	$\epsilon(\boldsymbol{r}, \omega_0)$	$=$	-8.68-1.2i
($\omega_0 = 3 \times 10^{15}$ rad/s)			

Table D.5: Parameters used for calculating the linear spectra shown in Fig. 4.5 and Fig. 4.6.

envelope (Gaussian)	$E(t)$	$=$	$e^{-\frac{(t-\tau)^2}{(\Delta t)^2}}$
central frequency	$\hbar\omega$	$=$	0.69 eV
temporal width	Δt	$=$	1 fs
delay	τ	$=$	0 ps
homogeneous broadening	γ	$=$	50 meV

Each surface wave function is composed of 3367 summands

$$\varphi_{n,\mathbf{k}}(\boldsymbol{r}) = e^{i\mathbf{k}\cdot\mathbf{r}}u_{n,\mathbf{k}}(\boldsymbol{r}) = e^{i\mathbf{k}\cdot\mathbf{r}} \sum_{j=-6}^{6} \sum_{l=-3}^{3} \sum_{j=-18}^{18} c_{n,\mathbf{k},jlm}\, e^{i(j\mathbf{b}_1+l\mathbf{b}_2+m\mathbf{b}_3)\cdot\mathbf{r}},$$

$$(D.1)$$

where $\mathbf{b}_{1,2,3}$ are the primitive reciprocal lattice vectors. The vectors $\mathbf{a}_1 = (6.577, 0, 0)$ Å, $\mathbf{a}_2 = (0, 3.797, 0)$ Å, and $\mathbf{a}_3 = (0, 0, 19.731)$ Å span the direct lattice of the surface supercell. The wave functions were provided by M. Rohlfing.

Table D.6: Parameters used for the investigation of the optical Stark effect analyzed in Fig. 4.8 and Fig. 4.9.

pump

envelope (Gaussian)	$E(t)$	$=$	$e^{-\frac{(t-\tau)^2}{(\Delta t)^2}}$
central frequency Fig. 4.8	$\hbar\omega$	$=$	0.3 eV
central frequency Fig. 4.9	$\hbar\omega$	$=$	0.1...0.3 eV
temporal width	Δt	$=$	250 fs
delay	τ	$=$	0 ps

probe

envelope (Gaussian)	$E(t)$	$=$	$e^{-\frac{(t-\tau)^2}{(\Delta t)^2}}$
central frequency	$\hbar\omega$	$=$	0.69 eV
temporal width	Δt	$=$	1 fs
delay	τ	$=$	0 ps

| homogeneous broadening Fig. 4.8 | γ | $=$ | 50 meV |
| relative amplitudes Fig. 4.8 | $A_{\text{pump}} : A_{\text{probe}}$ | $\propto$ | 0:1, 1:1, 2:1, 3:1 |

| homogeneous broadening Fig. 4.9 | γ | $=$ | 6.6 meV |
| relative amplitudes Fig. 4.9 | $A_{\text{pump}} : A_{\text{probe}}$ | $\propto$ | 1:1, 2:1, 4:1, 8:1 |

Table D.7: Parameters used for the calculation of the three-pulse second-harmonic generation analyzed in Fig. 4.11, Fig. 4.12, and Fig. 4.13.

envelope (sech)	$E(t)$ =	$\mathrm{sech}((t - \tau_{a,b,c})/\bar{t})$
central frequency	$\hbar\omega_{a,b,c}$ =	1.55 eV
temporal width	$\bar{t}_{a,b,c}$ =	7.9 fs
delay	τ_a =	-250...100 fs
	τ_b =	0 fs
	τ_c =	-100...700 fs
Fig. 4.11-Fig. 4.12:		
relaxation time	T_1 =	500 fs
dephasing time	T_2 =	10 fs
transfer time	T_{trans} =	50 fs
detuning of $|l'\rangle$	Δ =	200 meV
	μ_{lk} =	2.0 arb. units
	μ_{ml} =	1.4 arb. units
	μ'_{lk} =	1.0 arb. units
	μ'_{ml} =	1.0 arb. units
	$\nu_{mk} : \nu'_{mk}$ =	1:500
Fig. 4.13:		
relaxation time	T_1 =	500 fs
dephasing time	T_2 =	50 fs
detuning of $|l\rangle$ for the ensemble (N=100)	Δ =	-50...50 meV
detuning of $|l\rangle$ for the single system	Δ =	0
	μ_{lk} =	2.0 arb. units
	μ_{ml} =	1.4 arb. units

Table D.8: Parameters taken from Ref. [103] to calculate the two-pulse second-harmonic generation shown in Fig. 4.16.

envelope (sech)	$E(t)$	$=$	$\mathrm{sech}((t - \tau_{a,b})/\bar{t})$
central frequency (RWA)	$\hbar\omega_a = \hbar\omega_b$	$=$	0 eV
temporal width	$\bar{t}_a = \bar{t}_b$	$=$	7.9 fs
delay	τ_a	$=$	-30...50 fs
	τ_b	$=$	0 fs
relaxation time	T_1	$=$	300 fs
dephasing time	T_2	$=$	3...∞ fs
energy distribution of the lowest state	ΔE	$=$	-300...300 meV
(N=100)			

Appendix E

List of Abbreviations

ABC	-	absorbing boundary conditions
FDTD	-	finite-difference time-domain
FEM	-	finite-element frequency-domain
FM	-	flow map
PCS	-	planar chiral structure
RWA	-	rotating wave approximation
SF	-	scattered field
SH	-	second harmonic
SHG	-	second-harmonic generation
TF	-	total field
TLS	-	two-level system
UPML	-	uniaxial perfectly matched layer
4WM	-	four-wave mixing
5WM	-	five-wave mixing

Bibliography

[1] A.R. Parker. Natural photonic engineers. *Materials Today*, 5:26, 2002.

[2] E. Yablonovitch. Inhibited Spontaneous Emission in Solid-State Physics and Electronics. *Phys. Rev. Lett.*, 58:2059, 1987.

[3] S. John. Strong Localization of Photons in Certain Disordered Dielectric Superlattices. *Phys. Rev. Lett.*, 58:2486, 1987.

[4] J.D. Joannopoulos, R.D. Meade, and J.N. Winn. *Photonic Crystals - Molding the Flow of Light*. Princeton University Press, 1995.

[5] K. Sakoda. *Optical Properties of Photonic Crystals*. Springer Verlag, 2001.

[6] K. Busch, S. Lölkes, R.B. Wehrspohn, and H. Föll. *Photonic Crystals: Advances in Design, Fabrication, and Characterization*. Wiley-VCH, Berlin, 2004.

[7] T. Quang, M. Woldeyohannes, S. John, and G.S. Agarwal. Coherent Control of Spontaneous Emission near a Photonic Band Edge: A Single-Atom Optical Memory Device. *Phys. Rev. Lett.*, 79:5238, 1997.

[8] S. John and J. Wang. Quantum electrodynamics near a photonic band gap: Photon bound states and dressed atoms. *Phys. Rev. Lett.*, 64:2418, 1990.

[9] S. John and T. Quang. Spontaneous emission near the edge of a photonic band gap. *Phys. Rev. A*, 50:1994, 1994.

[10] Y. Akahane, T. Asano, B.S. Song, and S. Noda. High-Q photonic nanocavity in a two-dimensional photonic crystal. *Nature*, 425:944, 2003.

[11] T. Yoshie, J. Vučković, A. Scherer, H. Chen, and D. Deppe. High quality two-dimensional photonic crystal slab cavities. *Appl. Phys. Lett.*, 79:4289, 2001.

[12] H.Y. Ryu, J.K. Hwang, D.S. Song, I.Y. Han, Y.H. Lee, and D.H. Jang. Effect of nonradiative recombination on light emitting properties of two-dimensional photonic crystal slab structures. *Appl. Phys. Lett.*, 78:1174, 2001.

[13] A.A. Erchak, D.J. Ripin, S. Fan, P. Rakich, J.D. Joannopoulos, E.P. Ippen, G.S. Petrich, and L.A. Kolodziejski. Enhanced coupling to vertical radiation using a two-dimensional photonic crystal in a semiconductor light-emitting diode. *Appl. Phys. Lett.*, 78:563, 2001.

[14] M. Boroditsky, T.F. Krauss, R. Coccioli, R. Vrijen, R. Bhat, and E. Yablonovitch. Light extraction from optically pumped light-emitting diode by thin-slab photonic crystals. *Appl. Phys. Lett.*, 75:1036, 1999.

[15] S.H. Kwon, H.Y. Ryu, G.H. Kim, Y.H. Lee, and S.B. Kim. Photonic band-edge lasers in two-dimensional square-lattice photonic crystal slabs. *Appl. Phys. Lett.*, 83:3870, 2003.

[16] H.Y. Ryu, S.H. Kim, H.G. Park, and Y.Hee. Lee. Characteristics of single defect laser modes in a two-dimensional square lattice photonic crystal slab. *J. Appl. Phys.*, 93:831, 2003.

[17] M. Lončar, T. Yoshie, A. Scherer, P. Gogna, and Y. Qiu. Low-threshold photonic crystal laser. *Appl. Phys. Lett.*, 81:2680, 2002.

[18] D.S. Song, S.H. Kim, H.G. Park, C.K. Kim, and Y.H. Lee. Single-fundamental-mode photonic-crystal vertical-cavity surface-emitting lasers. *Appl. Phys. Lett.*, 80:3901, 2002.

[19] S. Noda, M. Yokoyama, M. Imada, A. Chutinan, and M. Mochizuki. Polarization Mode Control of Two-Dimensional Photonic Crystal Laser by Unit Cell Structure Design. *Science*, 293:1123, 2001.

[20] M. Kira, W. Hoyer, T. Stroucken, and S.W. Koch. Exciton Formation in Semiconductors and the Influence of a Photonic Environment. *Phys. Rev. Lett.*, 87:176401, 2001.

[21] T. Stroucken, R. Eichmann, L. Banyai, and S.W. Koch. Excitons in photonic crystals. *J. Opt. Soc. Am. B*, 19:2292, 2002.

[22] R. Eichmann, B. Pasenow, T. Meier, T. Stroucken, P. Thomas, and S.W. Koch. Semiconductor absorption in photonic crystals. *Appl. Phys. Lett.*, 82:355, 2003.

[23] R. Eichmann, B. Pasenow, T. Meier, T. Stroucken, P. Thomas, and S.W. Koch. Semiconductor excitons in photonic crystals. *phys. stat. sol. (b)*, 238:439, 2003.

[24] B. Pasenow. Mikroskopische Theorie exzitonischer Anregungen in photonischen Kristallstrukturen. *Diplomarbeit, Philipps-Universität Marburg*, 2003.

[25] W. Mönch. *Semiconductor Surfaces and Interfaces*. Springer, second edition, 1995.

[26] G. Czycholl. *Theoretische Festkörperphysik*, chapter 9. Vieweg, 2000.

[27] C. Kittel. *Einführung in die Festkörperphysik*, chapter 19. R. Oldenbourg Verlag, twelfth edition, 1999.

[28] J.R. Goldman and J.A. Prybyla. Ultrafast dynamics of laser-excited electron distributions in silicon. *Phys. Rev. Lett.*, 72:1364, 1994.

[29] S. Jeong, H. Zacharias, and J. Bokor. Ultrafast carrier dynamics on the Si(100)2×1 surface. *Phys. Rev. B*, 54:R17300, 1996.

[30] M. Bauer, S. Pawlik, and M. Aeschlimann. Decay dynamics of photoexcited alkali chemisorbates: Real-time investigations in the femtosecond regime. *Phys. Rev. B*, 60:5016, 1999.

[31] W. Berthold, U. Höfer, P. Feulner, E.V. Chulkov, V.M. Silkin, and P.M. Echenique. Momentum-Resolved Lifetimes of Image-Potential States on Cu(100). *Phys. Rev. Lett.*, 88:056805, 2002.

[32] N. Bloembergen, R.K. Chang, S.S. Jha, and C.H. Lee. Optical Second-Harmonic Generation in Reflection from Media with Inversion Symmetry. *Phys. Rev.*, 174:813, 1968.

[33] Y.R. Shen. Optical Second Harmonic Generation at Interfaces. *Ann. Rev. Phys. Chem.*, 40:327, 1989.

[34] U. Höfer. Time-resolved coherent spectroscopy of surface states. *Appl. Phys. B*, 68:383, 1999.

[35] M. Reichelt, B. Pasenow, T. Meier, T. Stroucken, and S.W. Koch. Spatially inhomogeneous optical gain in semiconductor photonic-crystal structures. *Phys. Rev. B*, 71:035346, 2005.

[36] A. Taflove and S.C. Hagness. *Computational Electrodynamics: The Finite-Difference Time-Domain Method*. Artech House, second edition, 2000.

[37] A. Taflove. *Advances in Computational Electrodynamics*. Artech House, 1998.

[38] K.S. Yee. Numerical solution of initial boundary value problems involving Maxwell's equations in isotropic media. *IEEE Trans. Antennas and Propagation*, 14:302, 1966.

[39] B. Pasenow, private communication.

[40] Z.S. Sacks, D.M. Kingsland, R. Lee, and J.F. Lee. A perfectly matched anisotropic absorber for use as an absorbing boundary condition. *IEEE Trans. Antennas and Propagation*, 43:1460, 1995.

[41] K. Zimmermann. Zur Theorie der elektromagnetischen Kopplung in periodischen Quantenpunkt-Strukturen. *Diplomarbeit, Technische Universität Berlin*, 2003.

[42] R.W. Ziolkowski. The Incorporation of Microscopic Material Models into the FDTD Approach for Ultrafast Optical Pulse Simulations. *IEEE Trans. Antennas and Propagation*, 45:375, 1997.

[43] A.S. Nagra and R.A. York. FDTD Analysis of Wave Propagation in Nonlinear Absorbing and Gain Media. *IEEE Trans. Antennas and Propagation*, 46:334, 1998.

[44] H. Haug and S.W. Koch. *Quantum theory of the optical and electronic properties of semiconductors*. World Scientific, Singapore, fourth edition, 2004.

[45] W.H. Press, S.A. Teukolsky, W.T. Vetterling, and B.P. Flannery. *Numerical Recipes in C++*. Cambridge University Press, second edition, 2002.

[46] L. Allen and J.H. Eberly. *Optical Resonance and Two-Level Atoms*. Dover Publications, New York, 1987.

[47] B. Pasenow, M. Reichelt, T. Stroucken, T. Meier, S.W. Koch, A.R. Zakharian, and J.V. Molone. Enhanced light-matter interaction in semiconductor heterostructures embedded in one-dimensional photonic crystals. *J. Opt. Soc. Am. B, in press*.

[48] R. Eichmann. Lineare optische Eigenschaften dielektrisch strukturierter Halbleiter. *Dissertation, Philipps-Universität Marburg*, 2002.

[49] J.D. Jackson. *Classical Electrodynamics*. John Wiley & Sons, third edition, 1998.

[50] W. Nolting. *Grundkurs: Theoretische Physik, 3. Elektrodynamik*. Zimmermann-Neufang, Ulmen, 4 edition, 1996.

[51] A. Messiah. *Quantenmechanik*. Walter de Gruyter, Berlin, 1981.

[52] A. Knorr. Spatial Effects in the Ultrafast Optics and Kinetics of Semiconductors. *Habilitationsschrift, Philipps-Universität Marburg*, 1997.

[53] L. Bányai, I. Galbraith, C. Ell, and H. Haug. Excitons and biexcitons in semiconductor quantum wires. *Phys. Rev. B*, 36:6099, 1987.

[54] B. Pasenow, M. Reichelt, T. Stroucken, T. Meier, and S.W. Koch. Excitonic wave packet dynamics in semiconductor photonic-crystal structures. *Phys. Rev. B, in press*.

[55] T. Yoshie, A. Scherer, J. Hendrickson, G. Khitrova, H.M. Gibbs, G. Rupper, C. Ell, O.B. Shchekin, and D.G. Deppe. Vacuum Rabi splitting with a single quantum dot in a photonic crystal nanocavity. *Nature*, 432:200, 2004.

[56] A. Papakostas, A. Potts, D.M. Bagnall, S.L. Prosvirnin, H.J. Coles, and N.I. Zheludev. Optical Manifestations of Planar Chirality. *Phys. Rev. Lett.*, 90:107404, 2003.

[57] A.S. Schwanecke, A. Krasavin, D.M. Bagnall, A. Potts, A.V. Zayats, and N.I. Zheludev. Broken Time Reversal of Light Interaction with Planar Chiral Nanostructures. *Phys. Rev. Lett.*, 91:247404, 2003.

[58] T. Vallius, K. Jefimovs, J. Turunen, P. Vahimaa, and Y. Svirko. Optical activity in subwavelength-period arrays of chiral metallic particles. *Appl. Phys. Lett.*, 83:234, 2003.

[59] S.L. Prosvirnin and N.I. Zheludev. Polarization effects in the diffraction of light by a planar chiral structure. *Phys. Rev. E*, 71:037603, 2005.

[60] D. Bedeaux, M.A. Osipov, and J. Vlieger. Reflection of light at structured chiral interfaces. *J. Opt. Soc. Am. A*, 21:2431, 2004.

[61] E.L. Eliel and S.H. Wilen. *Stereochemistry of Organic Compounds*. Wiley-Interscience, 1994.

[62] M. Reichelt, T. Stroucken, S.W. Koch, A.V. Krasavin, A.S. Schwanecke, N.I. Zheludev, and E.M. Wright. Broken enantiomeric symmetry for electromagnetic waves interacting with planar chiral nanostructures. *Submitted to Phys. Rev. A*.

[63] T. Warncke (née Stroucken), private communication.

[64] M. Lax, W.H. Louisell, and W.B. McKnight. From Maxwell to paraxial wave optics. *Phys. Rev. A*, 11:1365, 1975.

[65] A.V. Krasavin, A.S. Schwanecke, M. Reichelt, T. Stroucken, S.W. Koch, E.M. Wright, and N.I. Zheludev. Polarization Conversion and "Focusing" of Light Propagating through a Small Chiral Hole in a Metallic Screen. *Appl. Phys. Lett.*, 86:201105, 2005.

[66] M. Wegener, D.S. Chemla, S. Schmitt-Rink, and W. Schäfer. Line shape of time-resolved four-wave mixing. *Phys. Rev. A*, 42:5675, 1990.

[67] M. Lindberg, R. Binder, and S.W. Koch. Theory of the semiconductor photon echo. *Phys. Rev. A*, 45:1865, 1992.

[68] K. Leo, M. Wegener, J. Shah, D.S. Chemla, E.O. Göbel, T.C. Damen, S. Schmitt-Rink, and W. Schäfer. Effects of coherent polarization interactions on time-resolved degenerate four-wave mixing. *Phys. Rev. Lett.*, 65:1340, 1990.

[69] S.T. Cundiff, H. Wang, and D.G. Steel. Polarization-dependent picosecond excitonic nonlinearities and the complexities of disorder. *Phys. Rev. B*, 46:7248, 1992.

[70] S. Schmitt-Rink and D.S. Chemla. Collective Excitations and the Dynamical Stark Effect in a Coherently Driven Exciton System. *Phys. Rev. Lett.*, 57:2752, 1986.

[71] B. Fluegel, N. Peyghambarian, G. Olbright, M. Lindberg, S.W. Koch, M. Joffre, D. Hulin, A. Migus, and A. Antonetti. Femtosecond Studies of Coherent Transients in Semiconductors. *Phys. Rev. Lett.*, 59:2588, 1987.

[72] C. Sieh, T. Meier, A. Knorr, F. Jahnke, P. Thomas, and S.W. Koch. Influence of carrier correlations on the excitonic optical response including disorder and microcavity effects. *European Physical Journal B*, 11:407, 1999.

[73] H. Haken. *Quantenfeldtheorie des Festkörpers*. Teubner, 2 edition, 1993.

[74] M.S. Hybertsen and S.G. Louie. First-Principles Theory of Quasiparticles: Calculation of Band Gaps in Semiconductors and Insulators. *Phys. Rev. Lett.*, 55:1418, 1985.

[75] M. Rohlfing and S.G. Louie. Excitons and Optical Spectrum of the Si(111)-(2×1) Surface. *Phys. Rev. Lett.*, 83:856, 1999.

[76] J.E. Northrup, M.S. Hybertsen, and S.G. Louie. Many-body calculation of the surface-state energies for Si(111)2×1. *Phys. Rev. Lett.*, 66:500, 1991.

[77] X. Zhu and S.G. Louie. Quasiparticle surface band structure and photo-electric threshold of Ge(111)-2×1. *Phys. Rev. B*, 43:12146, 1991.

[78] M. Rohlfing and S.G. Louie. Optical Reflectivity of the Si(111)-(2×1) Surface - The Role of the Electron-Hole Interaction. *phys. stat. sol. (a)*, 175:17, 1999.

[79] M. Rohlfing. Excited Electronic States and Optical Spectra of Solids, Surfaces, and Molecules. *Habilitationsschrift, Wilhelms-Universität Münster*, 2000.

[80] M. Rohlfing, M. Palummo, G. Onida, and R. del Sole. Structural and Optical Properties of the Ge(111)-(2×1) Surface. *Phys. Rev. Lett.*, 85:5440, 2000.

[81] M. Rohlfing. Quasiparticle spectrum and optical excitations of semiconductor surfaces. *Appl. Phys. A*, 72:413, 2001.

[82] K.C. Pandey. Reconstruction of Semiconductor Surfaces: Buckling, Ionicity, and π-Bonded Chains. *Phys. Rev. Lett.*, 49:223, 1982.

[83] Thanks to Oleg Rubel for generating the three-dimensional plot with the Cerius^2 molecular simulation package.

[84] M. Lindberg and S.W. Koch. Effective Bloch equations for semiconductors. *Phys. Rev. B*, 38:3342, 1988.

[85] S. Selci, F. Ciccacci, G. Chiarotti, P. Chiaradia, and A. Cricenti. Surface differential reflectivity spectroscopy of semiconductor surfaces. *J. Vac. Sci. Technol. A*, 5:327, 1987.

[86] M. Reichelt, T. Meier, M. Rohlfing, and S.W. Koch. Microscopic theory for the nonlinear optical response of the Si(111)-(2×1) surface exciton. *phys. stat. sol. (b)*, 238:525, 2003.

[87] P. Chiaradia, A. Cricenti, S. Selci, and G. Chiarotti. Differential Reflectivity of the Si(111)-(2×1) Surface with Polarized Light: A Test for Surface Structure. *Phys. Rev. Lett.*, 52:1145, 1984.

[88] C. Goletti, G. Busetti, F. Arciprete, P. Chiaradia, and G. Chiarotti. Infrared surface absorption in Si(111)-(2×1) observed with reflectance anisotropy spectroscopy. *Phys. Rev. B*, 66:153307, 2002.

[89] M. Reichelt, T. Meier, S.W. Koch, and M. Rohlfing. Theory for the nonlinear optical response of semiconductor surfaces: Application to the optical Stark effect and spectral oscillations of the Si(111)-(2×1) surface exciton. *Phys. Rev. B*, 68:045330, 2003.

[90] C. Sieh, T. Meier, F. Jahnke, A. Knorr, S.W. Koch, P. Brick, M. Hübner, C. Ell, J. Prineas, G. Khitrova, and H.M. Gibbs. Coulomb Memory Signatures in the Excitonic Optical Stark Effect. *Phys. Rev. Lett.*, 82:3112, 1999.

[91] P. Brick, C. Ell, S. Chatterjee, G. Khitrova, H.M. Gibbs, T. Meier, C. Sieh, and S.W. Koch. Influence of light holes on the heavy-hole excitonic optical Stark effect. *Phys. Rev. B*, 64:075323, 2001.

[92] R. Binder, S.W. Koch, M. Lindberg, W. Schäfer, and F. Jahnke. Transient many-body effects in the semiconductor optical Stark effect: A numerical study. *Phys. Rev. B*, 43:6520, 1991.

[93] R. Oszwaldowski, M. Reichelt, T. Meier, S.W. Koch, and M. Rohlfing. Nonlinear optical response of the Si(111)-(2 × 1) surface exciton: Influence of biexciton many-body correlations. *Phys. Rev. B, in press*.

[94] V.M. Axt and A. Stahl. A dynamics-controlled truncation scheme for the hierarchy of density matrices in semiconductor optics. *Z. Phys. B*, 93:195, 1994.

[95] V.M. Axt and A. Stahl. The role of the biexciton in a dynamic density matrix theory of the semiconductor band edge. *Z. Phys. B*, 93:205, 1994.

[96] S. Weiser. Exzitonische Korrelationseffekte in der nichtlinearen Optik ungeordneter Halbleiter. *Diplomarbeit, Philipps-Universität Marburg*, 1999.

[97] C. Voelkmann. Incoherent and coherent dynamics of electronic surface states on silicon surfaces. *Dissertation, MPI für Quantenoptik, TU München, Philipps-Universität Marburg,*, 2001.

[98] C. Voelkmann, M. Reichelt, T. Meier, S.W. Koch, and U. Höfer. Five-Wave-Mixing Spectroscopy of Ultrafast Electron Dynamics at a Si(001) Surface. *Phys. Rev. Lett.*, 92:127405, 2004.

[99] T. Meier, M. Reichelt, S.W. Koch, and U. Höfer. Femtosecond Time-Resolved Five-Wave Mixing at Silicon Surfaces. *J. Phys.: Condens. Matter 17*, 17:221, 2005.

[100] J. Pollmann, P. Krüger, M. Rohlfing, M. Sabisch, and D. Vogel. Ab initio calculations of structural and electronic properties of prototype surfaces of group IV, III-V and II-VI semiconductors. *Appl. Surf. Sci.*, 104/105:1, 1996.

[101] M. Weinelt, M. Kutschera, T. Fauster, and M. Rohlfing. Dynamics of Exciton Formation at the Si(100)c(4×2) Surface. *Phys. Rev. Lett.*, 92:126801, 2004.

[102] C. Voelkmann, M. Maurer, W. Berthold, and U. Höfer. Second-Harmonic Diffraction from a Transient Population Grating of Silicon Dangling Bonds. *phys. stat. sol. (a)*, 175:169, 1999.

[103] M. Reichelt. Mikroskopische und phänomenologische Beschreibung ausgewählter kohärenter optischer Phänomene in Halbleitern. *Diplomarbeit, Philipps-Universität Marburg*, 2001.

[104] M. Koch, D. Weber, J. Feldmann, E.O. Göbel, T. Meier, A. Schulze, P. Thomas, and S. Schmitt-Rink. Subpicosecond photon-echo spectroscopy on GaAs/AlAs short-period superlattices. *Phys. Rev. B*, 47:1532, 1993.

[105] N. Peyghambarian, S.W. Koch, and A. Mysyrowicz. *Introduction to Semiconductor Optics*. Prentice-Hall, 1993.

[106] N.A. Kurnit, I.D. Abella, and S.R. Hartmann. Observation of a Photon Echo. *Phys. Rev. Lett.*, 13:567, 1964.

[107] T. Meier, A. Schulze, P. Thomas, H. Vaupel, and K. Maschke. Signatures of Fano resonances in four-wave-mixing experiments. *Phys. Rev. B*, 51:13977, 1995.

Publications in the Context of this Thesis

Publications concerning chapter 2

- *Spatially-inhomogeneous optical gain in semiconductor photonic-crystal structures*, M. Reichelt, B. Pasenow, T. Meier, T. Stroucken, and S.W. Koch, Phys. Rev. B **71**, 035346 (2005).

- *Excitonic wave packet dynamics in semiconductor photonic-crystal structures*, B. Pasenow, M. Reichelt, T. Stroucken, T. Meier, and S.W. Koch, Phys. Rev. B, in press.

- *Enhanced light-matter interaction in semiconductor heterostructures embedded in one-dimensional photonic crystals*, B. Pasenow, M. Reichelt, T. Stroucken, T. Meier, S.W. Koch, A.R. Zakharian, and J.V. Molone, J. Opt. Soc. Am. B, in press.

Publications concerning chapter 3

- *Broken enantiomeric symmetry for electromagnetic waves interacting with planar chiral nanostructures* M. Reichelt, T. Stroucken, S.W. Koch, A.V. Krasavin, A.S. Schwanecke, N.I. Zheludev, and E.M. Wright, submitted to Phys. Rev. A

- *Polarization Conversion and "Focusing" of Light Propagating through a Small Chiral Hole in a Metallic Screen*, A.V. Krasavin, A.S. Schwanecke, M. Reichelt, T. Stroucken, S.W. Koch, E.M. Wright, and N.I. Zheludev, Appl. Phys. Lett. **86**, 201105 (2005).

Publications concerning chapter 4

- *Theory for the nonlinear optical response of semiconductor surfaces: Application to the optical Stark effect and spectral oscillations of the Si(111)-(2x1) surface exciton*, M. Reichelt, T. Meier, S.W. Koch, and M. Rohlfing, Phys. Rev. B **68**, 045330 (2003).

- *Microscopic theory for the nonlinear optical response of semiconductor surfaces: Application to the optical Stark effect of the Si(111)-(2x1) surface exciton*, M. Reichelt, T. Meier, S.W. Koch, and M. Rohlfing, phys. stat. sol. (b) **238**, 525-528 (2003).

- *Five-Wave-Mixing Spectroscopy of Ultrafast Electron Dynamics at a Si(001) surface*, C. Voelkmann, M. Reichelt, T. Meier, S.W. Koch, and U. Höfer, Phys. Rev. Lett. **92**, 127405 (2004).

- *Femtosecond Time-Resolved Five-Wave Mixing at Silicon Surfaces*, T. Meier, M. Reichelt, S.W. Koch, and U. Höfer, invited review, J. Phys.: Condens. Matter **17**, S221-S244 (2005).

- *Nonlinear optical response of the Si(111)-(2x1) surface exciton: Influence of biexciton many-body correlations*, R. Oszwaldowski, M. Reichelt, T. Meier, S.W. Koch, and M. Rohlfing, Phys. Rev. B, in press.

Miscellaneous

- *Microscopic Theory for the Nonlinear Optical Response of the Si(111)-(2×1) surface exciton* M. Reichelt, T. Meier, S.W. Koch, and M. Rohlfing, talk, NOEKS 2003

- *Excitonic semiconductor absorption in photonic crystals*, M. Reichelt, R. Eichmann, B. Pasenow, T. Meier, T. Stroucken, P. Thomas, and S.W. Koch poster presentation Q49.2, DPG-Frühjahrstagung, Hannover (2003).

- *Optical Properties of Semiconductor Photonic-Crystal Structures* B. Pasenow, M. Reichelt, T. Stroucken, T. Meier, and S.W. Koch poster presentation, 323. Heraeus-Seminar "From Photonic Crystals to Metamaterials - Artificial Materials in Optics", Bad Honnef (2004)

Danksagung

In erster Linie möchte ich mich bei den Mitstreitern im "Photonischen Kristall Projekt" Bernhard Pasenow und Tineke Warncke bedanken. Beide haben mir wesentliche Impulse beim Durchdenken physikalischer Probleme gegeben. Meinem Doktorvater Stephan Koch danke ich für die langjährige Unterstützung von der Diplomzeit an. Regelmäßige Gespräche und ein hervorragendes Umfeld haben das Arbeiten stets angenehm gestaltet. Torsten Meier hat mir in allen Bereichen wertvolle Anregungen gegeben, wofür ich ihm herzlich danke. Peter Thomas danke ich für interessante Diskussionen und die Erinnerung, dass auch im Computerzeitalter die Welt nicht hinter dem Monitor aufhört. Bei Jens Förstner und Andreas Zeiser von der TU-Berlin bedanke ich mich für die Zeit, die sie für die Anmerkungen zum FDTD-Code aufgebracht haben. Für die Mithilfe im Bereich der Halbleiter-Oberflächen gebührt Carsten Voelkmann, der die 5WM-Experimente durchführte, und Michael Rohlfing von der IU-Bremen, der die Quasiteilchen-Wellenfunktionen zur Verfügung stellte, mein Dank. Erwähnen möchte ich auch die großzügige Unterstützung durch das Graduiertenkolleg "Optoelektronik mesoskopischer Halbleiter" und durch das European Graduate College "Electron-Electron Interactions in Solids".

Die Atmosphäre in der Arbeitsgruppe war stets freundlich: Bei Sven muss ich mich dafür bedanken, dass er mir bei potentiell 312 ℓ Kaffee fast immer den schönen Ausblick[1] gelassen hat. Christoph war zu jeder Tageszeit[2] für ein Schwätzchen zu haben. Ralf hat mir netterweise den Umgang mit sehr vielen Computern gelernt.[3] Angela bringt mich (verbal) jeden Tag drei Euro näher zum Millionär.[4] Claudia hat mein Englisches Vokabular etwas aufgebessert: "Thanks a bomb!" Thomas hat mich durch die Superlativen des viel tieferen Rechnens[5] und des viel mehr Essens angespornt, wesentliche Teile meines Lebens zu perfektionieren. Péter, thank you for alluding to Xanthippe's[6] course, it is much fun.

Meinem Freund Lars danke ich, dass er die Geduld hatte, mir immer zuzuhören, sich sowohl auf die universelle Philosophie ("Per se existieren keine Dreiecke.") als auch die individuelle ("Schönes Dreieck!") einließ, und mir dabei den Großteil[7] der Brötchen überließ.

---

[1]"Isis", a goddess and a snatcher.

[2]Saturday, Saturday, Saturday Night's Alright. . .

[3]mailx -s "Danke!" ralf.eichmann@nun-geschaeftsmann.de < to-instructor.txt

[4]Mein Haus, mein Auto, mein Origami-Papierschiff.

[5]Gemeint ist so was wie 24.Txd4!!! (Kasparov-Topalov, Wijk aan Zee, 1999).

[6]You know, the wife of Socrates.

[7]Im Schnitt gilt: $G = \min\{rolls \in \mathbb{R}^+ \,|\, \sin(rolls) + 1 = 0\}$.

Wissenschaftlicher Werdegang

seit Juni 2001

Wissenschaftlicher Mitarbeiter in der Arbeitsgruppe Theoretische Halbleiter-physik, Philipps-Universität Marburg

April 1996 - Mai 2001

Studium der Physik an der Philipps-Universität Marburg

April 1998   Diplom-Vorprüfung
Mai 2001   Abschluss des Studiums mit Diplomprüfung